REGRESSION RATE STUDY OF POROUS AXIAL-INJECTION, END-BURNING HYBRID FUEL GRAINS

by

MATTHEW A. HITT

A DISSERTATION

Submitted in partial fulfillment of the requirements
for the degree of Doctor of Philosophy
in
The Department of Mechanical and Aerospace Engineering
to
The School of Graduate Studies
of
The University of Alabama in Huntsville

HUNTSVILLE, ALABAMA

2016

In presenting this dissertation in partial fulfillment of the requirements for a doctoral degree from The University of Alabama in Huntsville, I agree that the Library of this University shall make it freely available for inspection. I further agree that permission for extensive copying for scholarly purposes may be granted by my advisor or, in his/her absence, by the Chair of the Department or the Dean of the School of Graduate Studies. It is also understood that due recognition shall be given to me and to The University of Alabama in Huntsville in any scholarly use which may be made of any material in this thesis.

Matthew A. Hitt

Matthew A. Hitt

3/16/2016

(date)

DISSERTATION APPROVAL FORM

Submitted by Matthew A. Hitt in partial fulfillment of the requirements for the degree of Doctor of Philosophy in Mechanical Engineering and accepted on behalf of the Faculty of the School of Graduate Studies by the dissertation committee.

We, the undersigned members of the Graduate Faculty of The University of Alabama in Huntsville, certify that we have advised and/or supervised the candidate of the work described in this dissertation. We further certify that we have reviewed the dissertation manuscript and approve it in partial fulfillment of the requirements for the degree of Doctor of Philosophy in Mechanical Engineering.

Robert A Frederick Jr 3/16/16
Dr. Robert A. Frederick (date) Committee Chair

3/16/16
Dr. Keith Hollingsworth (date)

3/16/2016
Dr. David M. Lineberry (date)

3/16/2016
Dr. D. Brian Landrum (date)

3/10/16
Dr. Kunning Gabriel Xu (date)

3/16/16
Dr. Keith Hollingsworth (date) Department Chair

03/17/16
Dr. Shankar Mahalingam (date) College Dean

3/23/16
Dr. David Berkowitz (date) Graduate Dean

ABSTRACT
School of Graduate Studies
The University of Alabama in Huntsville

Degree Doctor of Philosophy College/Dept. Engineering/Mechanical and Aerospace Engineering

Name of Candidate Matthew A. Hitt

Title Regression Rate Study of Porous Axial-Injection, End-Burning Hybrid Fuel Grains

This experimental and theoretical work examines the effects of gaseous oxidizer flow rates and pressure on the regression rates of porous fuels for hybrid rocket applications. Testing was conducted using polyethylene as the porous fuel and both gaseous oxygen and nitrous oxide as the oxidizer. Nominal test articles were tested using 200, 100, 50, and 15 micron fuel pore sizes. Pressures tested ranged from atmospheric to 1160 kPa for the gaseous oxygen tests and from 207 kPa to 1054 kPa for the nitrous oxide tests, and oxidizer injection velocities ranged from 35 m/s to 80 m/s for the gaseous oxygen tests and from 7.5 m/s to 16.8 m/s for the nitrous oxide tests. Regression rates were determined using pretest and posttest length measurements of the solid fuel. Experimental results demonstrated that the regression rate of the porous axial-injection, end-burning hybrid was a function of the chamber pressure, as opposed to the oxidizer mass flux typical in conventional hybrids. Regression rates ranged from approximately 0.75 mm/s at atmospheric pressure to 8.89 mm/s at 1160 kPa for the gaseous oxygen tests and 0.21 mm/s at 207 kPa to 1.44 mm/s at 1054 kPa for the nitrous oxide tests.

The analytical model was developed based on a standard ablative model modified to include oxidizer flow through the grain. The heat transfer from the flame was

primarily modeled using an empirically determined flame coefficient that included all heat transfer mechanisms in one term. An exploratory flame model based on the Granular Diffusion Flame model used for solid rocket motors was also adapted for comparison with the empirical flame coefficient. This model was then evaluated quantitatively using the experimental results of the gaseous oxygen tests as well as qualitatively using the experimental results of the nitrous oxide tests. The model showed agreement with the experimental results indicating it has potential for giving insight into the flame structure in this motor configuration. Results from the model suggested that both kinetic and diffusion processes could be relevant to the combustion depending on the chamber pressure.

Abstract Approval: Committee Chair Robert A Frederick Jr.

Department Chair

Graduate Dean

ACKNOWLEDGMENTS

Completing this dissertation has been a journey that would not have been possible without the aid and support of many people. First, I would like to thank my committee. My advisor and committee chair, Dr. Robert Frederick hired me as an undergrad researcher at the PRC back in 2008 probably without realizing that I would stay at the PRC for the next eight years. His advice and encouragement during my pursuit of the Ph.D. in addition to his funding of my research have been invaluable. I could not have asked for a better advisor. I would like to thank Dr. David Lineberry for all of his help with helping me formulate my test ideas and for enduring all the operating procedure revisions. His office was always open for me to come think through what I needed to do to actually find the results I needed. Dr. Keith Hollingsworth was of great aid in developing the modified ablative model and in encouraging me to strive to better understand the driving physics of the experiment. Dr. Brian Landrum helped keep me grounded in the reality that I couldn't solve everything at once and needed to focus on solving my one small contribution very well. Dr. Gabe Xu was instrumental in the decision making process with the committee as to the route that I would take which is much appreciated. I have learned much from my committee, and it is much appreciated.

Next, I would like to acknowledge funding support provided through the Science, Mathematics & Research for Transformation (SMART) Scholarship and thank all the PRC staff and students who provided help and support along the way. Amy Parlett was of great assistance in my being able to conduct all of my experiments. Her ability and willingness to help is greatly appreciated. I would also like to thank the other students that helped with my experiments, Ezekiel Parrow, Carolyn Boos, and Claire Staschus.

Chris Hill's assistance by machining the test plates is greatly appreciated. In addition, Joe Buckley's aid through performing the XCT scans of the test articles is greatly appreciated. I would also like to thank my fellow grad students, Dan Jones, Amit Patel, Brian Sweeney, Andrew Hiatt, Brian Roy, Jake Cranford, and Matt Denny for helping to make the PRC such a great place to be. I would also like to acknowledge my former officemate, Dr. John Bennewitz. He provided a lot of encouragement during my time as a grad student. Anthony Edmondson was of great assistance behind the scenes procuring necessary parts and making sure I kept all my paperwork in order. His effort is greatly appreciated. Also, Claudia Meyering in the MAE office arranged for me to work as a Graduate Teaching Assistant for a couple of semesters to cover a gap in my funding. Her aid in keeping me funded through my degree is much appreciated. I would also like to thank George Story for his interest in my research and for providing relevant articles for my literature review.

No acknowledgement of those that aided in my research would be complete without mentioning the PRC Facilities Engineer, Tony Hall. Tony provided aid in formulating the test setup and aided in setting up for tests, leak checking, and conducting experiments as needed. That aid is much appreciated. However, I feel Tony's greatest contribution to this process was by encouraging a sophomore back in 2008 who didn't know anything about propulsion other than that he wanted to do it to apply for a job at the PRC. I will always be thankful for that encouragement.

In addition, I would like to thank my parents for their support during this time. Their encouragement has been invaluable, and my mother's proofreading of all my papers is much appreciated. The support of my brothers and their families is appreciated

as well. Lastly, I would like to thank Olivia Johnson for her encouragement to keep going and aid in interpreting comments.

The opportunity to pursue a Ph.D. has been a gift from God. Looking back through the years, I can see the hand of Divine Providence that has guided me to this point.

TABLE OF CONTENTS

Page

LIST OF FIGURES

LIST OF TABLES

Table Page

LIST OF SYMBOLS

A	Pre-exponential factor
B	Systematic expanded uncertainty
C_d	Orifice discharge coefficient
C_{fl}	Flame coefficient
c_{liq}	Specific heat of liquid fuel
c_p	Specific heat
c_{sol}	Specific heat of solid fuel
D	Flame height
d_o	Oxidizer particle diameter
d_t	Orifice throat diameter
E_a	Activation energy
GDF	Granular Diffusion Flame
GOX	Gaseous oxygen
g_o	Gravitational constant
$\Delta h_{f,dec}$	Fuel latent heat of decomposition
$\Delta h_{f,melt}$	Fuel latent heat of fusion
Δh_{tot}	Total fuel decomposition enthalpy requirement
h	Enthalpy
h_{fs}	Enthalpy required for sublimation
I_{sp}	Specific impulse
k	Thermal conductivity
k_1	Diffusion parameter
k_2	Pocket density
L_D	GDF diffusion flame height
L_k	GDF kinetic flame height
L_{tot}	GDF combined flame height
MW	Molecular weight
$\dot{m}$	Mass flow rate
$\dot{m}''$	Mass flux
O/F	Mixture ratio

Pe	Peclet number
Pr	Prandtl number
PRC	Propulsion Research Center
p_{ch}	Chamber pressure
q_s	Heat transfer from flame to fuel
Q_s	Fuel Gasification Heat Requirement
Re	Reynolds number
R_g	Gas constant
S_L	Flame speed
$\dot{r}$	Regression rate
T	Temperature
T_g	Mean temperature of flame and surface
UAH	University of Alabama in Huntsville
U	Expanded uncertainty
V	Velocity
ΔV	Change in velocity
α	Absorptivity
β	Orifice beta ratio
γ	Ratio of specific heats
ε	Emissivity
μ	Dynamic viscosity
ρ	Density
σ	Stefan-Boltzmann constant
ζ	Propellant mass fraction

Subscripts

a	Liquid fuel at melting temperature
dec	Decomposition
e	Liquid fuel at decomposition temperature
f	Fuel
fl	Flame

g	Gas
liq	Liquid
m	Solid fuel at melting temperature
melt	Melt
o	Initial condition
ox	Oxidizer
rad	Radiation
s	Fuel vapor at decomposition temperature, fuel surface
sol	Solid
u	Unburned
w	Wall

To my fiancée, Olivia Johnson
I love you

"The works of the LORD are great, sought out
of all them that have pleasure therein."
- Psalm 111:2

CHAPTER 1

INTRODUCTION

Hybrid rocket motors are a demonstrated alternative to liquid rocket engines and solid rocket motors for use in rocket propulsion systems. In general, hybrid motors use a combination of one propellant in solid phase (typically the fuel) and the other propellant in liquid or gaseous phase (typically the oxidizer). The oxidizer flow rate is controlled by the oxidizer injection system while the fuel flow rate is driven by the vaporization rate of the solid fuel. One means of measuring the vaporization rate of the fuel is by determining the rate at which the solid grain regresses as it burns. This rate is known as the regression rate and is an essential part of predicting hybrid fuel performance. For system applications, the regression rates of typical hybrid fuels are an order of magnitude too low to effect efficient volumetric loading of the fuels. As such, understanding basic combustion mechanisms to augment the fuel regression is critical to increasing the practicality of hybrid rocket motors as propulsion systems.

1.1 Literature Review

To gain a better understanding of the physics driving hybrid fuel regression and ways to augment it, a literature review of hybrid motor design and fuel regression was conducted. The literature review focused on hybrid rocket fundamentals, hybrid fuel regression, and various means that have been tested to enhance hybrid fuel regression.

Reviewing the literature provided an understanding regarding the physics behind hybrid fuel regression, the techniques that have been used to enhance the regression rate, and the opportunities in the field for further investigation.

1.1.1 Hybrid Rocket Motor Fundamentals

Many different forms of rocket propulsion exist. In general, these methods function by increasing the velocity of the rocket through a momentum exchange according to Newton's Third Law of Motion. This exchange is accomplished by accelerating the propellant through a nozzle. Energy can be provided to the propellant in several different ways. In chemical propulsion, the energy of the propellant is converted into high-enthalpy and high-velocity gasses using combustion. In nuclear propulsion, the working fluid's energy is increased by transferring heat from a reactor to the working fluid using a heat exchanger. Several different methods are used in electric propulsion. In electrothermal propulsion, the working fluid's energy is increased by electrical heating such as by electrical arcs or resistive heating. In ion propulsion, the working fluid is ionized and then accelerated through the use of electrostatic fields. For electromagnetic propulsion, an ionized gas is accelerated through the use of electric and magnetic fields. While the different propulsion methods have applications that use their respective advantages, only chemical propulsion has been used to propel a rocket into flight. [1]

The three primary methods of chemical propulsion are liquid propulsion, solid propulsion, and hybrid propulsion. Liquid propulsion is used in either monopropellant or bipropellant form. In monopropellant liquid propulsion, a single propellant is stored in a tank and then either pressure fed through a nozzle or fed over a catalyst to promote decomposition. In bipropellant liquid propulsion, both the oxidizer and the fuel are in

liquid form and are stored in separate tanks. The propellant is fed to the engine using either a pressure fed or a pump fed system. In solid propulsion, the oxidizer and the fuel are in solid form and are mixed together into a heterogeneous grain which is stored in the thrust chamber. For hybrid propulsion, one of the propellants is in solid form and the other propellant is in either liquid or gaseous form. The standard method is to use a solid fuel and a liquid oxidizer. The liquid propellant is stored in a tank and fed into the engine while the solid propellant is formed into a grain and stored in the thrust chamber. [1]

Hybrid rocket motors have several advantages as compared to liquid rocket engines or solid rocket motors. These advantages include greater safety as compared to solid rocket motors due to the separation of the fuel and oxidizer storage areas, greater reliability as compared to liquid rocket engines due to the elimination of one propellant feed-system, as well as the capability to throttle thrust during operation and stop-restart capability [1]. However, hybrid rockets do have several disadvantages. These disadvantages include mixture ratio shift during operation, low regression rates leading to lower propellant mass fractions, susceptibility to chugging instability, and complicated port combustion leading to difficulties in modeling the port physics [1].

A diagram of a notional hybrid rocket booster is shown in Figure 1.1 [1]. As can be seen in the figure, the hybrid propulsion system contains a hydroxyl-terminated polybutadiene (HTPB) fuel grain stored in the combustion chamber in the aft end of the rocket as well as a liquid oxygen (LOX) tank with a pressurization system to supply the oxidizer. An injector plate is located between the oxidizer tank and the fuel grain to introduce the oxidizer into the fuel ports for combustion. The combustion products and

any remaining uncombusted fuel and oxidizer enter the mixing chamber for final combustion and then are accelerated out the nozzle to provide thrust. [1]

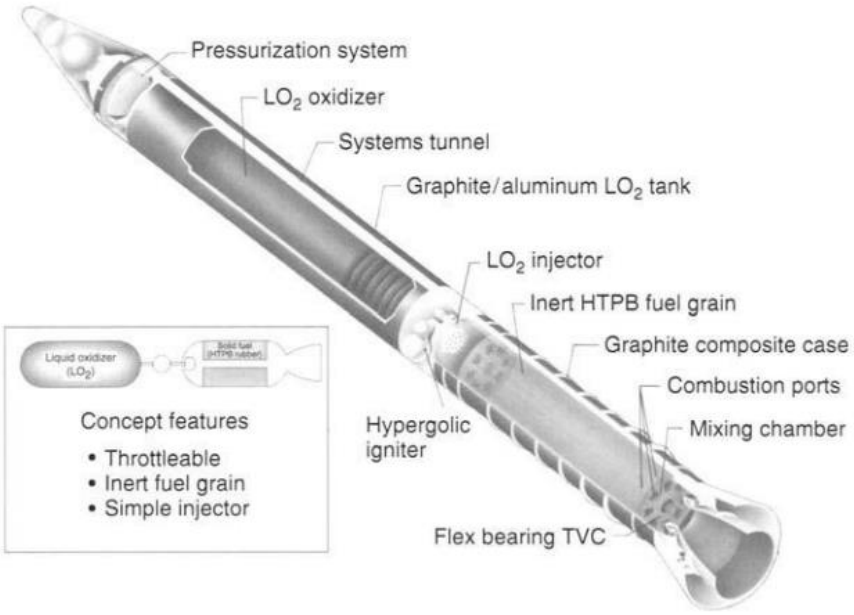

Figure 1.1. Sample Hybrid Rocket Layout [1]

Hybrid rockets have been investigated for use in several areas but have not seen widespread acceptance. The American Rocket Company (AMROC) performed several static firings of hybrid rocket motors in the 1980's and 90's but were unsuccessful in developing an operational hybrid rocket motor [1]. However, successful launches of hybrid rockets have been performed. Lockheed Martin launched a sounding rocket using a hybrid rocket motor in 2002 [1], and Nammo Raufoss, in conjunction with Lockheed Martin Michoud Operations and Andøya Rocket Range, launched a hybrid test rocket in 2007 [2-3]. The most significant use of a hybrid rocket motor was on Scaled Composite's SpaceShipOne which won the Ansari X-prize in 2004. The motor used on SpaceShipOne was designed by SpaceDev who had, in 1998, bought the rights to

AMROC's designs [1]. In addition to these uses, there has been interest in investigating the use of hybrid rocket motors on nanosatellites [4-5]. Due to the small scale of nanosatellites, most nanosatellites serve as secondary payloads on launch vehicles. As such, their orbit insertion is driven by the primary payload's orbit requirements. Adding a propulsion unit to the nanosatellites allows for orbit adjustment, but the propulsion unit must be inert on the vehicle to prevent any risk of damaging the primary payload before orbit insertion [4]. Another significant challenge is the development of a practical multiple re-ignition system. Hybrid rocket motors meet both challenges of maintaining inertness on the vehicle due to propellant separation and of providing a configuration that allows for re-ignition. Additionally, larger propulsion units could allow for extra-planetary missions by constellations of nanosatellites. This would allow for increased numbers of exploratory missions since constellations of nanosatellites would be a potentially less expensive option as compared to traditional satellites [5].

Hydroxyl-terminated polybutadiene (HTPB) is a common baseline fuel used in hybrid rocket motor designs and research. HTPB is inert, nontoxic, and low cost. In addition, hybrid motors with an HTPB and LOX propellant combination yields a performance equivalent to that of an engine using LOX and kerosene [1]. Other fuels with similar performance to HTPB include acrylonitrile-butadiene-styrene (ABS) [6] and polyethylene [7]. One particular area of interest in research is the use of additively manufactured ABS as a potential hybrid fuel [6, 8-12]. The interest in additive manufacturing is the potential that it provides for designing complex ports that would be impractical to create with traditional manufacturing methods and for reducing the cost associated with manufacturing complex grains [8].

As can be expected since hybrids combine aspects of liquid engines and solid motors, the performance of hybrid rocket motors falls between that of liquid rocket engines and solid rocket motors. A chart showing the relative theoretical specific impulse of propellant combinations for solids, hybrids, and liquids is shown in Figure 1.2 [13]. Specific impulse is a metric similar to a "gas mileage" that tells how much total impulse can be extracted from a given weight of propellant. As can be seen in the figure, hybrid rocket motors as a group have higher specific impulse values than solid rocket motors but lower values than liquid rocket engines as a group. However, due to the higher density of materials in solid phase than in liquid phase, the density specific impulse of hybrid rocket motors is lower than that of solid rocket motors but higher than that of liquid rocket engines. Density specific impulse can be a critical design metric for volume limited designs as the density specific impulse indicates the total impulse that can be extracted from a given volume.

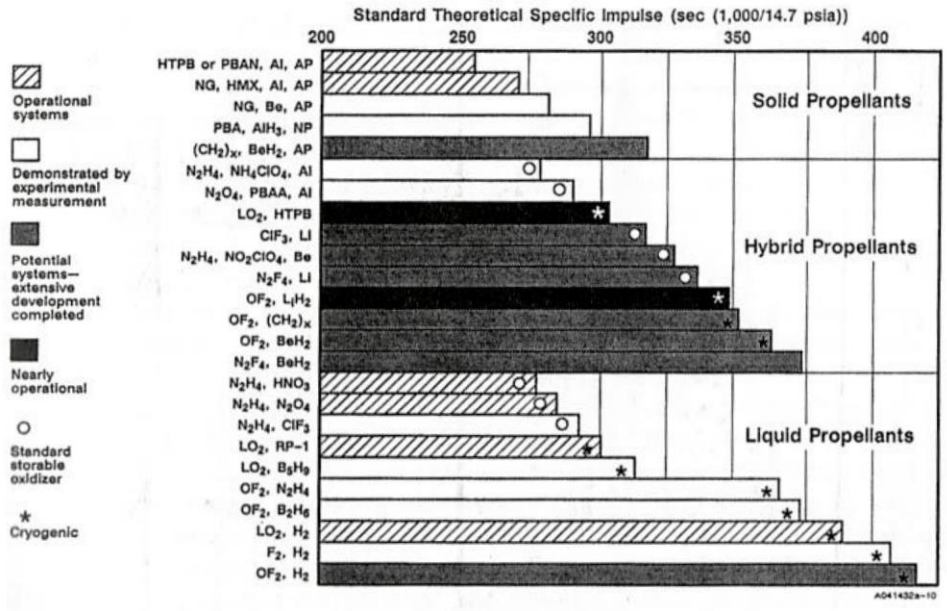

Figure 1.2. Hybrid Rocket Performance Comparison [13]

The importance of specific impulse is given in the rocket equation shown by

$$\Delta V = -I_{sp} g_o \ln(1 - \zeta) \tag{1.1}$$

where ΔV is the change in velocity of a spacecraft, I_{sp} is the specific impulse, g_o is the gravitational constant and ζ is the propellant mass fraction. The propellant mass fraction is given by the equation

$$\zeta = \frac{m_p}{m_o} \tag{1.2}$$

where m_p is the total mass of the propellant consumed (counting both fuel and oxidizer) and m_o is the initial mass of the spacecraft (including the propellant mass). As can be seen in Eq. 1.1, the velocity change can be increased by either increasing the specific impulse or by increasing the propellant mass fraction of the spacecraft. This illustrates the importance of the regression rate to hybrid rocket performance since increasing the regression rate increases the propellant mass fraction of the vehicle. This relationship shows that the velocity change of a spacecraft using a hybrid rocket motor can be increased by enhancing the regression rate of the solid fuel. It will be shown later that the regression rate also affects the specific impulse of the motor; however, the effect changes based upon the mixture ratio of the propellants.

Since the regression rate of the hybrid fuel grain is critical to motor performance, an understanding of the design of the fuel grains is important. A diagram showing a notional classical hybrid fuel grain is given in Figure 1.3 [1]. As can be seen in the figure, the oxidizer is introduced to the fuel grain through an injector at the head end of the motor. While not the primary means of driving fuel regression, the injector design does have an impact on the regression rate [14]. The fuel grain itself often utilizes a multi-port configuration as shown in Section B-B in the figure. Multi-port designs are

used to increase the surface area of the fuel exposed to the oxidizer to account for the low regression rate of classical hybrid motors since a larger burn surface area is required to counterbalance a low regression rate to maintain sufficient fuel mass flow. This design choice has drawbacks since multiple ports reduces the volumetric loading of the grain and thin webbings between the ports increases the risk of structural failure of the webbing leading to chunks of unburned to be expelled from the nozzle at the end of burning. However, thick webbings to prevent web breakoff results in larger propellant residuals after motor operation. Both low volumetric loading and large propellant residuals lead to lower propellant mass fractions reducing the amount of velocity change delivered by the motor [1]. In addition, low volumetric loading can lead to increases in grain length or diameter which in turn can lead to increases in vehicle drag (this effect is more significant with increases in diameter). These potential drawbacks indicate the importance of improving regression rates as increases in fuel regression could eliminate the need for multi-port grain designs. Of additional note is the presence of a mixing chamber at the aft end of the grain before the nozzle. The mixing chamber promotes complete mixing and combustion of the propellants before exiting the nozzle. Due to the diffusion mixing of the oxidizer and fuel in the boundary layer, port lengths on the order of up to 40 to 100 port diameters could be required for complete mixing and combustion. The addition of an aft mixing chamber promotes mixing and allows for shortening the length of the fuel grain [15].

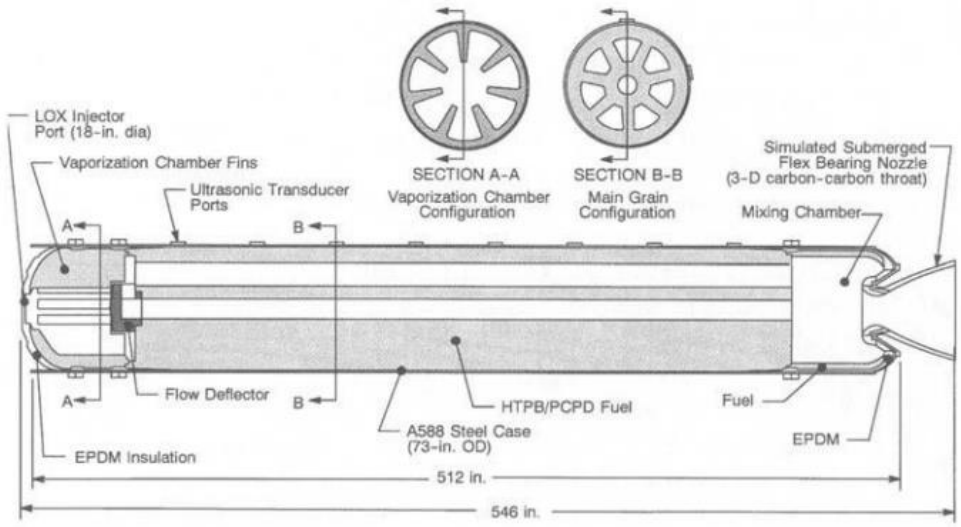

Figure 1.3. Hybrid Fuel Grain [1]

The performance of hybrid rocket motors can be understood by a series of equations. As stated before, the fuel mass flow rate is a critical piece of hybrid rocket performance. The equation for the fuel mass flow rate in a circular combustion port is given by

$$\dot{m}_f = \pi d_p L_c \dot{r} \rho_f \tag{1.3}$$

where $\dot{m}_f$ is the fuel mass flow rate, d_p is the diameter of the port, L_c is the length of the port, $\dot{r}$ is the regression rate, and ρ_f is the density of the fuel. The combined terms, π, d_p, and L_c represent the burn surface area of the grain (this representation would be modified for noncircular ports). Using the mass flow rate of the oxidizer and the fuel, the mixture ratio can be calculated using the equation

$$O/_F = \frac{\dot{m}_{ox}}{\dot{m}_f} \tag{1.4}$$

where *O/F* is the mixture ratio and $\dot{m}_{ox}$ is the oxidizer mass flow rate. Example mixture ratio values for stoichiometric conditions include 3.4 for oxygen/ethylene combustion

and approximately 3 for oxygen/HTPB combustion [1]. The mixture ratio is an important parameter for motor performance as it determines the chamber properties such as chamber temperature, molecular weight of the products, ratio of specific heats, and characteristic velocity. Another way of describing the mixture ratio is the equivalence ratio which can be defined as

$$\phi = \frac{(O/F)_{stoic}}{(O/F)} \tag{1.5}$$

where ϕ is the equivalence ratio and $(O/F)_{stoic}$ is the mixture ratio at stoichiometric conditions. As with the mixture ratio, the equivalence ratio is a useful parameter for evaluating combustion properties.

Using the propellant flow rates, combustion properties, and nozzle design, motor performance values such as thrust and impulse can be calculated. First, the chamber pressure can be calculated using the equation

$$p_1 = \frac{c^*(\dot{m}_{ox}+\dot{m}_f)}{A_t}\eta_{c^*} \tag{1.6}$$

where p_1 is the chamber pressure, c^* is the characteristic velocity, A_t is the nozzle throat area, and η_{c^*} is the characteristic velocity efficiency. The chamber pressure can be used to design the motor grain and case so that it can withstand the stresses. In addition, it can also be used to calculate the motor thrust using the equation

$$F = C_F p_1 A_t \tag{1.7}$$

where F is the thrust and C_F is the thrust coefficient which is determined by the ratio of the chamber pressure to the ambient pressure and the nozzle expansion ratio. Using the thrust, the total impulse of the motor can be calculated by integrating the motor thrust over time using the equation

$$I_t = \int F\, dt \tag{1.8}$$

where I_t is the total impulse of the motor. By dividing the total impulse of the motor by the weight of the propellants consumed, the specific impulse of the motor can be calculated using the equation

$$I_{sp} = \frac{I_t}{(m_{ox}+m_f)g_c} \tag{1.9}$$

where m_{ox} is the mass of the oxidizer consumed and m_f is the mass of the fuel consumed. The specific impulse can be used in Eq. 1.1 to calculate the change in velocity of the rocket. As can be seen in Eqs. 1.3 through 1.9, the regression rate influences the specific impulse through its contribution to the fuel mass flow rate. However, the influence does not follow a simple correlation as the mixture ratio has a significant impact on the chamber properties and thus the specific impulse. In general, motors tend to have superior performance at mixture ratios near the stoichiometric condition. As such, regression rate adjustments that drive the mixture ratio to the stoichiometric value tend to increase the specific impulse, and adjustments that drive the mixture ratio away from the stoichiometric value tend to decrease the specific impulse. Due to low regression rates, hybrid rocket motors tend to operate in oxidizer rich conditions; as such, increases in regression rate can lead to increases in specific impulse as well as propellant mass fraction. In addition, although the mixture ratio of a hybrid can produce optimal specific impulse at one point in the grain evolution, the nonlinear response of the fuel regression as the ports change causes shifts that lower the specific impulse [1].

1.1.2 Hybrid Fuel Regression

Hybrid fuel regression is driven by the transfer of heat from the flame to the fuel grain. A picture showing the proposed physics of the process is shown in Figure 1.4 [16].

As can be seen in the figure, combustion in a hybrid rocket motor is a complex process. In the figure, the flow is from left to right. An oxidizer core flows above the turbulent boundary layer and diffuses through the boundary layer to reach the flame zone where it reacts with the fuel. On the left side of the figure are several radial profiles that describe the distribution of fuel, oxidizer, and products at various locations in the flow. The curve labeled "Y_O" indicates the mass fraction of the oxidizer, "Y_F" indicates the mass fraction of the fuel, and "Y_P" indicates the mass fraction of the combustion products. As can be seen, the oxidizer mass fraction is largest in the core flow and decreases toward the grain surface; the fuel mass fraction is highest at the grain surface and decreases toward the core flow; and the products mass fraction peaks at the flame zone and decreases toward both the core flow and the grain surface [16].

Also of interest in the figure is the illustration of the major parts of the heat transfer from the flame to the grain and the energy balance at the fuel surface. The primary means of heat transfer from the flame as shown in the figure are convection and radiation. In addition, the figure shows the possibility of additional radiation from soot particles in the flow. Also shown is a blocking effect where the vaporization of the fuel from the surface provides a flow normal to the grain surface that inhibits convective heat transfer from the flame to the surface [16]. Finally, the dashed lines around the grain towards the right of the figure show the energy flux balance at the grain surface.

While the energy balance can be quite complex, some parts of the balance include the convective (Term 1) and radiative (Term 3) heat transfer to the grain, enthalpy requirements for pyrolysis (Terms 6 and 8), conduction from the surface into the grain (Term 2), radiation absorption by the grain below the surface (Term 4), and the enthalpy

of the fuel entering the control volume as the grain regresses (Terms 5 and 7) [16]. In short, the regression of the fuel is driven by the ability to control the processes that control the heat transfer from the combustion to the grain surface to pyrolize the fuel. Pyrolization is hindered by ineffective heat transfer from the flame to the grain (due to the blocking effect caused by the vaporizing fuel, low heat transfer coefficients, etc.) and by heat transfer from the surface to internal portions of the grain. Primary means of enhancing grain regression are by increasing the heat transfer to the grain or by decreasing the heat required to pyrolize the fuel.

The characteristics of hybrid fuel regression respond to the oxidizer mass flux in the port, radiation, and pressure differently depending on the operating conditions. Several different regimes exist for hybrid fuel regression. A plot illustrating these regimes is shown in Figure 1.5 [16]. As can be seen in the figure, the regimes are primarily dependent on the oxidizer mass flux which is equal to the oxidizer mass flow rate divided by the port cross-sectional area. In the middle regime, the regression rate is primarily driven by the turbulent heat transfer with no explicit pressure dependence. This regime is the one in which most hybrids operate [16]. In this regime, it is assumed that the reaction is diffusion limited in that the limiting factor for the flame is the diffusion of fuel and oxidizer to the flame. The reaction rates are assumed to be instantaneous compared to the diffusion process [15]. Marxman [15] postulated that since the velocity of the oxidizer in the core flow is roughly tangential to the flame (see Figure 1.4) convection would not be a significant mechanism in transporting the oxidizer to the flame.

Figure 1.4. Hybrid Motor Combustion [16]

While the flux-dominant dependency is generally true, if the oxidizer flux is increased above a critical point, the chemical kinetics become more influential in describing the regression rate as the reaction rates start becoming more significant when compared to the diffusion rate. In this regime, the regression rate obtains an explicit pressure dependence due to the kinetic effects [16]. Similarly, if the oxidizer flux drops below a certain threshold, an explicit pressure dependence is also obtained as the radiation heat flux starts to become more significant as compared to the convective heat transfer. The significance of the radiation heat flux can be driven by the reduced convective heat transfer associated with lower oxidizer mass fluxes. However, radiation heat flux can become significant without the requirement of low oxidizer mass fluxes if the fuel grain contains metallic particles or if the combustion products of the oxidizer and fuel are sooty [16].

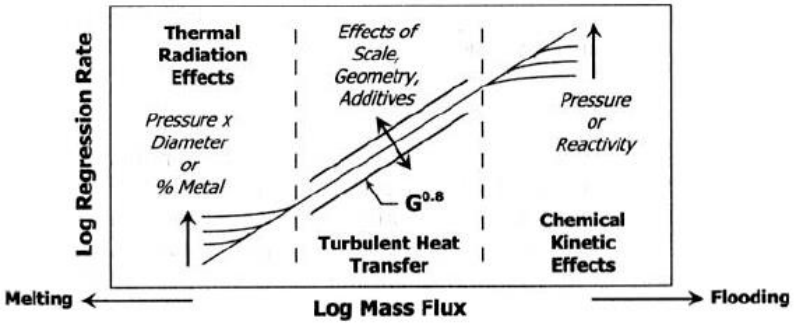

Figure 1.5. Hybrid Motor Regression Rate Regimes [16]

Several correlations have been developed to predict the regression rate based on various physical parameters. Marxman and Gilbert [15] and Marxman et al. [17] derived equations for diffusion-limited, turbulent combustion in a hybrid rocket which led to the equation given as

$$\rho_f \dot{r} = 0.036 G B^{0.23} Re_x^{-0.2} \propto B^{0.23} G^{0.8} x^{-0.2} \tag{1.10}$$

where G is the total mass flux through the port (includes both fuel and oxidizer flow rates), B is the blowing number, Re_x is the Reynolds number based on axial length, and x is the axial distance in the port. Going over the terms in Eq. 1.10, the port mass flux is given by the equation

$$G = \frac{\dot{m}}{A_p} \tag{1.11}$$

where $\dot{m}$ is the mass flow rate through the port and A_p is the area of the port. The blowing number accounts for the effect of the injection of fuel vapor from the grain wall. The equation for calculating the blowing number is given by

$$B = \frac{\rho v|_w}{\rho_e u_e (c_f/2)} = \frac{u_e}{u_{fl}} \left[\frac{h_{fl} - h_w}{\Delta H_{v,eff}} \right] \tag{1.12}$$

where $\rho v|_w$ is the momentum density of the vapor injected from the wall, ρ_e is the density of the freestream port flow, u_e is the velocity of the freestream port flow, c_f is the friction coefficient of the wall surface, u_{fl} is the flame velocity, h_{fl} is the enthalpy of the flame, h_w is the enthalpy of the fuel at the grain surface, and $\Delta H_{v,eff}$ is the enthalpy required to vaporize the fuel. As can be seen in Eq. 1.12, the blowing number can be represented as either a momentum ratio parameter based on the wall and freestream densities and velocities or as a thermodynamic parameter based on the flame and wall enthalpies. The Reynolds number is given by the equation

$$Re_x = \frac{Gx}{\mu} \tag{1.13}$$

where μ is the viscosity of the port flow. The Reynolds number is the ratio of inertial forces to viscous forces and indicates whether the flow is laminar or turbulent. Due to combustion and the surface mass injection from the fuel grain, it is expected that the port

flow transitions to turbulent flow shortly after injection [15]. Experiments were conducted by Marxman et al. to validate the derived equations. Both the derivations and the initial experiments were based on the assumption of a flat plate burner as opposed to a cylindrical grain. Since real hybrid motors typically exist as cylindrical grains as opposed to flat burners, additional experiments were conducted to evaluate the applicability of Eq. 1.10 to cylindrical grains. These experiments demonstrated that cylindrical grains generally followed the predicted trend within experimental error [17]. Altman and Humble [18] revisited the correlation given in Eq. 1.10 and determined that an exponent of "0.32" instead of "0.23" for the blowing number provided a more accurate correlation [16].

Marxman [19] later revisited the correlation in presented in Eq. 1.10 to account for effects due to variable fluid properties in the port flow. This correlation is given by the equation

$$\rho_f \dot{r} = 0.036 G \left(\frac{\bar{\rho}}{\rho_e}\right)^{0.6} B^{0.23} Re_x^{-0.2} \tag{1.14}$$

where $\bar{\rho}$ is the average density in the boundary layer. This result was successfully compared with experimental data, but its usefulness was observed to be limited by the difficulty of precisely determining the density ratio [19]. This equation was further refined by Marxman [20] to account for the presence of heterogeneous reactions in the port. Heterogeneous reactions occur when oxidizer passes through the flame uncombusted and reacts with the solid fuel on the grain surface. The correlation accounting for heterogeneous reactions is given by the equation

$$\rho_f \dot{r} = 0.036 G \left(\frac{\bar{\rho}}{\rho_e}\right)^{0.6} (B')^{0.23} Re_x^{-0.2} \left[exp\left(\frac{-Q_h}{Q_c}\right) + \frac{Q_h}{Q_c}\right] \tag{1.15}$$

where B' is the blowing number times the Prandtl number, Q_h is the heat flux from the heterogeneous reactions, and Q_c is the convective heat flux from the flame to the grain. The Prandtl number is given by

$$Pr = \frac{c_p \mu}{k} \tag{1.16}$$

where c_p is the specific heat at constant pressure and k is the thermal conductivity. For a gas, the Prandtl number is on the order of 0.7.

The correlation given in Eq. 1.15 was originally derived and validated based upon accounting for radiation heat flux instead of heterogeneous reaction heat flux. The impact of heterogeneous reaction was then formulated by Marxman by extension of the same physical principles [20]. Of particular note in the equation is that the effects of the separate heat fluxes are not additive. The presence of an additional heat source (whether from radiation or from heterogeneous reactions) decreases the convective heat flux to the grain. This lessening of the convective heat flux is caused by a "blocking" effect where the vaporized fuel's leaving the surface decreases the ability of the heat to convect from the flame back to the grain surface due to the fuel vapor's velocity's being normal to the grain surface. The normality of the fuel velocity lessens the convective heat transfer as it can force warmer gasses away from the surface. [16].

In addition to the derived correlations, several empirical curve fits have been performed to describe hybrid regression rate for a variety of regimes. These empirical correlations are typically performed to simplify the expression and aid in calculations. However, since the equations are empirically derived, they are only applicable to the specific propellant combination and motor geometry. Muzzy [21] provided a correlation for a kinetically influenced motor using the equation

$$\dot{r} = C_5 P^{0.5} G^{0.3} x^{-0.2} \tag{1.18}$$

where C_5 is an empirically derived constant, P is the chamber pressure, and x is the axial location along the grain. This expression was validated using data from a 80% PB/20% PMMA fuel and IRFNA oxidizer propellant combination [21]. Of particular interest in Muzzy's equation describing the kinetically influenced regime is the presence of an explicit pressure dependence. As noted previously, pressure dependence is not typically a property of diffusion limited regimes but it is one of kinetically influenced regimes [16].

A final empirical correlation that is popular to describe the regression rate of a hybrid motor is presented in Sutton [1] using the equation

$$\dot{r} = aG^n \tag{1.19}$$

where a and n are experimentally determined constants based on experiments conducted using particular propellant combinations and configurations with limited applicability outside of those conditions. These coefficients are typically calculated based on the mass flux's being the oxidizer mass flux as opposed to the total mass flux of the oxidizer and fuel. This form provides advantages in that it is tractable to use (only one variable is present) and allows for simple calculations and comparisons between propellant combinations and motor configurations.

As can be seen in the various correlations presented, the regression rate of a conventional hybrid rocket motor is a function of the mass flux (typically simplified to the oxidizer mass flux). This functionality can result in mixture ratio shifts. Mixture ratio shifts can result from two primary mechanisms. The first mechanism is the change in oxidizer mass flux during operation. For a constant oxidizer mass flow rate, the

oxidizer mass flux will decrease during motor operation due to the increasing port cross-sectional area caused by the grain regression. While the motor length can be chosen to achieve optimal conditions at one point during operation, the changing flux will drive the motor off the optimal condition. The second mechanism is the non-linear coupling of the fuel mass flow rate with the oxidizer mass flow rate. For motors where the exponent in Eq. 1.19 is not equal to 0.5, the fuel mass flow rate is non-linearly coupled to the oxidizer mass flow rate. As such, any throttling of the oxidizer mass flow rate will result in a shift of the mixture ratio. As stated previously, mixture ratio shifts from either mechanism lower the specific impulse of the motor. [1]

1.1.3 Swirling Flow Hybrids

One means of increasing the regression rate of hybrid fuel grains is by using swirling flow [22]. The creation of swirl in the combustion chamber can be created by several designs including swirl injection [22], vortex injection [23], swirl end burners [16], radial end burners [16], multi-slot swirl injection [7, 24-25], and swirling ports (often created using additive manufacturing) [8, 26-27]. A sketch showing the basic thought of swirling flow is given in Figure 1.6 [22]. As can be seen in the figure, the port flow has both an axial component ("*U*") and a rotational component ("*V*"). Current thought is that the rotational velocity component enhances regression by increasing the total velocity of the port flow and by forcing the port flow closer to the wall resulting in an increase in the effective mass flux as seen by the wall [16, 22].

Radial and swirl end burners function similarly to other hybrids using swirling mechanisms; however, the radial and swirl end burners do not have a port in the fuel grain. Instead, the fuel grain is a cylinder with one end serving as the burning surface.

The oxidizer is injected so that recirculation zones are created in the chamber to force the oxidizer against the burning surface [16]. A drawing showing the flow patterns in a swirl injection end burning hybrid is given in Figure 1.7 [16]. Swirl end burners can result in regression rates up to 10 times that of conventional designs using HTPB. However, swirl end burners have been limited to small scale designs, and the effect of scaling on achievable regression rates is unknown [16].

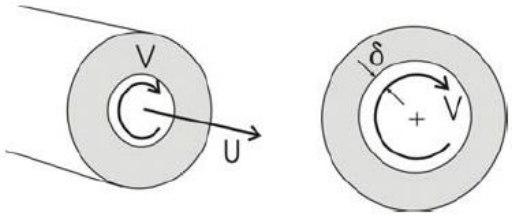

Figure 1.6. Swirling Flow [22]

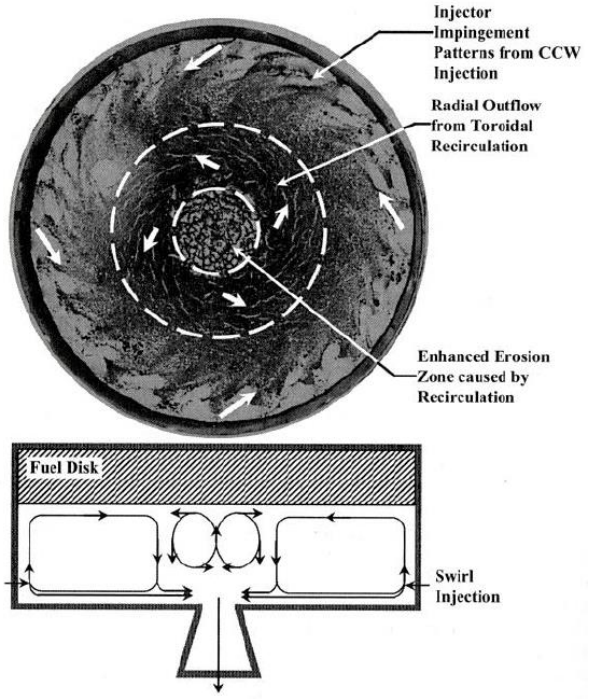

Figure 1.7. Swirl Injection End Burning Hybrid [16]

The Vortex Injection Hybrid Rocket Engine (VIHRE) is another motor design created to enhance the regression rate by using rotational flow. A drawing showing the functioning of a vortex injection hybrid is given in Figure 1.8 [23]. As can be seen in the figure, the oxidizer injection occurs at the aft end of the motor near the nozzle. Because of the swirling flow created by the injectors, a vortex is established on the outer edge of the port up against the fuel grain. This vortex climbs to the head end of the motor and then turns and creates an inside vortex down the middle of the port before exiting the nozzle. Similarly to other swirling flow type hybrids, the outer vortex in the port forces the oxidizer against the fuel grain aiding the regression [16. 23]. Experiments by Knuth et al. [23] have shown that vortex injection hybrids can result in regression rates up to 7 times that of conventional hybrids at same propellant combination and flux conditions.

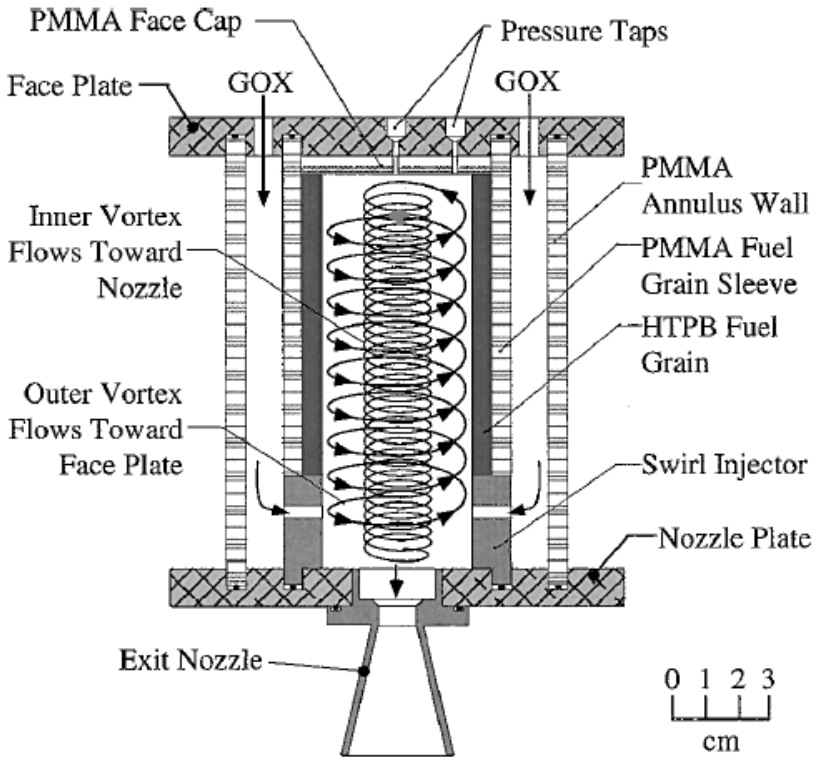

Figure 1.8. Vortex Injection Hybrid [23]

An additional means of inducing swirling motion in a hybrid rocket motor is through multi-slot injection [7, 24-25]. A model showing an injection scheme for a multi-slot injection hybrid is given in Figure 1.9 [7]. As can be seen in the figure, the oxidizer is injected at several axial locations through injectors that go through the fuel grain. These injectors are offset from the centerline to create rotational flow. Experiments by Hirata et al. [7] indicated that the regression rate enhancement using multi-slot injection is dependent upon the fuel used (either HDPE or paraffin in the cited experiment), but the regression rate is several times that of conventional designs. As a side note, Tada et al. [25] tested two multi-slot injection designs with centerline injection (i.e. without induced swirling flow in the port). While the amount of available data is limited, the regression rate of the motor with non-swirling, multi-slot injection was comparable to that of conventional designs [25, 28].

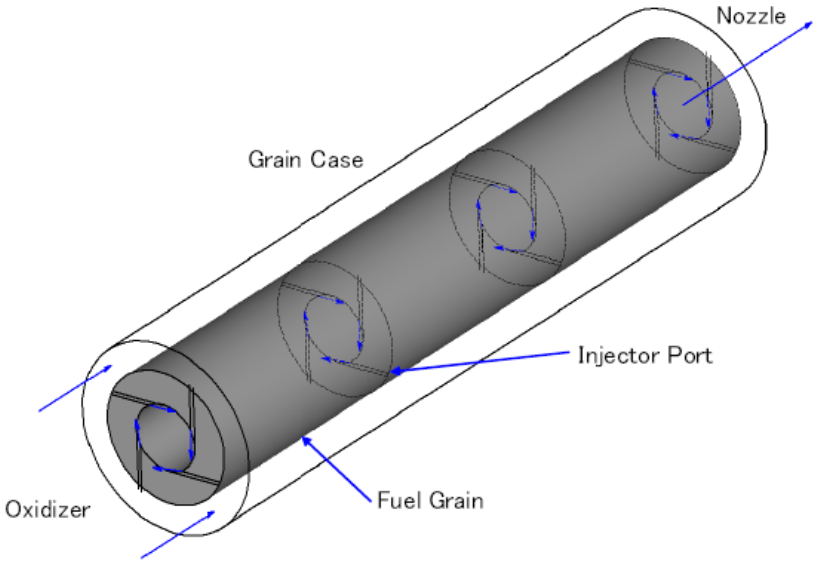

Figure 1.9. Multi-Slot Injection [7]

1.1.4 Liquefying Hybrids

Another means of enhancing the regression rate of hybrid fuel grains is by using liquefying fuels. These include the categories of cryogenic grains (such as solid methane or solid hydrogen) [16] and paraffins [27-31]. These fuels increase the regression rate by having a lower melting temperature that results in a melt layer on the fuel grain surface [29]. An example of the functioning of a liquefying fuel is shown in Figure 1.10 [29]. Liquefying fuels enhance the regression rate in two primary ways. First, the lower melting temperature (and vaporization temperature) enhances regression by requiring less heat to melt and vaporize the fuel. Second, as the oxidizer and combustion gases flow through the port, surface instability waves are established in the liquid. These waves lead to the formation and breakoff of droplets that are entrained in the flow and combust. The liquid droplets enhance regression not just by having the increased fuel mass leaving the grain but also by not significantly increasing the blocking effect since the fuel is in liquid phase [16, 29].

The primary drawback of cryogenic propellants is that significant temperature conditioning systems are required to maintain the grain in solid phase [16]. The primary drawback of paraffin fuel grains is the low structural strength of paraffin wax [16]. In addition, studies have shown that increases in the initial temperature of paraffin grains can make them susceptible to expelling unburned chunks of fuel as the softening of the grain can result in breakoff of solid pieces of the grain [27]. The use of cryogenic propellants can result in regression rates approximately four times that of HTPB [16], and the use of paraffins can increase the regression rate to approximately three to four times that of HTPB [28].

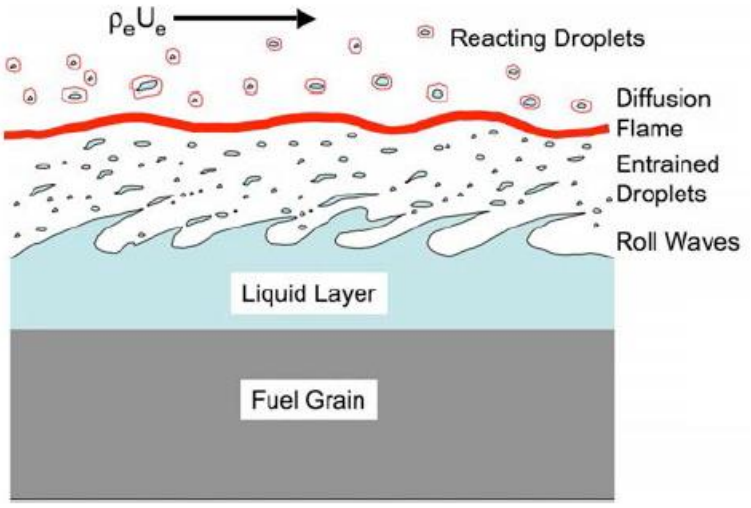

Figure 1.10. Liquefying Fuel [29]

1.1.5 Hybrid Additives

Additionally, the regression rate can be enhanced with additives in the fuel grain. Many types of additives exist including metal powders, metal hydrides, and oxidizer particles [16, 32-34]. Since each type of additive is different, general statements about additives as a whole cannot be made [16], but observations can be made for each type. For metal powders, the regression rate is mostly enhanced by increasing the radiation heat flux from the combustion products to the fuel grain [16]. Metal hydrides increase the regression rate party by the increased radiation from the metal oxides and partly by the increased heat release and reaction time of the hydrogen [32]. In addition, metal additives increase the fuel mass flow rate by increasing the fuel density.

The addition of oxidizer particles to the solid fuel grain results in what is termed a mixed hybrid [33, 35-36]. Mixed hybrids increase the regression rate by increasing the heat flux to the grain through creating a flame at the surface of the grain (thus decreasing the distance from the flame to the grain which increases the conductive heat transfer).

This flame is produced by the combustion of the oxidizer generated by the particles in the grain with the fuel vaporizing off the grain surface. The regression rate can be increased even more through the use of additives in addition to the oxidizer particles [33].

Frederick et al. [33] tested six formulations of HTPB with ammonium perchlorate (AP) and Fe_2O_3 (aka rust) added to the grain plus a pure HTPB fuel. In the tests, the AP was varied from 25-30% of the grain mass, and the additive was varied from 0-5% of the grain mass. Results of the tests are shown in Figure 1.11 [33]. As can be seen in the figure, the regression rate of the mixed hybrid without Fe_2O_3 was increased by 41-76% as compared to the baseline HTPB grain without additives. By adding Fe_2O_3 to the mixed hybrid, increases of regression rates of up to 325% over the baseline HTPB were experienced [33].

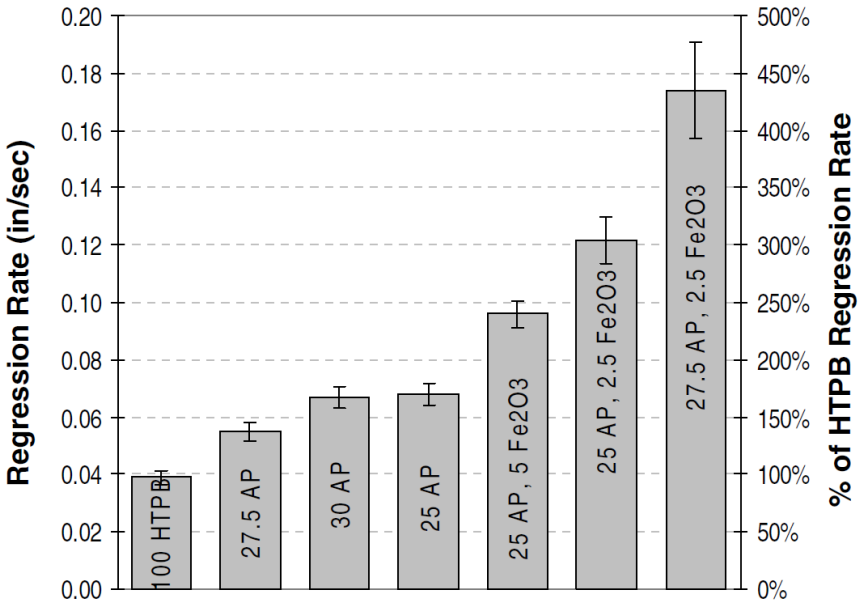

Figure 1.11. Mixed Hybrid Performance with Gaseous Oxygen (G_{ox} = 0.3 lb_m/in^2-s and P_{ch} = 350 psi) [33]

1.1.6 Double-tube Hybrids

A new design for hybrid fuel grains is what is termed the "double-tube" hybrid. A computational simulation of the double-tube design was presented at the 2014 AIAA Propulsion and Energy Forum [37], and an experimental investigation was presented at the 2015 AIAA Propulsion and Energy Forum [38]. Simulations were performed using a three dimensional model that included such effects as turbulence, fuel pyrolysis, and combustion [37]. Two main versions of the double tube configuration have been simulated. The first version functions as a conventional motor design with a fuel grain with head-end injection but with an inner tube added to provide additional oxidizer injection. The injection from the inner tube is oriented toward the fuel grain to aid in forcing the oxidizer toward the grain surface. The second version of the double-tube hybrid is the same as the first version except that an additional grain is placed on the outside of the inner tube resulting in two grain surfaces exposed to the oxidizer in the port. The injection holes in the inner tube could be either straight or canted [37]. A drawing of an experimentally tested scheme of the second version with canted inner tube injection ports as well as a graph of regression rate results from the computational simulations are given in Figure 1.12 [37-38].

As can be seen in the graph of the results, the double-tube design is predicted to increase the regression rate as compared to conventional grains. Of interest in double-tube regression is that the regression rate is not just dependent on the total oxidizer flux but also on the ratio of the oxidizer flow rate injected through the inner tube to the total oxidizer flow rate injected into the port (from both head-end and inner tube injection) [37]. The predicted increase of the regression rate was validated experimentally for a

condition with an inner injector cant angle of 135° and an oxidizer flow rate bypass ratio of one (the condition when all oxidizer is injected through the inner tube injection ports) [38].

Due to dependence of the regression rate on the oxidizer flow ratio and the total oxidizer flux, the double-tube design has two parameters to control the regression rate while maintaining a single oxidizer tankage system. As such, the double-tube introduces the potential for controlling the mixture ratio during throttling as the oxidizer flow ratio can be adjusted during throttle to tune the regression rate to obtain the desired mixture ratio. [37]

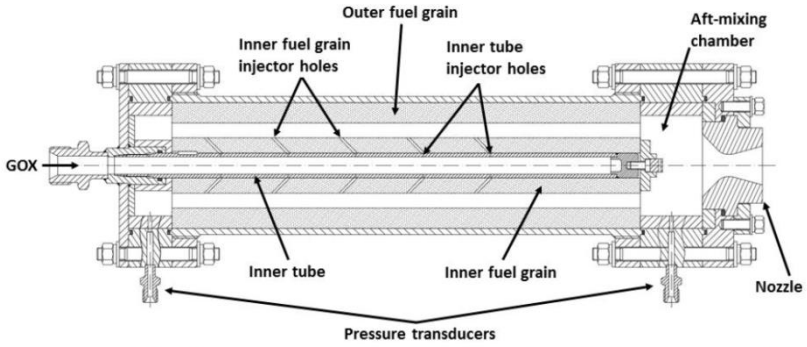

Figure 1. Scheme of the laboratory-scale hybrid rocket motor with double-tube configuration (DT) and without inserts.

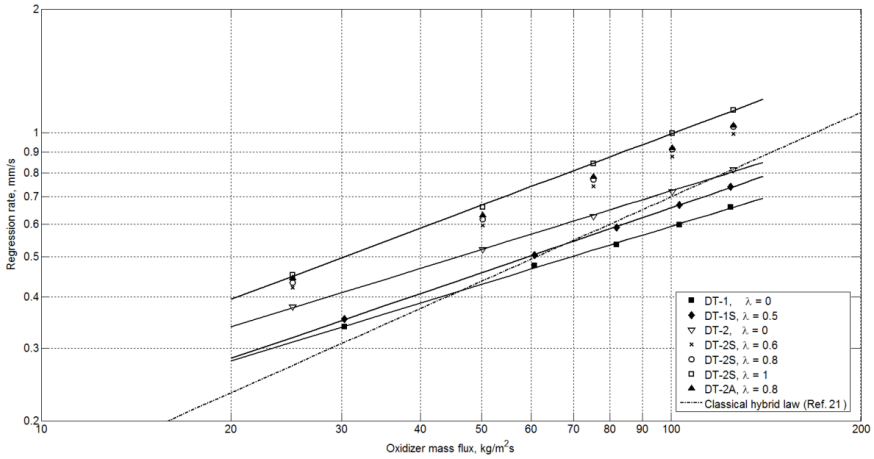

Figure 6. Regression rate as a function of oxidizer mass flux.

Figure 1.12. Double-tube Hybrid Motor [37-38]

1.1.7 Axial-Injection, End-Burning Hybrids

Another experimentally tested design to increase the regression rate of hybrid fuel grains is the axial-injection, end-burning hybrid rocket motor [39-41]. In the axial-injection, end-burning design, the oxidizer is flowed through a porous or fibrous grain to the surface where combustion occurs. This design is in contrast to the "wet towel" hybrid where the fibrous grain was soaked in a liquid oxidizer prior to ignition [39]. A drawing showing the design of the axial-injection, end-burning hybrid is given in Figure 1.13 [39]. A fundamental aspect of the axial-injection, end-burning hybrid is the presence of tubes or pores in the fuel grain to deliver the oxidizer to the combustion surface. These pores can reduce the effective density of the grain requiring any increase in the regression rate to also offset the decrease in effective density to increase the delivered fuel mass flow rate. However, since the grain fills the entire combustion chamber, the decrease in effective density is partly balanced by an increased loading of the combustion chamber (the wagon wheel design shown in Figure 1.3 has an approximately 75% volumetric loading). Decreases in the effective density are not considered to be too significant a difficutly as Nagata et al. [41] successfully fired an additively manufactured grain with an approximately 95% effective density/volumetric loading.

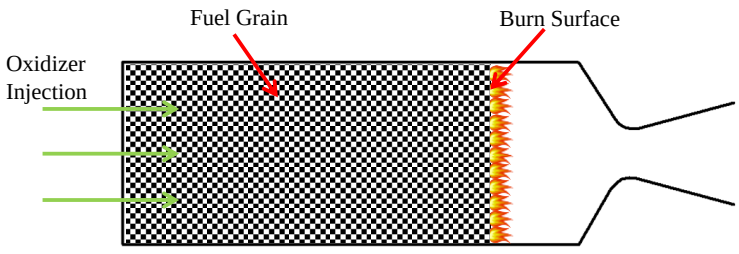

Figure 1.13. Axial-Injection, End-Burning Hybrid [39]

Nagata et al. evaluated the axial-injection, end-burning design using both polyethylene tubes [40] and fibrous filters [39] as the hybrid fuel. Testing indicated that for the axial-injection, end-burning configuration there was an upper critical oxidizer velocity above which the flame would experience blow-off (resulting in extinguishment of the propellant) and a lower critical oxidizer velocity below which the flame would creep back into the grain. Between those two critical oxidizer velocities, the flame would sit at the surface of the grain, and the grain regression rate was a function of the chamber pressure to an exponent (St. Robert's Law) as opposed to the oxidizer mass flux to an exponent [39-40].

Test conditions for the tests using the polyethylene tubes and Schlieren images of the combustion are shown in Table 1.1 and Figure 1.14 [40]. As can be seen in the table, two inner diameter tubes were used in the testing. Type-A had a 2 mm inner diameter and type-B had a 0.5 mm inner diameter giving a ratio of the area of type-A to the area of type-B of 16. The effect of the increase in area is shown in the Schlieren images in Figure 1.14. The type-A tube (left side) exhibits a dark core in the oxidizer flow at the exit which is not seen in the type-B tube (right side). This dark core is uncombusted oxidizer and is caused by the inability of the oxidizer to mix and combust with the vaporized fuel [40]. Nagata et al. speculated that using a mesh or fibers would break up the oxidizer core thus enhancing the performance of larger area tubes [40].

Table 1.1. Polyethylene Axial-Injection, End-Burning Hybrid Data [40]

	type-A	type-B
Material	Polyethylene	Polyethylene
Configuration	ID = 2 mm OD = 4 mm	ID = 0.5 mm OD = 3.1 mm
Boiling Point	440-450 ℃	430-440 ℃
Density	0.94-0.96 g/cc	0.94-0.96 g/cc

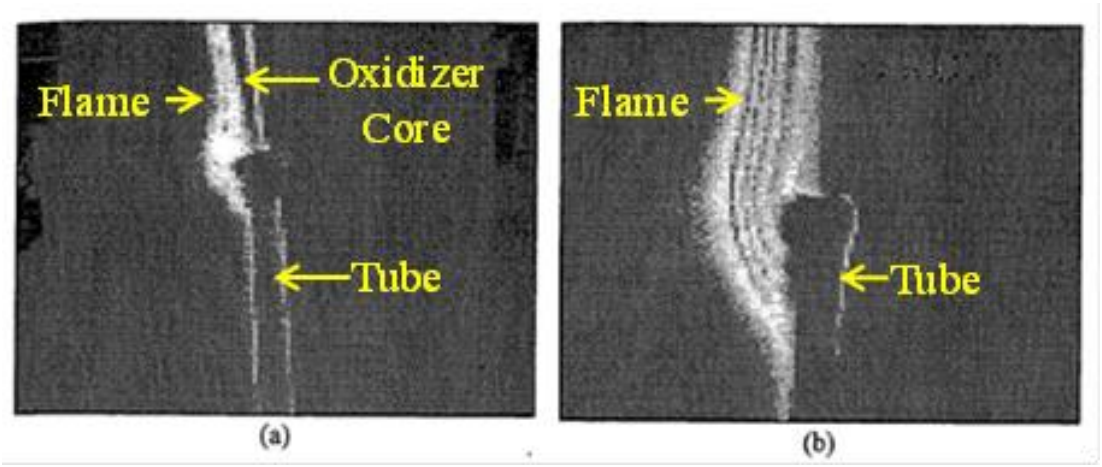

Figure 1.14. Schlieren Images of Burning Polyethylene Tubes in Atmospheric Pressure [(a): type-A tube, (b): type-B tube] [40]

Results from the tests using the polyethylene tubes are shown in Figure 1.15 [40]. The plot in the upper left shows the burning regimes for the type-B tube. In the plot, the upper and lower critical velocities can be seen to be a function of the chamber pressure. On the upper right is a plot showing the regression rate at atmospheric pressure for both type-A and type-B tubes. As can be seen in the plot, above a threshold velocity, the

regression rate of the type-B tubes is relatively constant over the range of flow rates tested while the regression rate of the type-A tubes peaked and then decreased with increasing velocity. The exact cause is unknown, but Nagata et al. [40] postulated that the reason was the increased difficulty of the oxidizer to mix and combust with the fuel at higher velocities when using larger exit areas.

The plot in the lower left of Figure 1.15 shows the regression rate of type-B tubes for the range of velocities and pressures tested. As can be seen in the plot, the regression rate increases with increasing pressure but is relatively constant with respect to velocity (there is scatter in the data, but the trend is relatively constant).

Finally, the equivalence ratio with respect to velocity for the type-B tubes is shown in the lower right of the figure. Since the fuel regression is relatively constant with respect to oxidizer velocity and is only a function of pressure, the equivalence ratio changes with changes in the oxidizer flow since the fuel flow is constant. As can be expected, the equivalence ratio is inversely related to the oxidizer flow since increasing the oxidizer flow makes the combustion more oxidizer rich which is indicated by decreasing equivalence ratios (as indicated by Eq. 1.5) [40]. While suffering the same scaling uncertainty as the swirl injection end burner due to only having been tested at a laboratory scale, the axial-injection, end-burning configuration can yield regression rates up to 10 times that of conventional hybrid designs [16, 40].

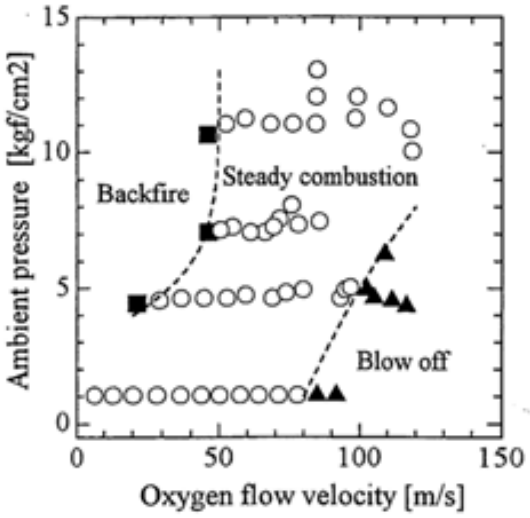

Fig. 5. Upper and lower critical velocities. Fuel tube of type-B is used.

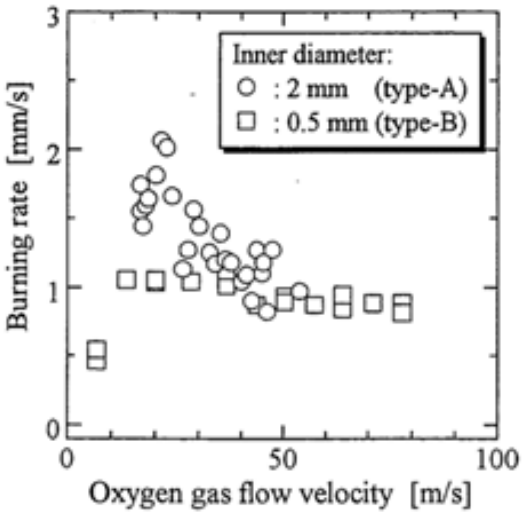

Fig. 6. Burning rates in the atmospheric pressure.

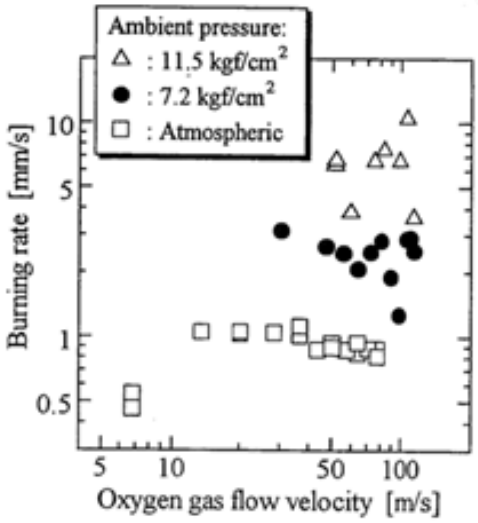

Fig. 8. Burning rates in high pressures. Fuel tube of type-B is used.

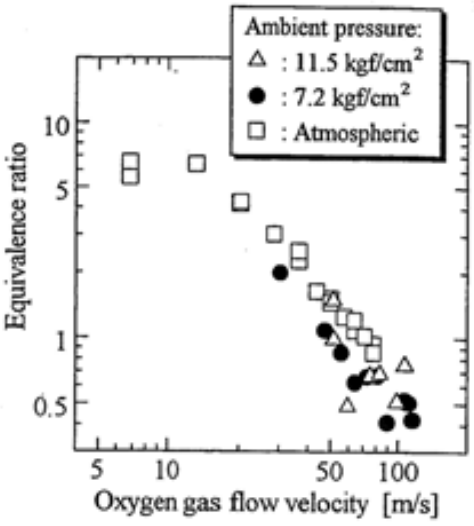

Fig. 9. Resultant equivalence ratios. Fuel tube of type-B is used.

Figure 1.15. Polyethylene Axial-Injection, End-Burning Performance [40]

The described pressure dependency of the axial-injection, end-burning configuration has been speculated to result from the motor burning more similarly to a solid rocket motor than a hybrid rocket motor [39]. Such a result would be expected not

only from the regression law similarity but also from the configuration's lacking the diffusion-controlled, boundary layer flame typically seen in hybrid rocket motors which would result in a different flame structure. Such a difference suggests the necessity of investigating flame models from solid rocket motors to fully understand the physical mechanisms driving the results observed by Nagata et al. [39-40].

Another consideration for the axial-injection, end-burning configuration is that the oxidizer ports reduce the effective density of the material. As such, any fuel mass flow rate calculations would need to be based on the actual fraction of the end surface that consists of solid material, or if the total end surface area is used, an effective fuel density including the pores would need to be used. A final implication of the pressure dependent regression rate of the axial-injection, end-burning configuration is that the fuel mass flow rate is decoupled from the oxidizer mass flux. This decoupling has been observed in experimental firings of additively manufactured axial-injection, end-burning hybrid rocket motors by Nagata et al. [41].

In contrast to the results of Nagata et al., a recent investigation was published by Li et al. [42] on axial-injection, end-burning hybrid rocket motors that stated the regression rate of axial-injection, end-burning hybrids was lower than that of conventional hybrids. In this study, Li et al. evaluated the regression rate of polymethyl methacrylate and polyethylene fuel grains with axial ports for the oxidizer to flow to the burning surface. In their experiment, the axial ports were small compared to the fuel grain diameter and were confined to the center of the grain as opposed to being evenly spaced throughout the grain. Results from the tests indicated two oxidizer transition velocities. Below the lower transition velocity, the flame was absorbed into the ports and

the grains burned as a conventional hybrid. Between the two transition velocities, the flame stabilized at the outlets of the ports resulting in combustion near the exit of the ports. Finally, above the upper transition velocity, the flame existed outside of the ports yielding an end-burning configuration. Using the mass loss from each test, Li et al. determined that the end-burning configuration yielded a lower regression rate than did the conventional configuration [42].

In addition, preliminary studies of an axial-injection, end-burning style configuration were conducted in the 1960's by McAlevy and Lee [43] and McAlevy et al. [44]. In these studies, tests were performed using solid oxidizer particles with a gaseous fuel, using solid fuel particles with GOX [43], and powdered or mesh aluminum with GOX [44]. In both studies, experiments were only performed at atmospheric or subatmospheric pressures. As such, while an increase in the regression rate was observed, no pressure correlations were developed to describe the regression rate. Of particular interest in the aluminum studies was that the regression rate of the grain when using different particle sizes was evaluated. Results from these studies indicated that after accounting for the effect of different void fractions on the solid fuel density, the regression rate increased with decreasing fuel particle or wire diameters [44]. Such an effect would indicate that the smaller diameters aided the regression rate in some manner potentially by reducing the diffusion process.

1.1.8 Hybrid Regression Enhancement Summary

In summary several different designs have tested for use in hybrid rocket designs. A table summarizing key features of some of the designs discussed in this chapter is shown in Table 1.2. Each of the strategies to enhance the regression rate ties back to the

energy balance shown in Figure 1.4. This can be accomplished through increasing the convective heat flux, conductive heat flux, or the radiative heat flux or by decreasing the heat requirement to pyrolize or vaporize the fuel. Increasing the convective heat flux can be achieved through the addition of swirl to the oxidizer injection. Increasing the conductive heat transfer can be achieved by altering the processes that move the flame closer to the grain. One method of doing this is to introduce the oxidizer through the fuel grain directly into the combustion region like in the axial-injection, end-burning configuration as opposed to a conventional hybrid where the oxidizer has to diffuse through the boundary layer. Increasing the radiation heat flux can be achieved by metalizing the fuel or by choosing a fuel with sooty combustion products. Finally, decreasing the heat requirement to pyrolize or vaporize the fuel is easily performed by selecting a fuel with a low decomposition enthalpy requirement.

Most of the experimentally tested designs with a flux-dependent regression rate suffer from mixture ratio shifting; but, by having two independent oxidizer injection systems, the double-tube design offers the possibility to control mixture ratio during motor throttling [37]. Likewise, since it has a pressure-dependent regression rate, the axial-injection, end-burning design does not suffer from mixture ratio shifting during operation.

Table 1.2. Regression Enhancement Summary

Type	Regression ($\dot{r}/\dot{r}_{HTPB}$)	O/F Control in Throttle	Hazard	Notes	Enhancement Mechanism	Ref
HTPB	1	No	Inert	Usually Multi-Port	-----	[1]
Printed ABS	0.92	No	Inert	More Dense than HTPB	-----	[6], [8]
Polyethylene	~0.9	No	Inert	Several Types	-----	[1], [7]
VIHRE	4 – 7	No	Inert	Uncertain Scaling	Increases Convective Heat Flux	[16], [23]
Mixed Hybrid	1.4 – 1.75	No	AP	Not Inert	Increases Conductive Heat Flux	[33]
Metal Additives	1.2 – 1.62	No	Inert	Additive Specific	Increases Radiation Heat Flux	[15-16], [32], [34]
Cryogenic	4 – 5	No	Low Temps	Cryogenic Temperatures	Decreases Pyrolysis Heat Req.	[16]
Paraffin	2.5 – 3.5	No	Inert	Low Structural Strength	Decreases Pyrolysis Heat Req.	[16], [28-30]
Swirl End Burner	10	No	Inert	Small Scale	Increases Convective Heat Flux	[16]
Axial-Injection End Burner	10	No	Inert	Small Scale	Increases Conductive Heat Flux	[16], [39-40]
Double-tube	1.5	Yes	Inert	Two Grains	Increases Convective Heat Flux	[37-38]

While several approaches show improvement compared to conventional hybrids using HTPB, ABS, or polyethylene, most improvements are not sufficient to make hybrids a practical choice based on improvements related to increases in mass fraction. Howbeit, a few designs have a significant regression rate including the vortex injection hybrid, the swirl injection end burner, and the axial-injection, end-burning hybrid. The axial-injection, end-burning hybrid shows potential as a possible hybrid motor configuration, but its regression rate for designs larger than 0.5 mm ID tubes would need to be investigated. Additionally, since the main concern of increasing the regression rate of hybrid rocket motors is to increase the fuel mass flow rate which is a function of the burn area, the fuel density, and the regression rate, any design that increases the regression rate must maintain a sufficient density so that the fuel mass flow rate is increased.

The axial-injection, end-burning configuration has shown significant potential for augmenting the regression rate of hybrid rocket motors. However, there is limited data in the literature regarding the performance of the configuration, and the data that do exist conflict regarding whether or not the design does indeed augment the regression rate. In addition, while it has been hypothesized that this configuration burns like a solid rocket motor due to the pressure dependency of the regression rate, no physical model has been proposed to explain that dependency.

Finally, all experimental tests of the axial-injection, end-burning configuration have used gaseous oxygen (GOX) as the oxidizer. As such, opportunities regarding this configuration include performing basic tests using gaseous oxygen to evaluate the competing claims in the literature, developing a heat balance model to include the effects

of oxidizer flow though the grain, applying a flame model to explain the physical mechanisms driving the pressure dependency of the regression rate, and conducting experiments using a different oxidizer to evaluate the augmentation of the regression rate with a non-GOX oxidizer.

1.2 Objective and Significance of Research

The objective of this research is to investigate the combustion and heat mechanisms controlling regression rate of axial-injection, end-burning hybrid fuel grains with laboratory-scale experimentation and to describe them with an analytical ablative model. The study is designed to evaluate the effect of oxidizer flow rate and chamber pressure on the fuel regression rate. By comparing the experimental results with the modified ablative model, a better understanding of how the various test parameters and physical processes contribute to the regression rate will be determined. The analytical model includes the dominant effects that are hypothesized to control the combustion including oxidizer flow rate and conduction from diffusion and kinetically controlled flames. This study does not include the effects of cross flow on the combustion process. The main research contribution of this work is evaluating conflicting results in the literature, conducting the first experiments of an axial-injection, end-burning hybrid with nitrous oxide as the oxidizer, developing a new analytical model for this configuration, and applying a solid rocket motor flame model to provide a physical explanation of the flame structure in a porous axial-injection, end-burning hybrid rocket motor.

CHAPTER 2

MODEL AND TEST ARTICLE DESIGN

To better understand the physics behind the fuel regression rate of the axial-injection, end-burning hybrid motor configuration, a theoretical model was developed using a basic ablation model as a foundation. Using the model, general observations were made regarding the effect of oxidizer flow on the grain regression. In addition, an estimation for the flame standoff from the fuel grain surface was calculated by adapting the Granular Diffusion Flame (GDF) model used for solid rocket motors. The GDF model was selected as it accounted for both kinetic and diffusion contributions to the flame distance and provided insight into the pressure dependence of the regression rate observed in the literature.

2.1 Ablative Model

To describe the regression rate of the fuel grain, a basic ablative model was investigated for applicability. A sketch showing the basics of ablation is shown in Figure 2.1 [45]. In an ablation model, it is assumed that the control volume boundary is moving such that the boundary inside the fuel ("*o*" in the figure) maintains an adiabatic condition (q_o is zero). All heat transferred into the fuel (q_s) goes toward increasing the solid fuel temperature from the initial temperature ("*o*" condition) to the surface temperature ("*u*" condition) and then sublimating it ("*s*" condition). It is assumed that all vaporized fuel

leaves the control volume, but no required mechanism is specified. In addition, no source for the heat transfer to the surface is specified for the basic ablative thermodynamic model.

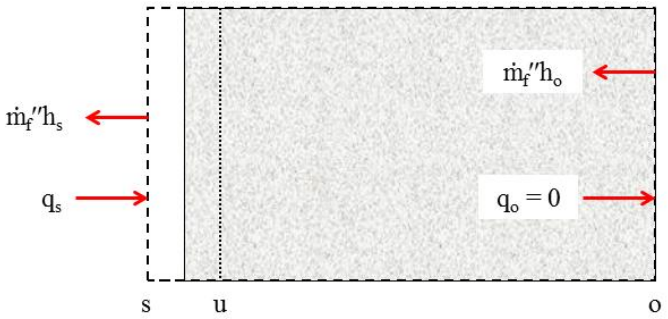

Figure 2.1. Ablative Melting [45]

Using an energy balance for the ablative model, the mass flux of the vaporized fuel can be expressed using the equation

$$\dot{m}_f'' = \frac{q_s}{h_{fs}+c_{p,f}(T_s-T_o)} \tag{2.1}$$

where $\dot{m}_f''$ is the fuel mass flux, q_s is the heat transfer to the surface per unit area, h_{fs} is the enthalpy required for sublimation, $c_{p,f}$ is the specific heat of the fuel, T_s is the surface temperature, and T_o is the initial temperature. As can be seen in Eq. 2.1, the mass flux of the fuel is equal to the rate of the heat transferred to the fuel divided by the enthalpy required to vaporize the fuel.

For an axial-injection, end-burning hybrid, not only is the fuel present in the grain, but the oxidizer is also present as it flows through the tubes or porous material. To account for the change, the basic ablative model was extended to add oxidizer flow and the potential for a liquid layer as some fuels could melt to create liquid film on the

surface that vaporizes as opposed to sublimating directly. A drawing of the modified model is shown in Figure 2.2. As can be seen in the figure, the modified ablative model with porous flow maintains the moving control volume and adiabatic condition of the basic ablative model. However, the modified model adds a mass flux term for the oxidizer flow and adds additional surfaces to account for additional phase changes. These surfaces include the "m" surface where the solid is at the melting temperature, the "*a*" surface where the fuel has melted to form a liquid at the melting temperature, the "*e*" surface where the liquid was been heated to the vaporization temperature, and the "*s*" surface where the fuel is a vapor at the vaporization temperature. Assumptions for the modified ablative model include

- Steady state,
- Uniform porosity and equal distribution of pores across surface,
- No phase change in the oxidizer (e.g. gaseous oxidizer),
- Oxidizer temperature controlled by heat transfer from the fuel grain,
- Uniform fuel distribution and density,
- Uniform heat transfer to burn surface (no preferential heating of parts of burning surface),
- Interface temperatures between phases are equal to phase change temperatures,
- Constant properties,
- No liquid entrainment (all fuel leaves control volume as vapor), and
- Flame occurs at an equivalence ratio of one. [35]

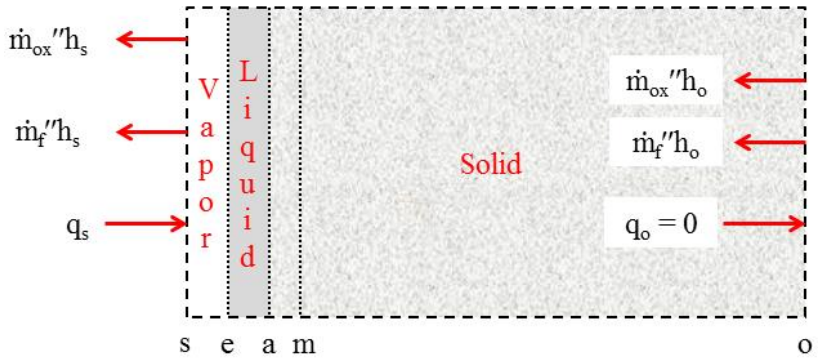

Figure 2.2. Ablative Melting with Porous Flow

Performing an energy balance on the modified ablative model shown in Fig. 7 results in the equation

$$q_s = \dot{m}_f''\left(h_{f,s} - h_{f,o}\right) + \dot{m}_{ox}''\left(h_{ox,s} - h_{ox,o}\right) \tag{2.2}$$

where $h_{f,s}$ is the enthalpy of the fuel at the "s" surface, $h_{f,o}$ is the enthalpy of the fuel at the "*o*" surface, $\dot{m}_{ox}''$ is the oxidizer mass flux, $h_{ox,s}$ is the enthalpy of the oxidizer at the "*s*" surface, and $h_{ox,o}$ is the enthalpy of the oxidizer at the "*o*" surface. Equation 2.2 can be expanded to account for the enthalpy of the fuel at the additional surfaces to yield the equation

$$q_s = \dot{m}_f''\left(h_{f,s} - h_{f,e} + h_{f,e} - h_{f,a} + h_{f,a} - h_{f,m} + h_{f,m} - h_{f,o}\right) + \dot{m}_{ox}''\left(h_{ox,s} - h_{ox,o}\right) \tag{2.3}$$

where $h_{f,e}$ is the enthalpy of the fuel at the "*e*" surface, $h_{f,a}$ is the enthalpy of the fuel at the "*a*" surface, and $h_{f,m}$ is the enthalpy of the fuel at the "*m*" surface. By combining some of the fuel enthalpy terms, the enthalpy changes can be expressed in terms of the latent heats of the fuel. This is shown in the equation

$$q_s = \dot{m}_f''\left(\Delta h_{f,dec} + \left(h_{f,e} - h_{f,a}\right) + \Delta h_{f,melt} + \left(h_{f,m} - h_{f,o}\right)\right)$$

$$+\dot{m}''_{ox}\left(h_{ox,s} - h_{ox,o}\right) \tag{2.4}$$

where $\Delta h_{f,dec}$ is the enthalpy required to decompose the fuel from a liquid to a vapor (equivalent to the latent heat of vaporization if no decomposition is required) and $\Delta h_{f,melt}$ is the latent heat of fusion of the fuel. Expressing the enthalpy in terms of latent heats simplifies solving the equation as it gives the equation in known physical properties of the fuel. Further simplification can be achieved using the assumption of constant properties to express enthalpy differences in terms of the specific heat times a temperature difference. This substitution along with expressing the fuel mass flux in terms of the fuel density times the regression rate yields the equation

$$q_s = \rho_f \dot{r}\left(\Delta h_{f,dec} + c_{liq}\left(T_{f,e} - T_{f,a}\right) + \Delta h_{f,melt} + c_{sol}\left(T_{f,m} - T_{f,o}\right)\right)$$
$$+\dot{m}''_{ox}\left(h_{ox,s} - h_{ox,o}\right) \tag{2.5}$$

where c_{liq} is the specific heat of the liquid fuel, $T_{f,s}$ is the temperature of the fuel at the "*s*" surface, $T_{f,a}$ is the temperature of the fuel at the "*a*" surface, c_{sol} is the specific heat of the solid fuel, $T_{f,m}$ is the temperature of the fuel at the "*m*" surface, $T_{f,o}$ is the temperature of the fuel at the "*o*" surface, $c_{p,ox}$ is the specific heat at constant pressure of the oxidizer, $T_{ox,s}$ is the temperature of the oxidizer at the "*s*" surface, and $T_{ox,o}$ is the temperature of the oxidizer at the "*o*" surface. Since the surfaces are located at phase change locations as described previously and since the oxidizer temperature is assumed to equal the fuel temperature at each location, the temperatures for the fuel phase changes can be substituted into Eq. 2.5 which yields the equation

$$q_s = \rho_f \dot{r}\left(\Delta h_{f,dec} + c_{liq}(T_{dec} - T_{melt}) + \Delta h_{f,melt} + c_{sol}(T_{melt} - T_o)\right)$$
$$+\dot{m}''_{ox}\left(h_{ox,s} - h_{ox,o}\right) \tag{2.6}$$

where T_{dec} is the fuel decomposition temperature, T_{melt} is the fuel melting temperature, and T_o is the initial temperature of the fuel. This further ties the equation to physical properties of the fuel grain which aids the analysis as the assumption that the surface temperatures are equal to the phase change temperatures reduces the number of temperature measurements required for the analysis.

At this point, no assumption has been made regarding the means of heat transfer to the grain. Due to uncertainty in the relative strengths of the various heat transfer mechanisms, it was determined not to initially treat each method of heat transfer individually but group them all into an effective heat transfer coefficient. As such the following correlation was used to describe the heat transfer to the surface

$$q_s = C_{fl}\left(T_{fl} - T_{dec}\right) \tag{2.7}$$

where C_{fl} is the "flame coefficient" (an effective heat transfer coefficient) and T_{fl} is the temperature of the flame. Finally, the expression for the heat transfer shown in Eq. 2.7 can be substituted into the modified ablative model expressed in Eq. 2.6 to yield the equation

$$C_{fl}\left(T_{fl} - T_{dec}\right) = \rho_f \dot{r}\left(\Delta h_{f,dec} + c_{liq}(T_{dec} - T_{melt}) + \Delta h_{f,melt} + c_{sol}(T_{melt} - T_o)\right) + \dot{m}''_{ox}\left(h_{ox,s} - h_{ox,o}\right) \tag{2.8}$$

where all terms have been previously defined. Rearranging Eq. 2.8 results in the equation

$$\rho_f \dot{r} = \frac{C_{fl}\left(T_{fl} - T_{dec}\right) - \dot{m}''_{ox}\left(h_{ox,s} - h_{ox,o}\right)}{\left(\Delta h_{f,dec} + c_{liq}(T_{dec} - T_{melt}) + \Delta h_{f,melt} + c_{sol}(T_{melt} - T_o)\right)} \tag{2.9}$$

where all terms have been previously defined. Finally, Eq. 2.9 can be simplified by combining the enthalpy required to change the fuel from a solid at a reference

temperature (298 K) to a vapor at the decomposition temperature and by adding the enthalpy difference of the solid fuel at the intial temperature from the reference temperature. These changes result in the equation

$$\dot{r}\rho_f = \frac{C_{fl}(T_{fl}-T_{dec})-\dot{m}''_{ox}(h_{ox,s}-h_{ox,o})}{(\Delta h_{tot}+c_{sol}(298K-T_o))} \tag{2.10}$$

where Δh_{tot} is the combined fuel enthalpy change requirement which can be found for polyethylene in the literature [46]. The expression shown in Eq. 2.10 follows the same format of the basic ablative model given in Eq. 2.1 where the fuel mass flux is equal to the heat transferred to the fuel divided by the enthalpy required to heat and vaporize the fuel. However, as seen in the modified ablative model shown in Eq. 2.10, the presence of the oxidizer flow reduces the fuel regression as some of the heat goes to heat the oxidizer instead of vaporizing the fuel. Heat transfer from the fuel to the oxidizer is assumed to occur by internal convection from the grain to the oxidizer based on an assumed thermal soak of the fuel grain as given in a standard ablative model [45]. For simplicity, a uniform temperature was used for the fuel grain based on the thermal soak and cooling of the fuel grain was neglected. In addition, the initial temperature of the fuel and the oxidizer are assumed to be equal and given by the oxidizer injection temperature. Any benefit in fuel regression provided by the porous oxidizer flow setup must come from increasing the heat flux from the flame as without any heat transfer increase, the oxidizer flow results in a regression rate reduction.

By rearranging Eq. 2.10, an explicit relationship for the flame coefficient can be found. This yields the equation

$$C_{fl} = \frac{\dot{r}\rho_f(\Delta h_{tot}+c_{sol}(298K-T_o))+\dot{m}''_{ox}(h_{ox,dec}-h_{ox,o})}{(T_{fl}-T_{dec})} \tag{2.11}$$

where everything has been defined previously. By solving for the flame coefficient at each test condition, correlations can be determined to gain insight into trends to better understand the underlying physics behind the combustion of axial-injection, end-burning hybrid rocket motors.

2.2 Flame Standoff Calculations

In an endeavor to better understand the physical parameters driving the regression rate of the fuel, a means of modeling the heat transfer from the flame to fuel surface was required. Three primary possibilities were investigated; these possibilities were a flat flame model, the Beckstead-Derr-Price (BDP) model, and the Granular Diffusion Flame (GDF) model. After evaluating the different models and the underlying assumptions and configuration, it was determined to use the GDF model as the basis for the flame model.

2.2.1 Flat Flame Model

In this situation, a flat flame model would be based on the assumption that the flame is a premixed flame [47]. This would be achieved by assuming that the grain was uniformly porous with equal distribution of pores thus having no oxidizer concentration gradients above the surface and that the fuel grain experienced uniform regression resulting in no fuel concentration gradients above the surface and that the fuel and the oxidizer would be sufficiently mixed exiting the grain surface to neglect any requirement for diffusion. In addition, it would be assumed that the flame was laminar instead of turbulent. These would allow for estimating the flame as one produced by a premixed, flat flame burner.

One method of calculating the standoff distance of a premixed, flat flame burner that was investigated was using the standoff Peclet number as presented by Ferguson and Keck [48]. The standoff Peclet number for this approach is given using the equation

$$Pe = \frac{\rho_u S_L (c_{p,u} + c_{p,b}) x}{k_u + k_b} \tag{2.12}$$

where Pe is the Peclet number, ρ_u is the density of the unburned gases, S_L is the flame speed, $c_{p,u}$ is the specific heat at constant pressure of the unburned gases, $c_{p,b}$ is the specific heat at constant pressure of the burned gases, x is the standoff distance, k_u is the thermal conductivity of the unburned gases, and k_b is the thermal conductivity of the burned gases. In this setup, the Peclet number represents the relative ratio of the convective rate to the conductive rate. For this calculation of the standoff distance, the Peclet number would need to be estimated using the Ferguson and Keck's plot shown in Figure 2.3 [48] since the Peclet number shown in Eq. 2.12 cannot be solved directly as the flame distance is unknown. In Figure 2.3, the x-axis represents a non-dimensional temperature based on the heat transfer to the burner to stabilize the flame where T_b is the temperature of the burned gases, T_b^o is the adiabatic flame temperature (at the premixed condition), and T_u is the temperature of the unburned gases. One noticeable challenge in estimating the Peclet number is the scatter observed in Figure 2.3 at the larger values of the non-dimensional temperature.

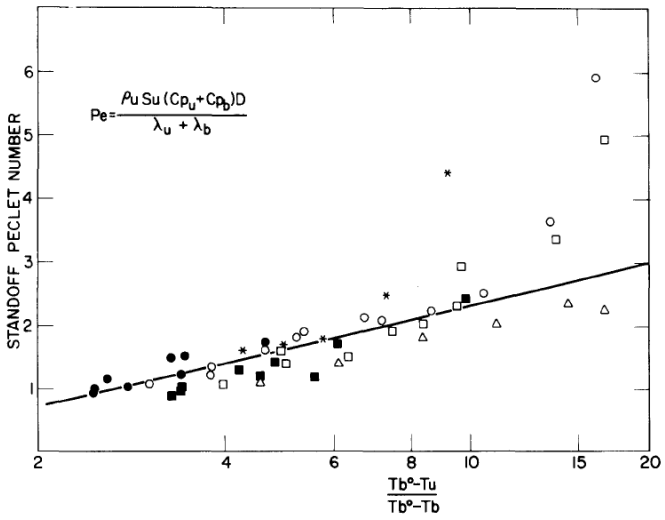

Figure 2.3. Premixed Flat Flame Standoff Peclet Number [48]

After estimating the Peclet number, it would also be required to estimate the flame speed. As a first order approximation, this could be performed using the values for ethylene and air as fuel/air flame speed data is common [49-50]. A plot showing the flame speed of ethylene and air at stoichiometric conditions as a function of pressure is shown in Figure 2.4 [49]. However, this approximation would be limited by the presence of nitrogen in the air as well as the laminar flame assumption mentioned previously.

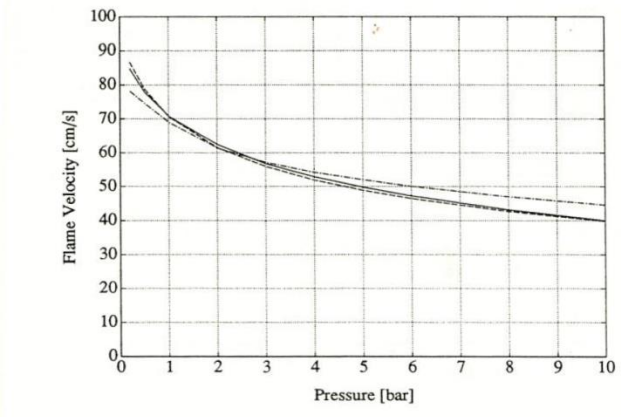

Figure 2.4. Ethylene-Air Flame Speed [49]

While some information could be gained from the flat flame model approach, it was determined that the estimations required for the approach involved too many assumptions and that the diffusion process neglected in the premixed assumption could be significant. As such, the flat flame model was deemed to be insufficient for modeling the flame. Therefore, emphasis was placed on investigating existing solid rocket motor flame models that included both kinetic and diffusion processes as they were considered to have greater applicability to the axial-injection, end-burning configuration.

2.2.2 Beckstead-Derr-Price

The BDP model was proposed to describe the combustion process of composite solid rocket fuels [51]. This model is based on a solid ammonium perchlorate (AP) oxidizer particles embedded in a matrix of solid fuel. Unlike later models, such as the Petite Ensemble Model, the BDP model assumes a statically-averaged particle diameter presenting itself at the burning surface. A picture of the assumed flame structure of the BDP model is shown in Figure 2.5. Assuming AP as the oxidizer is key to the model as AP produces a monopropellant decomposition flame. This results in a three flame structure as shown in the figure. The first flame is the AP monopropellant flame that results in oxidizer-rich combustion products. The second flame is the primary flame that occurs on the borders between the oxidizer particles and the fuel particles which results in fuel-rich combustion products. Lastly, there is the final diffusion flame which results from the combustion of the oxidizer-rich and fuel-rich products of the other two flames. All flames in the BDP model are estimated as flat flames for purposes of calculating the heat transfer to the motor. The flame structure described in the BDP model is termed a "competing" flame structure due to the relative positions of the three flames as a function

of pressure. At low chamber pressures, the location of the final flame is below that of the AP monopropellant flame thus eliminating the AP monopropellant flame from consideration. The three flame structure as given in Figure 2.5 occurs as the chamber pressure increases sufficiently so that the AP monopropellant flame occurs before the final flame [51]. While the BDP model provides useful insight into the combustion of composite solid rocket fuels, the presence of the monopropellant oxidizer decomposition flame was not applicable for axial-injection, end-burning hybrid rocket motors. As such, the BDP model was not used in favor of finding a more applicable model.

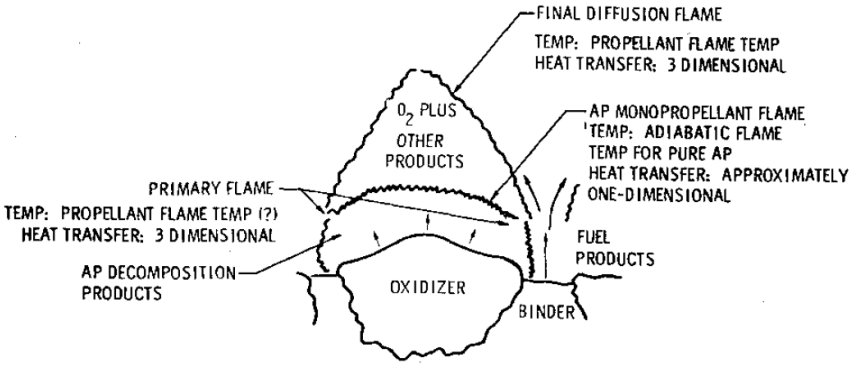

Figure 2.5. Beckstead-Derr-Price Model [51]

2.2.3 Granular Diffusion Flame

The GDF model was developed by Summerfield et al. [52-53] to describe the combustion of heterogeneous solid rocket fuels. Unlike the BDP, the GDF model does not include a monopropellant decomposition oxidizer flame in the model. Instead it uses a single flame whose location is a combination of the kinetic and diffusional effects. Summerfield et al.'s theory was that the kinetic and diffusional effects for the

heterogeneous solid rocket fuels occurred at the same time, and that the regression rate could be modeled using the equation

$$\frac{1}{\dot{r}} = \frac{a}{p_{ch}} + \frac{b}{p_{ch}^{1/3}} \tag{2.13}$$

where a and b are experimentally determined coefficients and p_{ch} is the chamber pressure. A derivation of the GDF model is included in Appendix E. To determine applicability, the GDF model was calibrated using experimental data. The a term describes the kinetic effects while the b term describes the diffusional effects. As can be seen in the equation, the regression rate is proportionally related to the kinetic effects with respect to the chamber pressure but only related to the diffusional effects to the 0.33 power. As the flame approaches a pure kinetically limited condition, the pressure exponent in St. Robert's Law approaches unity. Conversely, as the flame approaches a pure diffusion limited condition, the pressure exponent approaches 0.33. In addition, a physical model was determined to describe the a and b coefficients a priori [52-53]. A plot illustrating the transition from a pure kinetic condition to a pure diffusion condition is shown in Figure 2.6. As can be seen in the figure, the exponent for a pure kinetic condition (i.e. $b = 0$) is 1 while the exponent for a pure diffusion condition (i.e. $a = 0$) is 0.33. The other conditions shown illustrate the impact on the exponent due to contributions from both kinetic and diffusion processes.

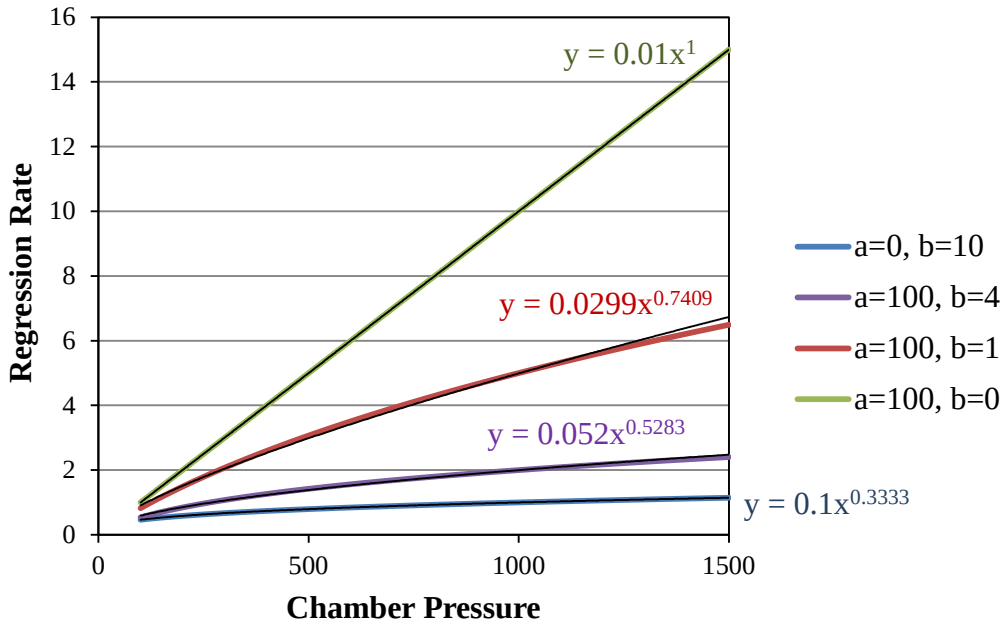

Figure 2.6. GDF Conditions

Since the pressure exponent of unity for the kinetically limited case is close to that observed in the literature for axial-injection, end-burning hybrid rocket motors, the GDF model was considered to be an appropriate model for describing the average or effective flame location of axial-injection, end-burning hybrid rocket motors. In addition, the absence of a monopropellant decomposition flame as given in the BDP model was a better match for the axial-injection, end-burning configuration.

Some difficulties arise through the use of the GDF model to describe the regression rate of an axial-injection, end-burning hybrid motor. These difficulties include the presence of a single, averaged oxidizer particle diameter term in the model and the assumption that all fuel regression is due to pyrolysis or sublimation without entrainment [54]. While these differences between the model basis and the experiments could result in difficulty in making a complete extension of the model to the experiments, it was

determined that the application would be sufficient to gain a basic understanding of the physical mechanisms involved. A fuller description of the kinetic and diffusional effects and their application to the axial-injection, end-burning hybrid configuration is given in the model results section of Chapter 4 and in the derivation in Appendix E.

CHAPTER 3

EXPERIMENTAL APPROACH

To evaluate the regression rate of the porous axial-injection, end burning hybrid fuel grains, test systems were developed for testing hybrid fuel grains in an axial-injection, end burning configuration in the Propulsion Research Center (PRC) Johnson Research Center (JRC). Flow rates and chamber conditions were determined using measurements by thermocouples and static pressure transducers. Chemiluminescence was used to determine the start of the burn time. Regression rates were calculated using the total regression length divided by the total burn time. To assess the effect of pore sizes on the regression rate, tests were conducted using high, middle, and low pore size articles. XCT scans were evaluated for assessing the solid fraction and pore size of representative grains.

3.1 Johnson Research Center

The JRC is one of the facilities of the PRC. A layout of the JRC is shown in Figure 3.1. As can be seen in the figure, the JRC is composed of several labs including a plasma combustion lab, laser diagnostics lab, vacuum chamber lab, water tunnel flow lab, and a spray facility. Additionally, an outdoor propulsion test facility composed of an air breathing test cell, a hot-fire rocket test cell, and a diagnostics bay is also located at the JRC. Testing in the hot-fire rocket test cell is conducted remotely from a control room in

the main building. Remote testing provides additional safety as test conductors are not allowed near the experiment during firings.

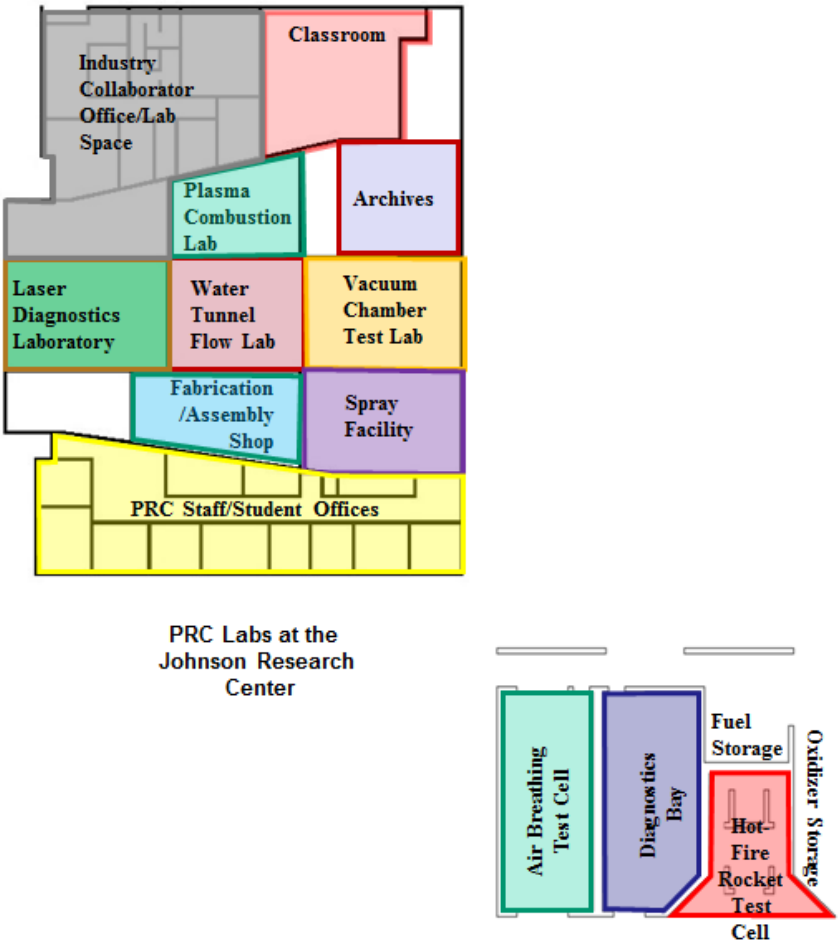

Figure 3.1. JRC Layout

The axial-injection, end-burning hybrid testing at the JRC occurred in the hot-fire rocket test cell in the propulsion test facility. A picture of the propulsion test facility is shown in Figure 3.2. Depending on the needs of the experiment, feed systems in the hot fire rocket test cell can provide gaseous oxygen (GOX), liquid oxygen, nitrous oxide (N_2O), gaseous nitrogen (GN_2), gaseous hydrogen (GH_2), gaseous methane, propane, or

kerosene. The GOX system in the propulsion test facility is designed to provide flow rates up to 0.91 kg/s (2 lbm/s) through a manifolded set of k-bottles [55]. Piping in the GOX system consists primarily of 19.05 mm (0.75 in.) outside diameter (OD) 316 stainless steel (SS) tubing with 2.1 mm (0.083 in.) wall thickness. Flowrates are controlled through the use of a critical orifice that is sized based on the specific experiment. The GOX system pressure is controlled through the use of a dome loaded pressure regulator set by the GN_2 system. A system purge is also provided by the GN_2 system to flush any oxidizer out of the test chamber after a firing is complete.

Figure 3.2. PRC Propulsion Test Facility

Similarly, the N_2O system consists primarily of 19.05 mm (0.75 in.) outside diameter (OD) 316 stainless steel (SS) tubing with 2.1 mm (0.083 in.) wall thickness. The N_2O system is designed to deliver either liquid or gaseous N_2O. For liquid N_2O, system pressure is provided by GN_2 pressurant controlled through a pressure regulator. For gaseous N_2O, the system pressure is set through a regulator at the N_2O k-bottle. As such, the maximum pressure for the liquid N_2O is limited by the pressure rating of the run

tank (12.4 MPa [1800 psi]) while the maximum pressure for the gaseous N_2O is limited by the vapor pressure of the N_2O. As with the GOX system, flowrates are controlled through the use of a critical orifice that is sized based on the specific experiment, and a system purge is also provided by the GN_2 system to flush any oxidizer out of the test chamber after a firing is complete.

Test chambers used in the hot-fire rocket test cell are mounted onto a thrust stand in the cell. A picture of the thrust stand in the hot-fire rocket test cell is shown in Figure 3.3. The test stand is capable of testing motors with thrust levels up to 2224 N (500 lbf). Chambers can be mounted either horizontally or vertically on the test stand as required by the needs of the experiment. The thrust stand is isolated from the propellant supply tanks by a bulkhead as a safety precaution.

Figure 3.3. Test Stand

3.2 Copper Combustion Chamber

The test chamber used in the experiment was the PRC's copper combustion chamber. A picture of the chamber is shown in Figure 3.4. The chamber uses a modular design to increase or decrease length as needed and is clamped together by threaded rods passed through flanges at the head and aft end of the chamber. Instrumentation ports are bored into the rings to provide access as needed for pressure or temperature measurements. One of the sections is designed to hold either acrylic or UV quartz windows to provide optical access into the chamber. Additionally, the modular design allows for changing nozzles to obtain target chamber pressures and injection velocities. The copper design of the chamber allows for heat sink thermal management where the heat transferred to the chamber is conducted away from the internal surface to maintain the chamber temperature at a satisfactory level. However, active water cooling of the nozzle is performed to prevent softening and erosion of the throat.

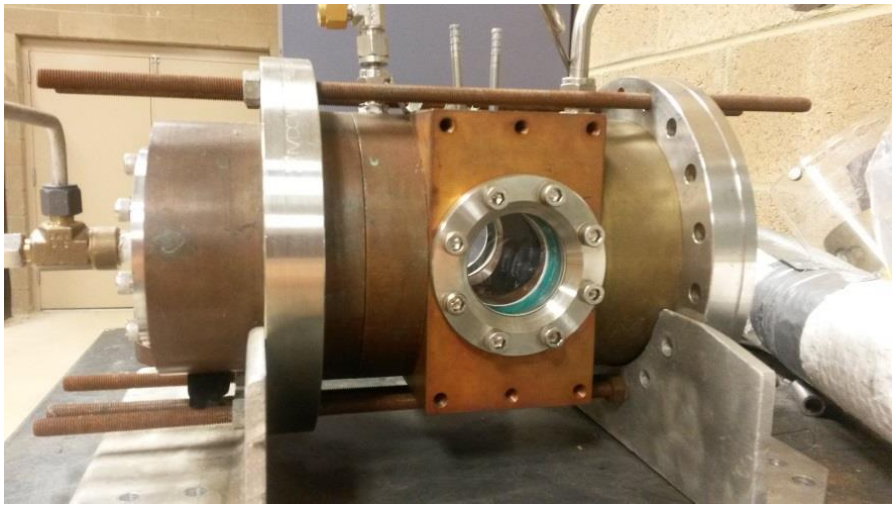

Figure 3.4. Copper Combustion Chamber

3.3 Test Articles

Porous rods with a nominal diameter of 19.1 mm (0.75 in.) and cut to a length of approximately 38.1 mm to 44.5 mm (1.5 to 1.75 in.) were selected as the fuel. Four different high density polyethylene rods of nominal 200 micron, 100 micron, 50 micron, and 15 micron average pore sizes were selected from Pore Technology, Inc. These pore size values were determined by the manufacturer through a bubble point flow rate test.

In preparation for testing, the test articles were bonded with epoxy to a nylon sleeve with a nominal 20.6 mm (0.81 in.) inner diameter and 22.6 mm (0.89 in.) outer diameter to restrict the oxidizer outflow to the upper face. Nylon was selected as the sleeve as it burned at approximately the same rate as the porous grain. J-B Weld was selected as the epoxy as its temperature rating was approximately equal to that of the test article. The diameter of the test article was based on balancing the requirements of larger diameters to reduce the ratio of the insulation area to the porous area and smaller diameters to reduce oxidizer system flow rate requirements. The test article length was selected as to place the burning face of the test article into the view area of the combustion chamber window. A picture showing one of the test articles affixed to a test plate prior to a test is given in Figure 3.5. An illustration showing a cross sectional view of the test article in the chamber is shown later in Figure 3.8.

Figure 3.5. Test Article Affixed to Test Plate

For the porous rods, the void fraction was found by dividing the volume of ethyl alcohol displaced by the rod when submerged by the total cylindrical volume of the rod including pores to find the solid fraction and then subtracting one by the solid fraction. This resulted in void fractions of 0.51, 0.50, 0.43, and 0.36 for the 200 micron, 100 micron, 50 micron, and 15 micron test articles respectively. Measurements for determining the solid fraction for the test articles are given in Appendix A.

X-ray computed tomography (XCT) scans were performed of the porous rods to verify the calculated void fractions. The porosity of the grains using the XCT scans are determined by imaging the grain, reconstructing slices of the grain, filtering the images, and then applying a threshold value to determine what portions of the grain are solid and which are void. A diagram illustrating the XCT process is shown in a scan of an assembled 50 micron test article resulted in a void of 0.46 showing concurrence with the calculated void fractions [56].

While the average void fraction values from the XCT scans showed agreement with the values from the submersion tests, the XCT results showed a large void in the middle of the grain and relatively void toward the edges which could potentially undermine the uniform porosity assumption for the modified ablative model. Based on

cursory visual observation of the grains, there was concern that the XCT results exhibited some bias. This bias was thought to arise from using a thresholding value to determine solid and void pixels particularly regarding the question as to how much of a given area had to be either solid or void for the XCT scan to detect it. To better evaluate the XCT scan, a closer inspection was conducted of one of the 50 micron grains after combustion. A picture of the grain is shown in Figure 3.7. Observing the grain after combustion was chosen since cutting the grains typically biased the surface but combustion was postulated to not have the same shearing effect as cutting. As can be seen in Figure 3.7, pores are scattered across the entire combustion surface. While some pores in the middle of some grains were larger than those on the edges, visual inspection indicated that there was indeed a distribution of pores as opposed to solely a central concentration as suggested by the XCT results.

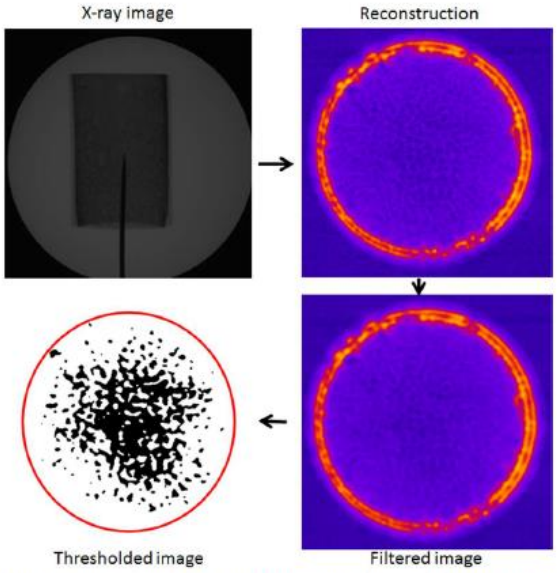

Figure 2: Raw x-ray image(top left) reconstructed slice (top right) reconstructed slice with removed outliers and 2-pixel radius median filter(bottom left) and thresholded slice (bottom right). The reconstructed and filtered slices have colormaps imposed for visual appeal. The red circle in the thresholded image was imposed to represent the outer wall ring that is present in the reconstruction and filtered images.

Figure 3.6. XCT Process [56]

Figure 3.7. 50 Micron Surface View

3.4 Experimental Setup

An illustration showing the placement of the test articles in the chamber is shown in Figure 3.8. As can be seen in the figure, the test article is located toward the head end of the chamber near the oxygen injection. The oxygen is injected into a plenum to mitigate preferential flow into the test article. The test article is epoxied to the test plate as shown in Figure 3.5. The window section has two holders for two windows and one instrumentation pass through.

For the experiment, acrylic windows were initially used; however, due to slight burning of the window across a number of tests, visibility through the window was inhibited. Due to this decline in visibility, the acrylic windows were replaced with UV quartz windows. In addition, a section with an instrumentation port was included in the test chamber setup to provide the ability to measure the temperature and pressure of the chamber. Finally, the nozzle section is located at the aft end of the chamber. As can be seen in the figure, the nozzle is a separate piece from the holder which allows it to be

changed between experiments to achieve the desired pressure for a given flow rate. Water cooling is provided to the nozzle to cool the throat to prevent erosion.

The assembled combustion chamber as mounted on the thrust stand is shown in Figure 3.9. Key components of the experiment hardware are labeled in the figure. The nozzle, window section, the test plate, and the instrumentation ports are designated. In addition, the figure shows the igniter mounted to the combustion chamber. Ignition of the test article is achieved using a GOX/GH_2 torch igniter. Also, as can be seen in the figure, a mirror is mounted next to the combustion chamber for optical access for the camera. The mirror setup was used to protect the camera should the UV quartz windows shatter or dislodge.

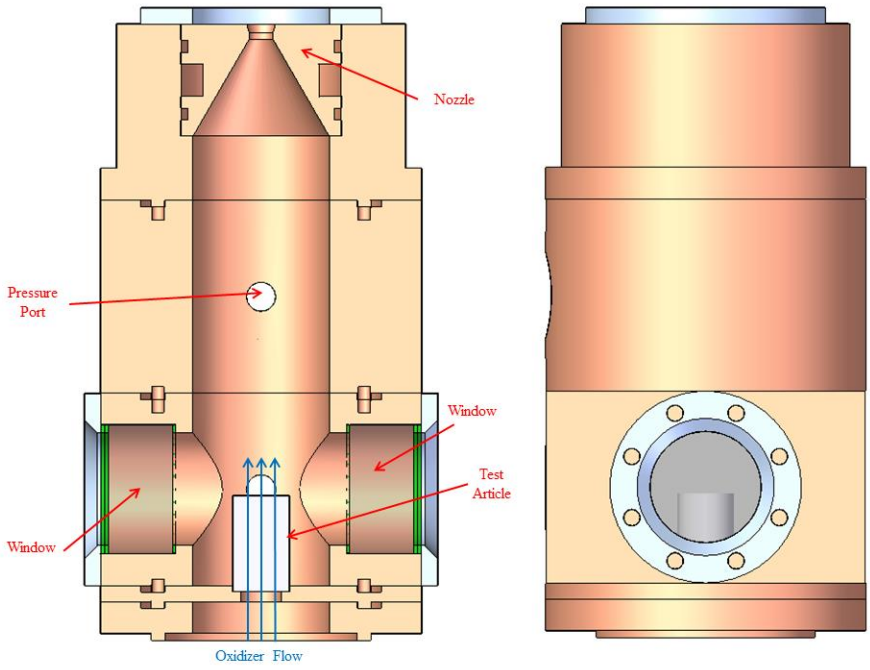

Figure 3.8. Test Chamber Setup

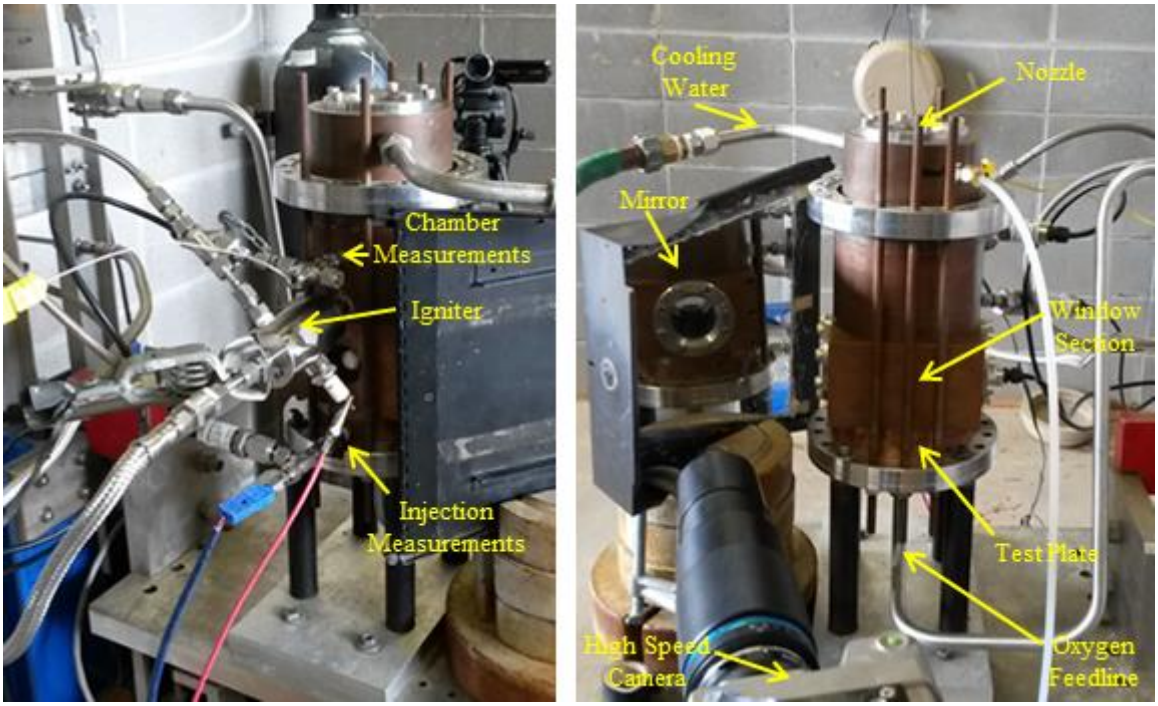

Figure 3.9. Assembled Experiment

3.4.1 JRC Facility Schematic

The schematic of the experimental setup using GOX as the primary oxidizer is shown in Figure 3.10. As can be seen in the figure, the setup uses a GOX igniter system, a GH_2 igniter system and a GN_2 system as well as the primary GOX system. The GOX system provides the oxygen to the test article for the test. Flow initiation and shutoff is remotely controlled through two pneumatically actuated valves (O6 and O9). The second valve (O9) is the fire valve and is the primary one for starting and stopping flow during a test, and the first valve (O6) is the main valve and is used as an emergency shutoff. Line pressures in the primary GOX system are set using a dome loaded pressure regulator (O7). The GOX flowrate was metered by an orifice upstream of the chamber (O10). Key pressure and temperature measurements in the setup were taken upstream of the orifice (P2 and T1), upstream of the test article (P3 and T2), and in the chamber (P4 and T3).

The GOX and GH_2 igniter systems provide the propellants for use in the igniter. The pressure in the GH_2 igniter system is established using a dome loaded pressure regulator (H8) while the pressure in the GOX igniter system is established using a regulator at the GOX igniter k-bottle (IO2). Flowrates for both igniter systems are metered using a flow control orifice. Ignition for the igniter propellants is accomplished using a lawn mower spark plug. Finally, the GN_2 system is used to set the primary GOX and igniter GH_2 line dome loaded pressure regulators and for purges in the three propellant systems. In addition to standard purge functions of clearing the feedlines, the purge in the primary GOX system is used to displace the oxygen in the test article to extinguish it at the conclusion of a test.

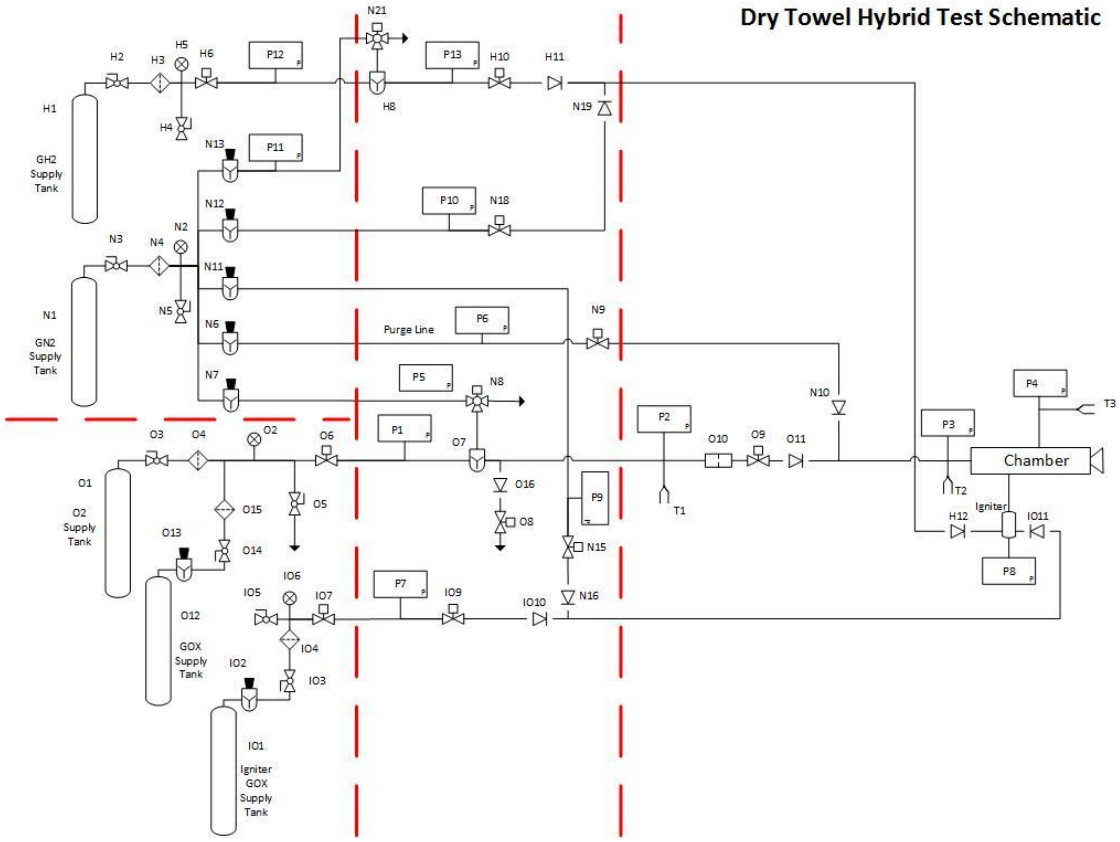

Figure 3.10. JRC GOX Facility Schematic

The schematic of the experimental setup using N_2O as the primary oxidizer is shown in Figure 3.11. This setup is very similar to the setup using GOX as the primary oxidizer in that it uses both igniter systems in the same configuration. The GN_2 system is the same except that the primary oxidizer pressure is not set by a dome loaded pressure regulator. Instead, the pressure in the N_2O system is set by a pressure regulator on the N_2O k-bottle (O2). As before, flow is controlled by two pneumatic valves, a main valve (O12) and a fire valve (O15), and flowrates are metered using a flow control orifice downstream of the fire valve (O17).

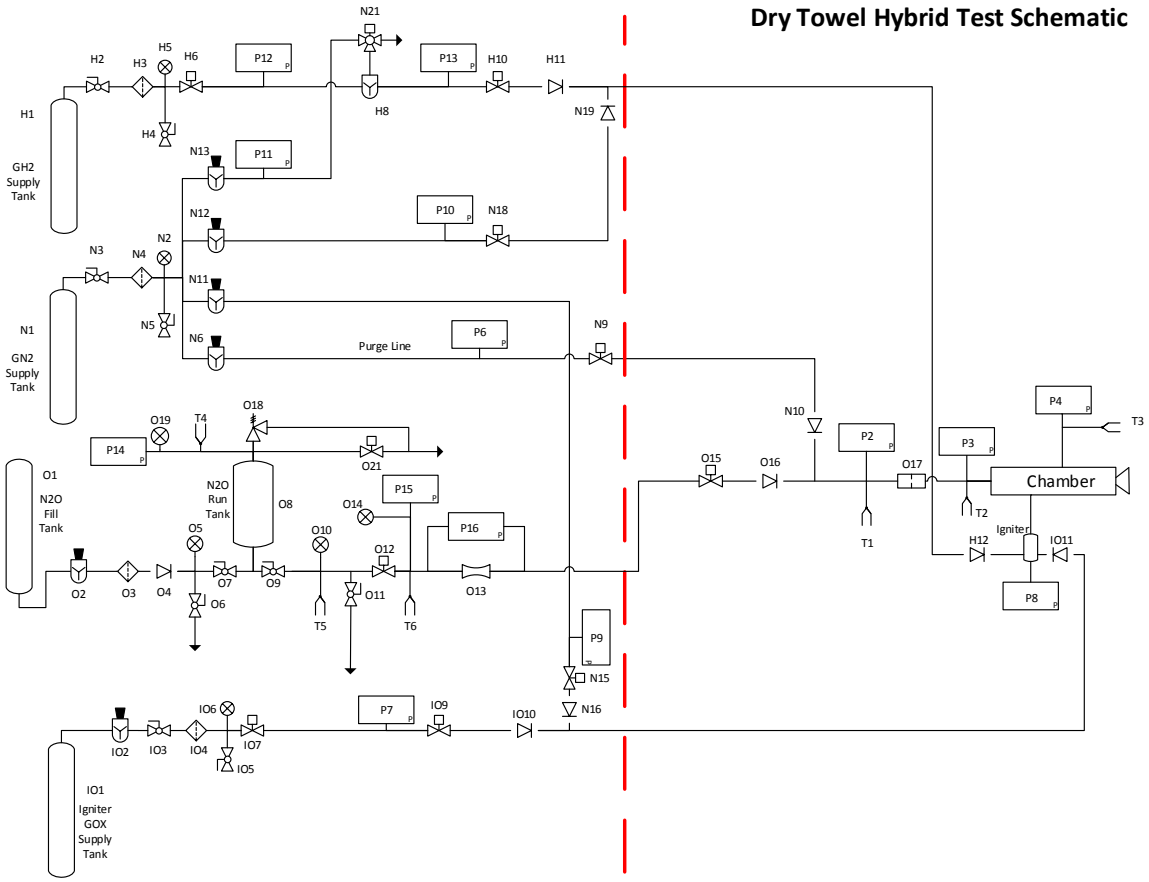

Figure 3.11. JRC N_2O Facility Schematic

3.4.2 PLC Logic

Remotely actuated valves were controlled using an Omron Programmable Logic Controller (PLC). Four zones were created in the PLC for the different modes of operation during a test. The first zone was the "Preliminary" zone which was used prior to initiation of the firing sequence. In this zone, all valves were under manual control. The second zone was the "Fire" zone which was the primary zone of the firing sequence. This zone was initiated by pressing the "Fire" button on the control board. The third zone was the "Purge" zone. It became active after the "Fire" zone timer was complete or if the "End" button was pressed on the control board which manually overrode the "Fire" zone timer. Finally, a fourth "Abort" zone was created to set all valves to a safe state should an emergency occur. A summary of the PLC logic for the N_2O tests is shown in Figure 3.12. In the figure, the names of the remotely controlled valves (plus the spark) are provided in the leftmost column, and the valve designation as shown in Figure 3.11 is in the column next to the name. The four zones are listed across the top row. Yellow circles indicate manual control of the valve, green circles indicate that the valve is open (or turned on for the spark plug), and red circles indicate that the valve is closed (or turned off for the spark plug). A split in the zone (e.g. a green circle and then a red circle) for a valve means that the valve changes state during the zone (e.g. valve is opened at the start of the zone and then is closed).

Name	Number	Preliminary	Fire	Purge	Abort
N2O Main	O12				
N2O Vent	O21				
N2O Fire	O15				
N2O Purge	N9				
GOX Main	IO7				
GOX Ig. Fire	IO9				
GOX Ig. Purge	N15				
Fuel Main	H6				
Fuel Ig. Dome	N21				
Fuel Ig. Fire	H10				
Fuel Ig. Purge	N18				
Spark	-				

Figure 3.12. N_2O PLC Logic

3.5 Instrumentation and Data Acquisition

The primary instrumentation for each setup is shown in the respective schematics in Figure 3.10 and Figure 3.11. The orifice and test article inlet temperatures were measured using Omega T-type thermocouple while the other temperature measurements were performed using Omega K-type thermocouples. Ungrounded thermocouples were used to prevent the occurrence of a ground loop. The thermocouples were not calibrated in-house. As such, the manufacturer specified uncertainty of the larger value of 1.0 K or 0.75% above 0 °C for the T-type thermocouples [57] or 2.2 K or 0.75% above 0 °C for the K-type thermocouples [58] were used.

Static pressure measurements were performed using a variety of pressure transducers. These transducers were calibrated in-house using a deadweight pressure tester, and a regression analysis was performed to obtain a linear curve fit for each transducer. Additionally, a curve fit uncertainty analysis was performed for the transducers to describe the uncertainty of each transducer using a second-order expression of the form

$$U = aV^2 + bV + c \tag{3.1}$$

where U is the uncertainty of the transducer in kPa, V is the output voltage of the transducer, and a, b, and c are constants. The orifice inlet pressure was measured using a Sensotec FPA transducer with a range of 0-10.3 MPa (0-1500 psia); the injector pressure was measured using an Omega PX309 transducer with a range of 0-3.4 MPa (0-500 psig); and the chamber pressure was measured using an Omega PX309 transducer with a range of 0-3.4 MPa (0-500 psig). Each transducer had an output of 0-5 VDC.

Temperature and pressure data were taken using a National Instruments PXI-1052 chassis. The DAQ has a capability of 333 ksamples per second and a 16 bit resolution. Temperature data was taken using a NI-SCXI 1102 thermocouple card with a 2 Hz low-pass filter and a built-in cold junction compensation. Static pressure was taken using a NI-SCXI 1102B card with a 200 Hz low-pass filter. Both the thermocouple and static pressure measurements were sampled at 200 Hz with 20 samples taken at a time. Data was recorded using LabVIEW and output into *.lvm text files. Unique file names based on the designation of each test article were assigned to each text file to allow for ease of identification during analysis.

3.6 Chemiluminescence

As stated before, the initiation of combustion was determined through an optical measurement using chemiluminescence. Chemiluminescence takes advantage of the release of light from excited molecules to estimate reaction locations. A sketch illustrating the process of chemiluminescence emissions is shown in Figure 3.13 [59]. As can be seen in the figure, in chemiluminescence emissions, energy is transmitted to a molecule through the combustion process to raise the molecule to a higher energy state.

This energy is dissipated from the molecule through heat and other processes until the molecule reaches the point where it drops to the ground state energy releasing a photon in the process. The wavelength of the emitted photon is determined by the difference in energy between the energy level where the photon was released and the ground state energy level. Since these emissions are driven by the energy states of the molecule, the wavelength of the emitted photons is fixed by the molecule [59].

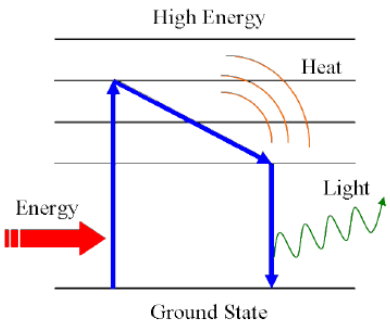

Figure 3.13. Chemiluminescence Emission [59]

For this experiment, CH* chemiluminescence was selected as it is a common radical in hydrocarbon combustion. The peak wavelength of photons released in CH* chemiluminescence is 431 nm [59]. Imaging of the test article was accomplished using a Vision Research Phantom Miro 4 high speed camera. Several different options were tried to obtain an image of the flame, but a two filter approach using an Andover 450FL07-50 filter and an Andover 420FG03-50 filter to obtain a CH* bandpass was ultimately chosen.

3.7 X-Ray System

XCT scans were performed at the UAH High Pressure Laboratory using x-ray radiography [56]. X-ray radiography functions by capturing the attenuation of x-ray

intensity caused by passing through the imaged object. A sketch illustrating the basic components required in x-ray radiography is shown in Figure 3.14 [60]. As can be seen in the figure, a source generates the x-rays. These rays are then transmitted through the object where the ray intensity is attenuated based on the object material and size. Finally, the rays are collected by a sensor where the results are captured as an image. The intensity of the captured image is based on the intensity of the x-rays detected by the sensor [60].

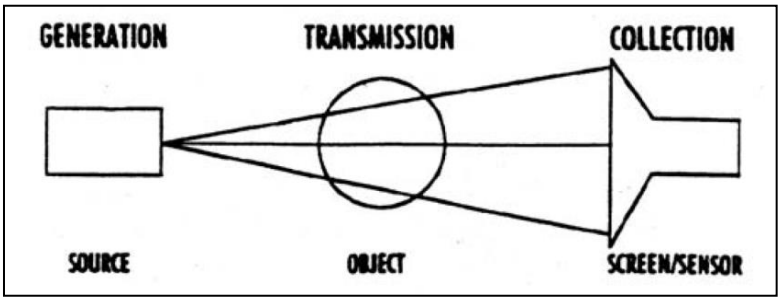

Figure 3.14. X-Ray Radiography [60]

The HPL uses an Eresco 200 MF4-R transmitter and a Toshiba E5877J-P1 X-ray image intensifier coupled with a Kappa HiRes3-XR camera. Pictures of the transmitter and intensifier with camera are shown in Figure 3.15. The transmitter is a 200 kV/600 W, air-cooled tube where the operating range varies from 10 kV to 200 kV. The tube emits a 40° x 60° elliptical beam. The image intensifier has a nominal entrance field size of 100 mm in N mode and 50 mm in M mode. The central resolution of the image intensifier is 77 Lp/cm for N mode and 110 Lp/cm for M mode. Finally, the camera has a light sensitive area of 5.632 mm x 5.632 mm and a 14 bit digital signal processor. Additionally, the camera has a frame rate of 30 frames per second.

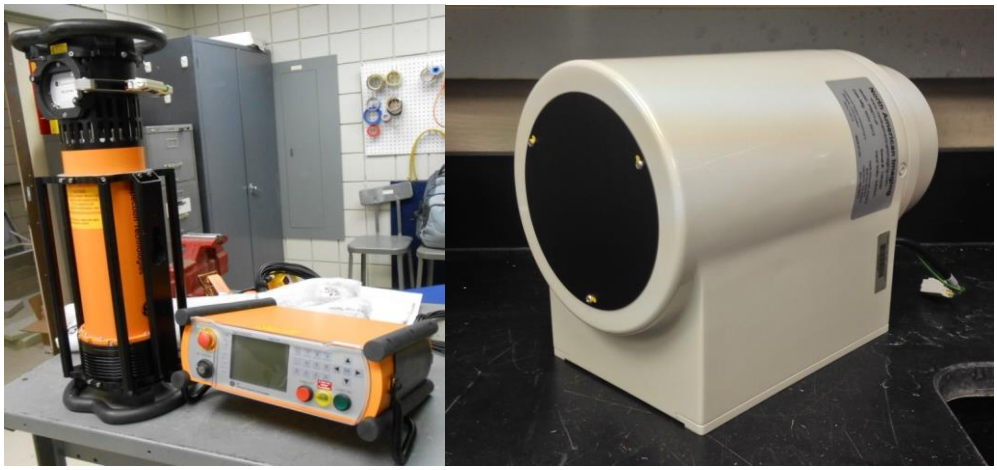

Figure 3.15. UAH X-Ray System (Left: Source, Right: Intensifier and Camera)

3.8 Data Analysis

Using the pressure, temperature, dimensional, and time measurements, the key parameters of the oxygen mass flow rate and the test article regression rate were able to be calculated. These parameters along with the test conditions and test article physical properties were able to be used in the ablative model derived in Chapter 2 to determine the flame coefficient.

First, the oxygen mass flux was calculated using the flow conditions at the orifice along with the geometry of the orifice and the test article. This was accomplished by dividing the expression for mass flowrate through a sonic orifice by the cross sectional area of the test article yielding the equation

$$\dot{m}''_{ox} = C_d \frac{p_{or}}{\sqrt{R_g T_{or}}} \frac{d_t^2}{d_p^2} \sqrt{\gamma_{ox} \left(\frac{2}{\gamma_{ox}+1}\right)^{\gamma_{ox}+1/\gamma_{ox}-1}} \tag{3.2}$$

where C_d is the discharge coefficient of the orifice, p_{or} is the upstream pressure at the orifice, T_{or} is the upstream temperature at the orifice, d_t is the orifice throat diameter, d_p is the test article diameter, and γ_{ox} is the ratio of specific heats for oxygen.

The average regression rate of the test article was calculated by dividing the change in height of the test article by the burn time. This method is given by the expression

$$\dot{r} = \frac{\Delta x}{\Delta t} \tag{3.3}$$

where Δx is the change in height of the test article, and Δt is the burn time. Since the test article is assumed to have a constant burn surface area with a regression rate expected to be based on the chamber pressure, it was expected that the average regression rate would be similar to the instantaneous regression rate. This expectation assumed that the pressure transients during the start and stop of the burn were minimal in length compared to the steady state portion of the test. A mass based method of calculating the average regression rate was investigated but was ultimately abandoned due to the difficulty of ascertaining the percentage of the cross section that was the porous fuel instead of epoxy or sleeve and the amount of sleeve consumed around the side. Since the tests were conducted in an oxidizing environment, some of the sleeve was consumed during a test.

3.9 Test Method

To develop the test matrix, the origin of the terms in the modified ablative model given in Eq. 2.9 was determined. By categorizing the various terms in Eq. 2.9 based on origin, the test variables were able to be determined. The categories used for the parameters were input parameters, material properties, flame properties, and the measured parameters. Equation 2.9 with the various parameters colored based on category is given by

$$\rho_f \dot{r} = \frac{c_{fl}(T_{fl} - T_{dec}) - \dot{m}''_{ox} c_{p,ox}(T_{dec} - T_o)}{\left(\Delta h_{f,dec} + c_{liq}(T_{dec} - T_{melt}) + \Delta h_{f,melt} + c_{sol}(T_{melt} - T_o)\right)} \tag{3.4}$$

where all terms have been previously defined. Parameters colored green are input parameters which are the independently set test conditions. The parameters colored red are material properties of the fuel and the oxidizer. The blue parameters are the flame properties which are in themselves driven by the input parameters and material properties. Finally, the parameters colored black are the measured parameters which are determined through direct measurements such as the regression rate or through calculation for the flame coefficient. A diagram showing the origin of the key parameters is given in Figure 3.16. As can be seen in the figure, the various parameters in Eq. 3.4 are divided by category using the same color scheme as used in Eq. 3.4.

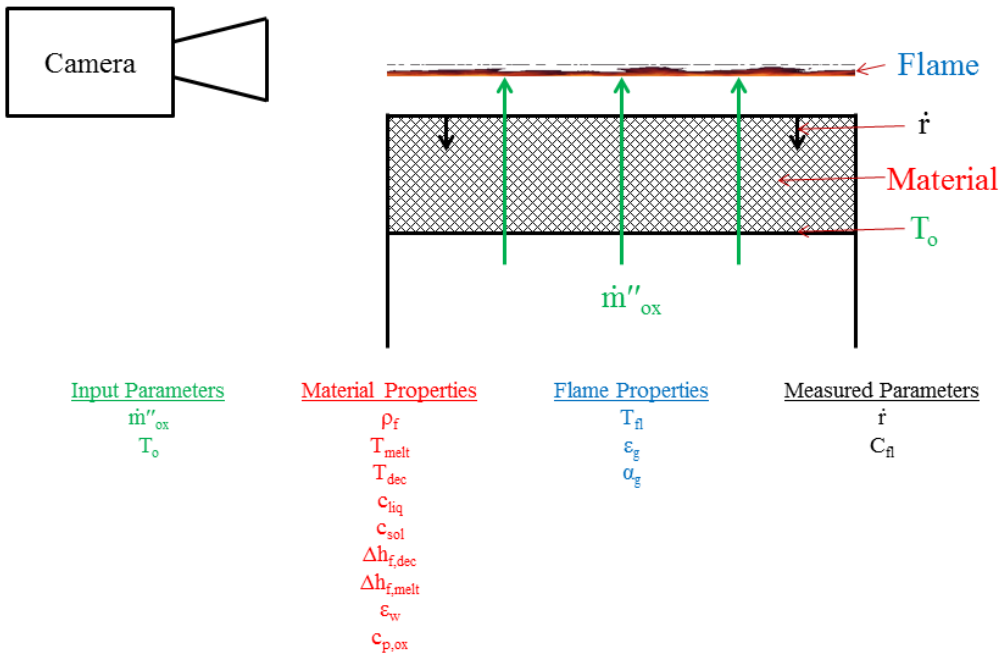

Figure 3.16. Experimental Setup

Using the results of the category analysis of the modified ablative model, it was determined that the key parameter to evaluate was the flame coefficient. As such,

variations in test conditions were selected to determine the key physical parameters that affect the flame coefficient so as to better compare the flame coefficient to flame models. While not shown in Eq. 3.4 or Figure 3.16, it was hypothesized that the primary dependency of the flame coefficient would be the chamber pressure based on the pressure dependency of the regression rate as observed by Nagata et al. [39-40]. This hypothesis was based upon the pressure dependence of the axial-injection, end-burning hybrid regression rate as observed by Nagata et al [39-40]. In addition, it was speculated that the pore size of the test articles could have an effect on the flame structure and thus the flame coefficient.

As such, the four variables identified for evaluation in this experiment are the oxidizer mass flux, chamber pressure, test article porosity, and oxidizer selection (i.e. GOX and N_2O). The oxidizer mass flux was selected due to its impact on the oxidizer heat absorption term, and the oxidizer selection was chosen due to its impact on the oxidizer material properties and the flame properties. By using these four parameters, variation would be achieved in each of the three controlled parameter groups (input, material, and flame) which in turn would aid with evaluating the applicability of the modified ablative model. The oxidizer mass flux was controlled by setting the pressure at the orifice or by changing the orifice throat area; the test article porosity was specified by the manufacturer; and the chamber pressure was controlled by adjusting the nozzle diameter based on given flowrates. A table showing the test matrix conditions is given in Table 3.1. For this experiment, a test series consisted of a target chamber pressure and oxidizer flow rate and could be conducted with a variety of test article porosities or oxidizers. The entire test matrix consisted of 11 independent test series.

Table 3.1. Target Test Matrix

Series	Chamber Pressure (kPa)	Oxidizer Mass Flow Rate (g/s)	Nominal Porosity (microns)	Oxidizer
1	101.3	8	100	GOX
2	101.3	10	200, 100, 50	GOX, N_2O
3	101.3	15	100	GOX, N_2O
4	170	30	100	GOX
5	275	30	100	GOX, N_2O
6	275	45	100	GOX
7	425	50	50, 15	GOX
8	515	50	200, 100, 50	GOX, N_2O
9	740	65	200, 100, 50	GOX, N_2O
10	740	110	100	GOX, N_2O
11	1190	105	100	GOX, N_2O

CHAPTER 4

RESULTS AND ANALYSIS

A total of forty-four successful experiments were conducted for evaluation and for developing the analytical model. Both GOX and N_2O were used as oxidizers in combination with the polyethylene fuel to evaluate the impact of varying the oxidizer on the performance of the axial-injection, end-burning configuration. In addition, test articles with different pore sizes were tested to determine the effect of porosity on the test articles.

4.1 GOX Experimental Results

Data were successfully taken for twenty-seven hot-fire tests using GOX as the oxidizer. The tests consisted of one 15 micron article test, five 50 micron article tests, seventeen 100 micron article tests, and four 200 micron article tests. A summary of the test results is shown in Table 4.1 with fuller details on test conditions given in Appendix B. The regression rate for each test was determined by measuring the length of each test article before and after each test to determine the grain regression and then dividing the regression by the burn time as given in Eq. 3.3. Since the test articles were end burners with a constant burn area and the regression rate was dependent on pressure, it was assumed that the average regression rate was a good approximation of the instantaneous regression rate. The burn time was determined by for all test articles by

using the visual observation of when the initial flame spread across the end surface as the start of burning and the disappearance of flame as the end of burning for atmospheric tests. The minimum time derivative of chamber pressure [61] for pressure tests was used to determine the end of burning for those cases. The presence of a flame on the end surface for the start of the burn time was selected as the pressure increase provided by the igniter was significant enough for the low pressure tests to bias the start time. For each case, the average pressure was found by integrating the pressure trace over the length of the burn using the trapezoidal method and then dividing by the burn time. An example pressure trace using Test Article 100-10 is given in Figure 4.1. The blue diamonds give the pressure chamber pressure as a function of time, and the vertical red lines indicate the start and stop of the burn time. As stated before, the average chamber pressure was determined by integrating the pressure trace over the region bounded by the vertical red lines.

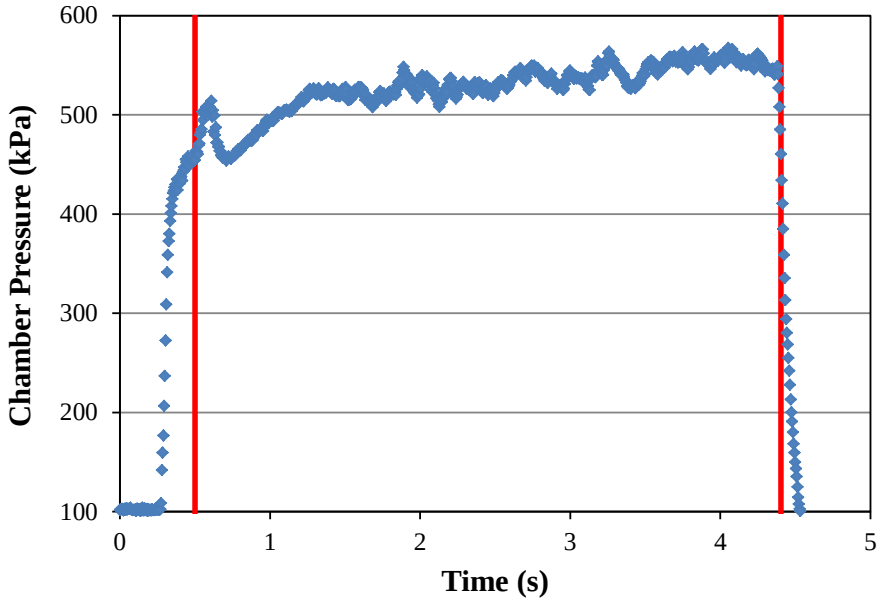

Figure 4.1. Article 100-10 Pressure Trace (GOX)

Table 4.1. GOX Experimental Results

Test Article	Chamber Pressure (kPa)	Chamber Pressure Unc. (%)	Oxidizer Velocity (m/s)	Oxidizer Velocity Unc. (%)	Regression Rate (mm/s)	Regression Rate Unc. (%)
15-1	409.6	2%	87.2	8%	1.48	76%
50-1	732.5	1%	52.7	8%	6.09	9%
50-2	504.0	2%	59.8	8%	3.18	14%
50-3	101.5	9%	61.8	12%	0.28	157%
50-4	528.2	2%	56.0	8%	3.32	12%
50-5	377.5	2%	56.6	8%	2.12	16%
100-1	101.4	9%	48.1	12%	0.60	7%
100-2	110.1	9%	44.3	11%	0.75	12%
100-3	100.8	9%	66.0	12%	0.48	90%
100-4	101.4	9%	39.4	12%	0.59	22%
100-5	100.6	9%	49.2	12%	0.67	16%
100-6	180.8	5%	80.2	9%	0.77	89%
100-7	285.1	3%	47.7	8%	1.79	20%
100-8	284.5	3%	77.4	8%	1.66	14%
100-9	275.2	3%	80.1	8%	1.24	19%
100-10	527.2	2%	49.6	7%	3.19	7%
100-11	527.9	2%	48.6	7%	3.59	7%
100-12	500.6	2%	47.3	7%	3.68	10%
100-13	716.4	1%	46.5	7%	4.76	16%
100-14	724.7	1%	78.2	7%	4.48	12%
100-15	1160.4	1%	45.8	7%	8.89	12%
100-16	532.3	2%	49.4	7%	3.67	11%
100-17	494.4	2%	50.6	7%	3.25	9%
200-1	132.7	7%	46.1	10%	0.79	22%
200-2	584.7	1%	46.1	7%	3.93	7%
200-3	443.6	2%	42.9	7%	3.06	5%
200-4	677.0	1%	43.8	7%	5.42	9%

Uncertainties for the experimental results were determined using a Monte Carlo Analysis [62] as given in Appendix C. As can be seen, the uncertainty of the chamber

pressure is below 9% for each test, and the oxygen velocity uncertainty is around 10% for each test. The regression rate uncertainty experienced a wide range of uncertainty across the various tests but typically fell below a value of 20%. The variation in regression rate uncertainty was typically caused by uneven burning at the lower chamber pressures which increased the uncertainty of the posttest article length. As can be seen, this effect decreased as increasing chamber pressure resulted in more even burn surfaces. The analyses were simplified due to one elemental uncertainty's (whether systematic or random) being the dominant influence for each input parameter. Further details on the uncertainty analysis are given in Appendix C.

Of note is that about an order of magnitude increase in pressure while maintaining the oxygen velocity (100-2 to 100-15) resulted in about an order of magnitude increase in the regression rate while an increase in velocity (100-7 to 100-8) did not have a significant impact on the regression rate. These results match the results found by Nagata et al. that the regression rate of an axial-injection, end-burning hybrid is a function of the chamber pressure as opposed to the oxidizer flux typical in conventional hybrids.

The disparity in the number of tests of the various test articles is that several of the 50 micron articles were used for initial tests to understand how to configure the experiment and did not result in any useful data and tended to fail at higher pressures, the 15 micron articles were difficult to ignite and were prone to break from the test plate during testing, and the 200 micron articles were evaluated only to determine potential effects of pore size on the regression rate. The failure of the 15 micron articles was suspected to be caused by the small pores' presenting a significant enough flow restriction to cause an adiabatic compression ignition at the test article inlet. A picture

showing a 15 micron test article with evidence of burning on the injection end are given in Figure 4.2.

Figure 4.2. 15 Micron Test Article Showing Ignition of Head End of Test Article (Left: Head End. Right: Aft End)

As such, the tests primarily focused on the 100 micron test articles as they were the most available after settling on the experimental configuration and were also the most tractable. For illustration, pretest and posttest pictures of Test Article 100-14 are given in Figure 4.3. As can be seen in the figure the test article regressed axially over the burn. Some burning of the outer sleeve did occur during the test but was not sufficient to compromise the test by allowing for oxidizer flow through the side of the grain. The burning of the sleeve provided the impetus to rely on the length measurements to determine the test article regression as opposed to mass measurements since a mass measurement would require a determination of the side burning present. It was also noted for the GOX tests that at higher chamber pressures, the test articles tended to regress more evenly over the burn surface while at lower chamber pressures, the test

articles tended to experience more regression at the edges. Additional pretest and posttest pictures are shown in Appendix D.

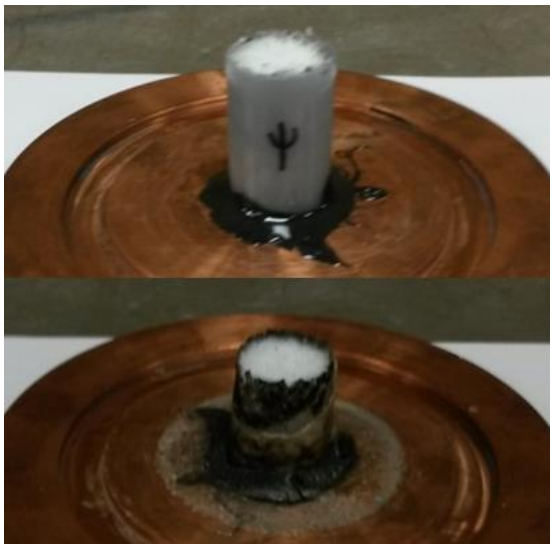

Figure 4.3. Test Article 100-14 (Top: Pretest, Bottom: Posttest)

As can be seen in Table 4.1, several of the tests were repeats of test matrix conditions. This was done to ensure repeatability in the tests. While there was some variability in the results at each pressure (possibly due to variations in the initial temperature), the regression rates tended to occur in groups based on the chamber pressure. The velocities observed during testing fall within the boundaries observed by Nagata et al. for stable end-burning where the flame does not lift-off the surface and is not absorbed back into the grain. Visual observation of the tests support the conclusion that the flame was not absorbed into the grain.

A plot of the regression rate for each of the twenty-two tests is given in Figure 4.4. As can be seen in the figure, the regression rate is a function of the chamber pressure. The power trendline shown in the figure is based on the data for the 100 micron

test article results, but it is representative of most of the other test articles as well except for the 15 micron test article case. The cause for the exceptionally low regression rate of the 15 micron test article is unknown at this time. One final point of interest is that the exponent of the regression rate is approximately equal to one which indicates the potential for amplification of pressure disturbances [1].

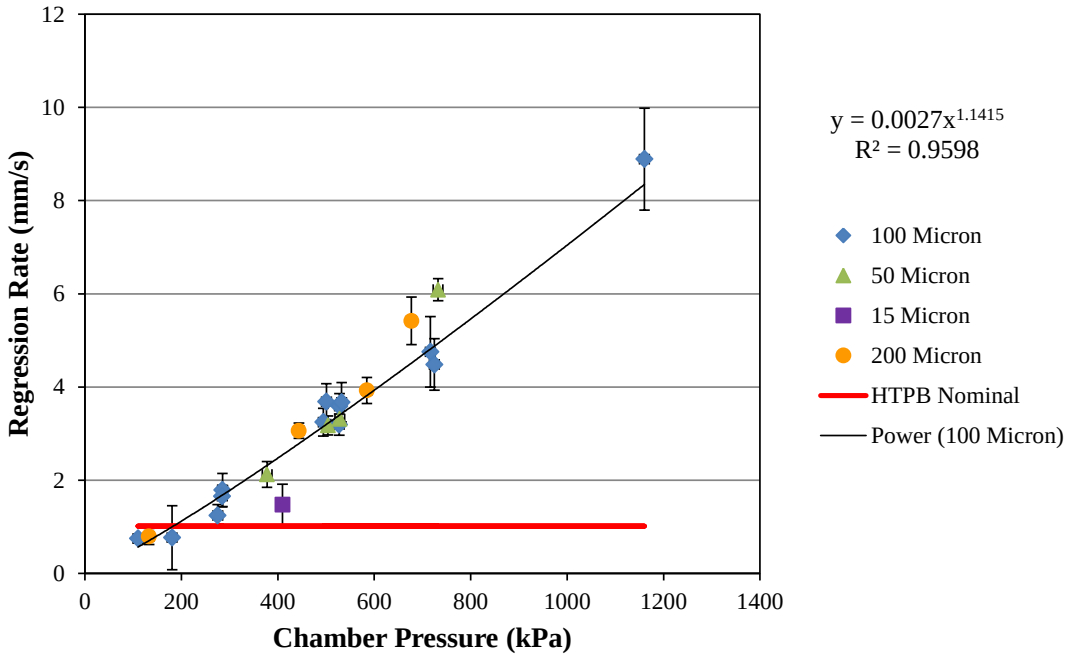

Figure 4.4. GOX Tests Regression Rates

Finally, since a porous axial-injection, end-burning hybrid has a low effective density (i.e. cross-sectional density accounting for the pores for oxidizer flow), a check was made to ensure that the configuration resulted in an increase in the fuel mass flux in addition to an increase in the regression rate. For this check, the regression rate of each test article was multiplied by the effective density of the porous material to calculate the fuel mass flux. Then, the results were plotted against the chamber pressure. A nominal

value for the fuel mass flux of an HTPB grain with a 1 mm/s regression rate (which is a reasonable value based on the regression rates presented in Sutton [1]) was also included for comparison.

The plot of the fuel mass flux for each test article is shown in Figure 4.5. As with the regression rate results, the fuel mass flux results follow a power trendline with an exponent approximately equal to one. The power trendline was based on the 100 micron test article results but is representative of most of the other tests as well. In addition, the fuel mass flux of the porous axial-injection, end-burning hybrid starts to equal the HTPB nominal around an operating pressure of 350 kPa and is clearly above the nominal case by 525 kPa. The increase of the fuel mass flux compared to the HTPB nominal indicates that the axial-injection, end-burning hybrid has the potential for mitigating the low fuel mass flux disadvantage of conventional hybrid rocket motors.

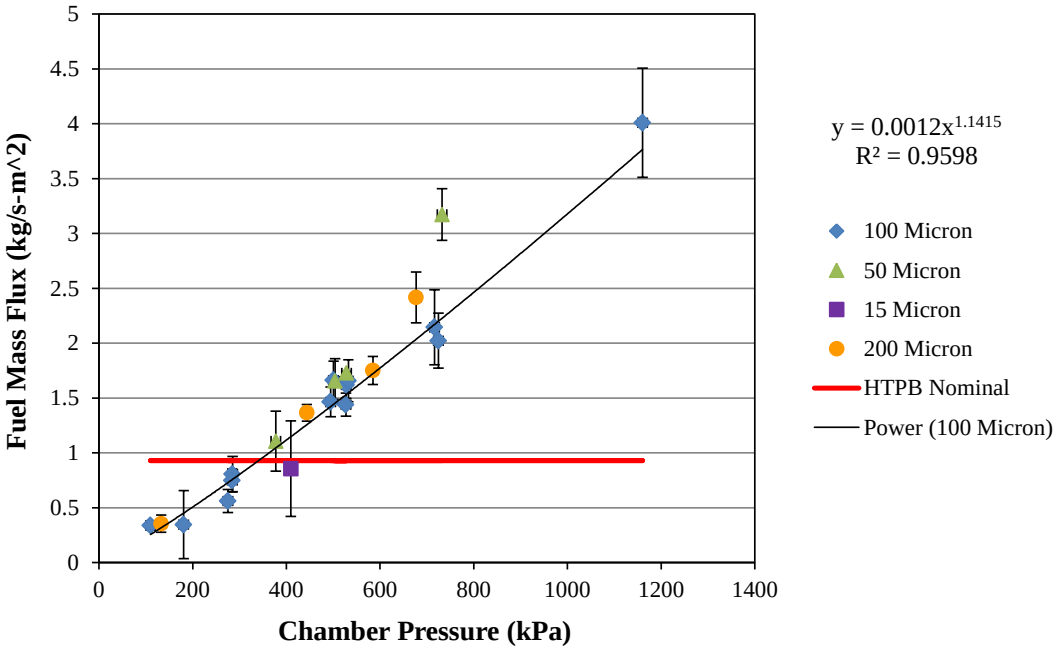

Figure 4.5. GOX Tests Fuel Mass Flux

4.2 GOX Model Results

Enthalpies for the oxygen were determined using NIST Fluid Properties [63], and the flame temperatures were determined using Propep3 [64]. Propep3 was selected as it allowed for an easy determination of the flame temperature based on the initial propellant temperatures and the chamber pressure. Basing the flame temperature on the chamber pressure was due to the assumption that the flame occurs as a diffusion flame at an equivalence ratio of one. The chamber pressure serves as a significant parameter as it determines the equilibrium constants controlling dissociation of the combustion products thus determining the flame temperature. Values for the other parameters were constant across the tests and are given in Table 4.2.

Table 4.2. Ablative Model Values

Parameter	Value	Units	Source
ρ_f (200 micron)	446	kg/m^3	Calculated
ρ_f (100 micron)	451	kg/m^3	Calculated
ρ_f (50 micron)	521	kg/m^3	Calculatec
ρ_f (15 micron)	580	kg/m^3	Calculated
T_{dec}	751	K	[15]
Δh_{tot}	2510	J/g	[15]
c_{sol}	1.6	J/g-K	[15]

Using Eq. 2.11, the flame coefficient for each test condition was determined. These flame coefficients are shown plotted against the chamber pressure in Figure 4.6. A power trendline for the flame coefficient as a function of pressure was determined based on the 100 micron test articles. Though there is some scatter, the power trendline

matches all test article porosities relatively well. As can be seen in the figure and in the power trendline equation, the flame coefficient is a function of the chamber pressure. Observing this relationship sparked interest in determining what caused the pressure dependency of the flame coefficient.

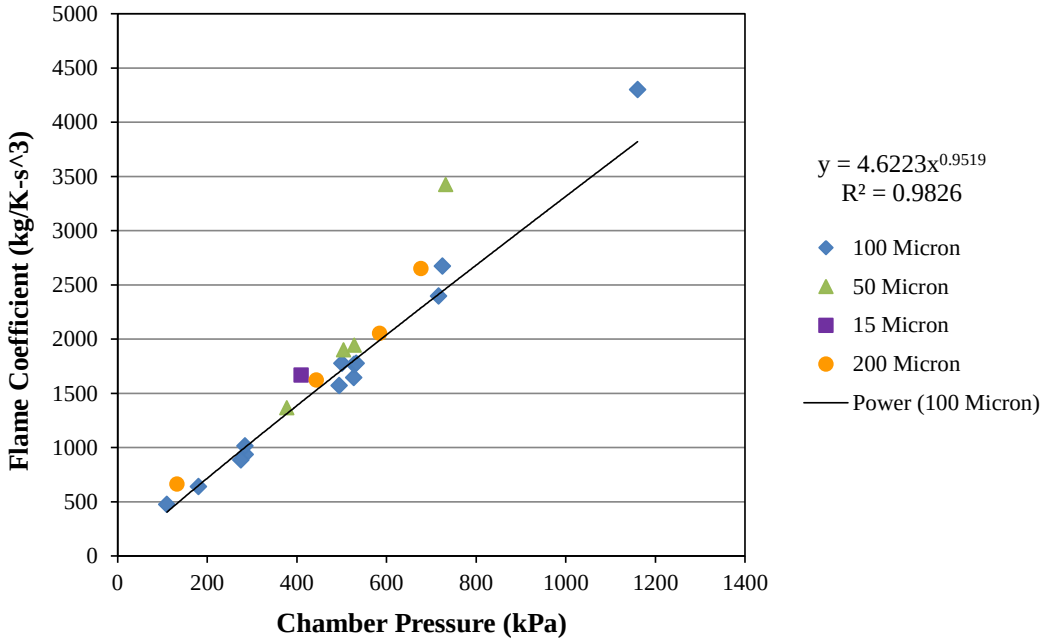

Figure 4.6. GOX Flame Coefficient vs. Chamber Pressure

To further determine the source of the pressure dependency of the regression rate, the terms in Eq. 2.10 were divided into a heat flux regression term and an oxidizer flow rate (advective term). This grouping is yields the relationship

$$\dot{r} = \frac{C_{fl}(T_{fl}-T_{dec})}{\rho_f(\Delta h_{tot}+c_{sol}(298K-T_o))} - \frac{\dot{m}''_{ox}(h_{ox,s}-h_{ox,o})}{\rho_f(\Delta h_{tot}+c_{sol}(298K-T_o))} \quad (4.1)$$

where the first term on the right hand side is the regression rate contribution from the heat flux to the grain and the second term on the right hand side is the regression rate decrease

from the porous oxidizer flow. Using the heat flux and advective terms shown in Eq. 4.1 with the flame coefficients shown in Figure 4.6, the regression rate contribution of both terms was determined. The magnitudes of these contributions are plotted against chamber pressure in Figure 4.7 for all test article porosities. As can be seen in the figure, the heat flux term has a strong dependence on chamber pressure (i.e. coefficient of determination of 0.97) while the advective term had a very weak dependence on chamber pressure (i.e. coefficient of determination of 0.25). These results confirm the heat flux term as the primary source of the pressure dependency of the regression rate.

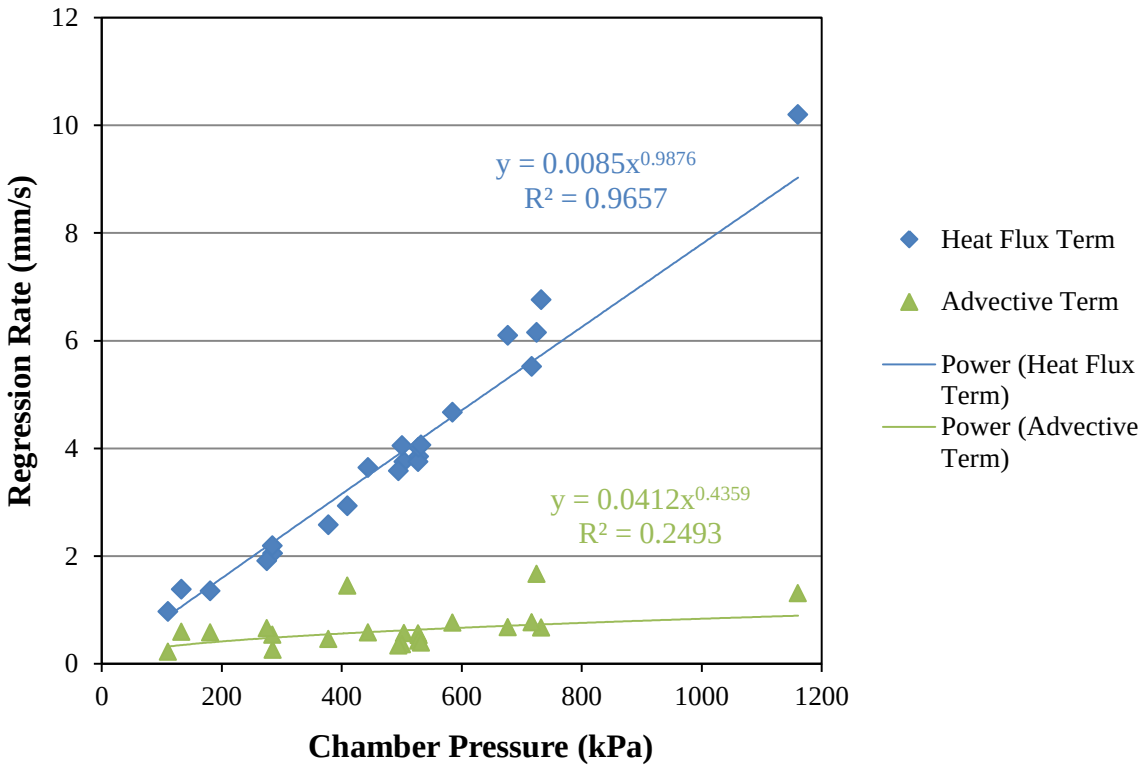

Figure 4.7. GOX Regression Rate Contributions

In an endeavor to understand the pressure dependency of the heat flux and thus the flame coefficient, the heat transfer from the flame to fuel surface was modeled using conduction as the primary means of heat transfer similar to the model used for solid rocket motors [52]. In this model, the flame coefficient was defined as being the average thermal conductivity of the vaporized gases divided by the distance from the flame to the surface (flame distance). This can be rearranged to solve for the flame height giving the equation

$$D = \frac{k}{C_{fl}} \tag{4.2}$$

where D is the flame distance and k is the thermal conductivity of the gases. Using Cequel [65] and Gaseq [66], a correlation for the thermal conductivity of the combustion gases between the grain and the flame can be determined by averaging the thermal conductivity of the cold gases at the combustion surface and the hot combustion gases at the flame. This correlation is given by the equation

$$k = 2.43 p_{ch}^{-0.121} \tag{4.3}$$

where k is in W/m-K and p_{ch} is in kPa. By inserting the curve fit for the flame coefficient given in Figure 4.6 and the curve fit for the thermal conductivity shown in Eq. 4.3 into Eq. 4.2, a relationship for the predicted flame height using the flame coefficient can be determined. This relationship is given as

$$D = 1.9 p_{ch}^{-1.07} \tag{4.4}$$

where D is in meters, and p_{ch} is in kPa. As can be seen in Eq. 4.4, the predicted flame distance is inversely proportional to chamber pressure. The pressure dependence of the flame location is a reasonable result as the pressure affects the concentration which in turn drives the chemical kinetics reaction rate (i.e. higher concentrations lead to an

increased number of collisions which increases the chemical kinetics reaction rate). As such, the pressure dependency of the flame location aids with explaining the pressure dependency of the axial-injection, end-burning hybrid as the decrease in the flame distance with increasing pressure would increase the heat transfer to the fuel thus explaining the increase in the regression rate.

Inspired by the inverse pressure dependence of the predicted flame distance vs. chamber pressure, it was desired to find a more detailed flame model to explain the predicted relationship. After investigating the literature, it was noticed that the Granular Diffusion Flame (GDF) model [52-53] predicts such an inverse relationship for the flame distance for a pure kinetically controlled flame (i.e. the diffusion contribution to the flame distance is negligible compared to the kinetic contribution to the flame distance). For the GDF model, the flame exists at a location based on a combination of the distance required for the propellants to diffuse and the chemical kinetics to occur. The distance for the kinetic portion of the GDF flame model is given by the equation

$$L_k = \frac{1}{\frac{\left[c_{liq}(T_s - T_e) - Q_s\right]^{0.5}}{\left[k\left(T_{fl} - T_s\right)\right]^{0.5}}} \frac{R_g T_g}{\left(Ae^{\frac{-E_a}{R_g T_g}}\right)^{0.5}} \frac{1}{p_{ch}} \tag{4.5}$$

where L_k is the GDF kinetic flame distance, T_g is the average temperature of the flame and surface, Q_s is the heat required for gasification of the fuel, E_a is the activation energy, A is the pre-exponential factor, and p_{ch} is the chamber pressure. As with the ablative model, the flame temperature is estimated for each condition using the stoichiometric assumption given in Chapter 2 with Propep3 [64]. Values for the parameters shown in Eq. 4.5 and later in Eq. 4.6 are given in Table 4. As a note, the values for the pre-exponential factor and the activation energy shown in Table 4.3 were estimated from

Turns [47] based on the values for C_2H_4 combustion. In addition, those values were divided by the molecular weight of ethylene to convert them to a per mass basis to use in Eq. 4.5.

Using Eq. 4.5, the GDF kinetic flame distance was calculated for each test condition. For this calculation, the latent heat required for decomposition was used for Q_s. The results of the GDF flame distance vs. chamber pressure for each test article are plotted in Figure 4.8. As can be seen in the figure, the GDF kinetic flame distance follows a similar trend to the predicted flame distance shown in Eq. 4.4. Some variations occur in the GDF kinetic flame distance due to using experimental data which have variations in initial temperature. However, even with the variations in test conditions, an inverse pressure relationship for the GDF kinetic flame distance is observed.

Table 4.3. GDF Model Values

Parameter	Value	Units	Source
c_{liq}	3	J/g-K	[46]
T_l	400	K	[46]
Q_s	-670	J/g	[46]
k	1.04	W/m-K	[65, 66]
A	$2 \cdot 10^{12}$	cm^3/mol-s	[47]
E_a	125500	J/mol	[47]
k_1	0.0015	m^2-Pa/s-$K^{1.5}$	Calculated

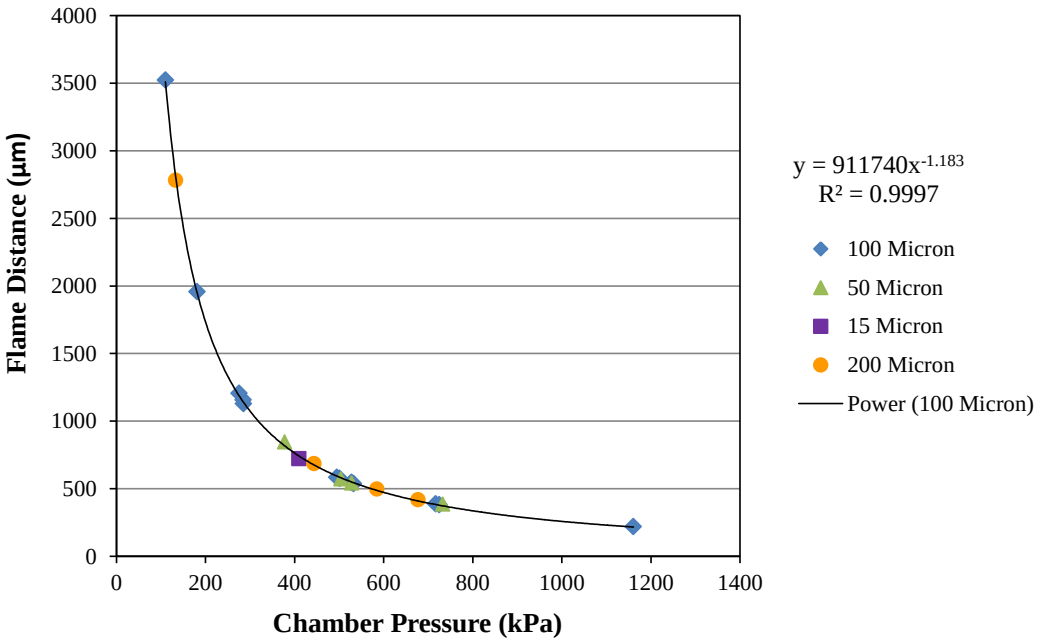

Figure 4.8. GOX GDF Kinetic Flame Distance vs. Chamber Pressure

Due to observed discrepancies in the predicted regression rate using the GDF kinetic flame distance, particularly at the higher chamber pressures, it was speculated that as the GDF kinetic flame distance decreased at higher pressures that the GDF diffusion flame distance became no longer negligible in comparison. As such, it was determined to estimate the GDF diffusion flame distance to see if a more accurate regression rate prediction could be achieved. This estimation was based on the GDF diffusion flame distance equation which is given by

$$L_D = \frac{1}{\frac{\left[c_{liq}(T_s - T_e) - Q_s\right]^{0.5}}{\left[k\left(T_{fl} - T_s\right)\right]^{0.5}}} \frac{k_2^{1/3} R_g^{5/6} T_g^{1/12}}{k_1^{0.5}} \frac{d_o}{p_{ch}^{1/3}} \tag{4.6}$$

where L_D is the GDF diffusion flame distance, k_1 is the diffusion parameter, k_2 is the pocket density, and d_o is the oxidizer diameter. The pocket density represents the mass of

fuel vapor generated by a fuel particle of a given diameter [52]. This equation was designed for evaluating the diffusion when the fuel and oxidizer were both solids as opposed to a hybrid configuration where the oxidizer is in the gas phase. As such, there is not a true equivalent for the oxidizer diameter term. This is further complicated by the lack of a single pore size. As such, an oxidizer diameter value was estimated by minimizing the sum of the square residuals between the experimental results and the GDF model including diffusion. This gave an oxidizer diameter value of 13.1 μm for the 100 micron test articles.

To obtain the total GDF predicted flame distance, the distances due to diffusion and chemical kinetics were summed as shown by

$$L_{tot} = L_k + L_D \tag{4.7}$$

where L_{tot} is the total GDF flame distance. To evaluate the prediction given by the GDF model for the flame distance, the predicted flame distance using the flame coefficient was divided by the GDF flame distance to check for similarity. These ratios are shown in Figure 4.9. As can be seen in the figure, the GDF flame distance has significant divergence from the predicted flame distance at the higher pressures when only the kinetic contribution is considered but is in closer agreement with the predicted flame distance when the diffusion contribution is considered as well. This meets the expectation that as the chamber pressure increases, the kinetic flame distance decreases until the point is reached that the diffusion flame distance is no longer negligible.

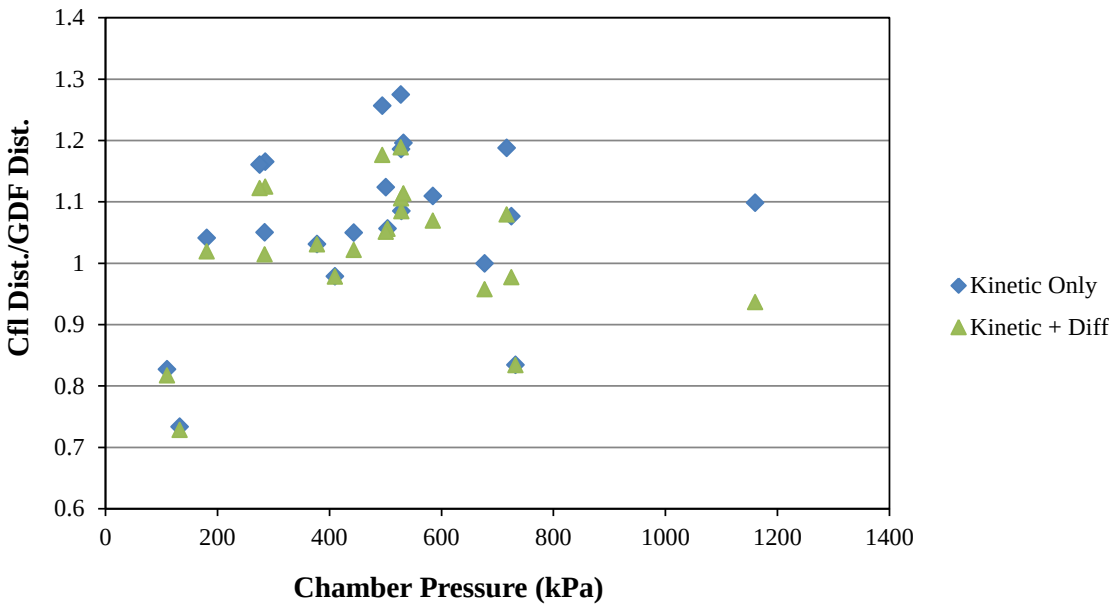

Figure 4.9. GOX Flame Distance Ratios

As a final comparison, regression rates were calculated based on the ablative model in Eq. 2.10 using both the GDF kinetic flame distance and the total GDF flame distance for evaluating the conductive heat transfer. Results for the 100 micron test articles are plotted in Figure 4.10 along with the measured experimental regression rate. Power trendlines for the measured and both predicted regression rates were determined, and the equations for each power trendline are given in the color of each power trendline. As can be seen in the figure, the predicted regression rates using the total GDF flame distance show much greater agreement with the experimental data at higher pressures than do the ones based on the GDF kinetic flame distance only. However, the power trendline for the total GDF flame distance regression rates does have a significant deviation from the experimental based power trendline at the highest pressure condition. This deviation was thought to have occurred due to the presence of several repeat test

conditions at the middle pressure range. Also of note is the above unity value of the pressure exponent. As noted in Section 2.2.3, the highest pressure exponent predicted in the GDF model is for the pure kinetic case which yields a unity value for the pressure exponent. However, the experimental data and the accompanying model predictions include variations in initial temperature and oxidizer mass flow rate. These effects are not included in the pressure-based trendlines. As such, above unity pressure exponents observed in the trendlines is considerd to result from the variations in initial temperature and oxidizer mass flow rate.

Due to the presence of so many test points, any bias in those conditions with respect to the power trendline would have a greater impact than that of a single test condition. As such, an additional plot was made and power trendlines determined where each cluster of test conditions and results were averaged into a single data point so that any one test condition would not significantly bias the power trendline. The averaged condition plot is given in Figure 4.11. As can be seen in the figure, the power trendlines have much greater agreement with the higher pressure condition. In addition, the power trendline based on the total GDF flame distance results is in closer agreement with the experimental power trendline and lies within the uncertainty band of each of the experimental test conditions. This agreement indicates that using a GDF based flame model has potential for explaining the heat transfer occurring in a porous axial-injection, end-burning hybrid rocket motor.

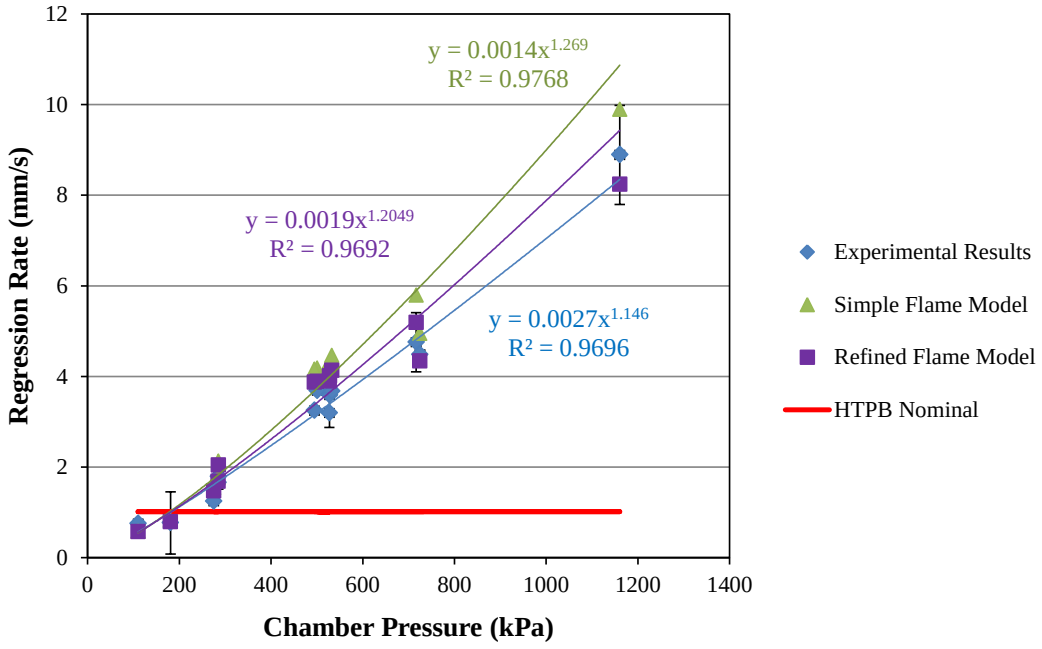

Figure 4.10. GOX 100 Micron Model Results

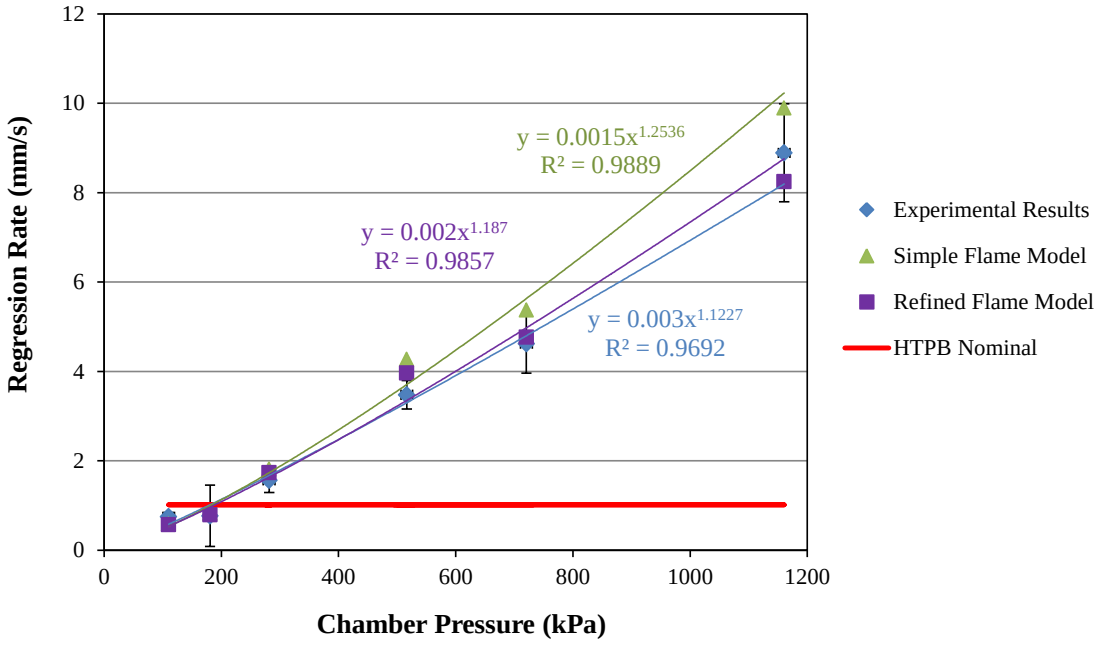

Figure 4.11. GOX 100 Micron Model Results (Averaged Conditions)

In addition, the model results for the 200 micron test articles are given in Figure 4.12, and the model results for the 50 and 15 micron test articles are given in Figure 4.13. As can be seen in Figure 4.12, the GDF results for both the simple flame model and the refined flame model show good agreement with the experimental results for the 200 micron test articles in the mid to upper pressure range tested. However, since only four test articles were evaluated, additional articles would need to be tested to determine more conclusive results. Additionally, as can be seen in Figure 4.13, the simple flame model shows sufficient agreement with the 50 and 15 micron test articles at the low to mid pressure range tested. The cause for the significant deviation of the highest pressure 50 micron condition from the predicted model value is currently unknown. In addition, a trendline was not determined for the 15 micron test articles due to the limited data.

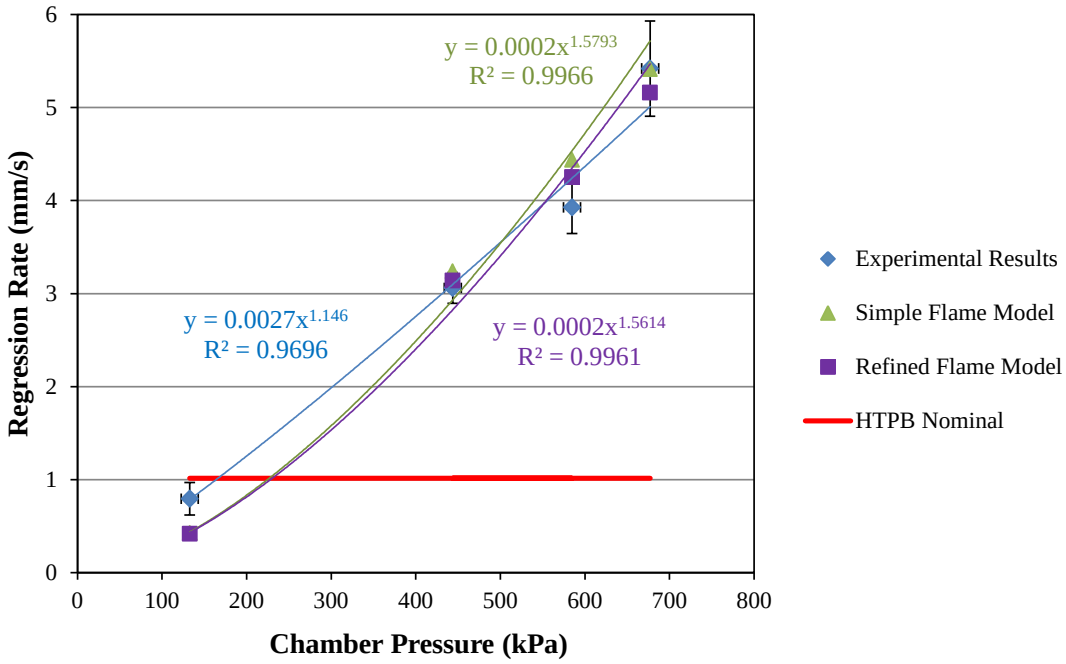

Figure 4.12. GOX 200 Micron Model Results

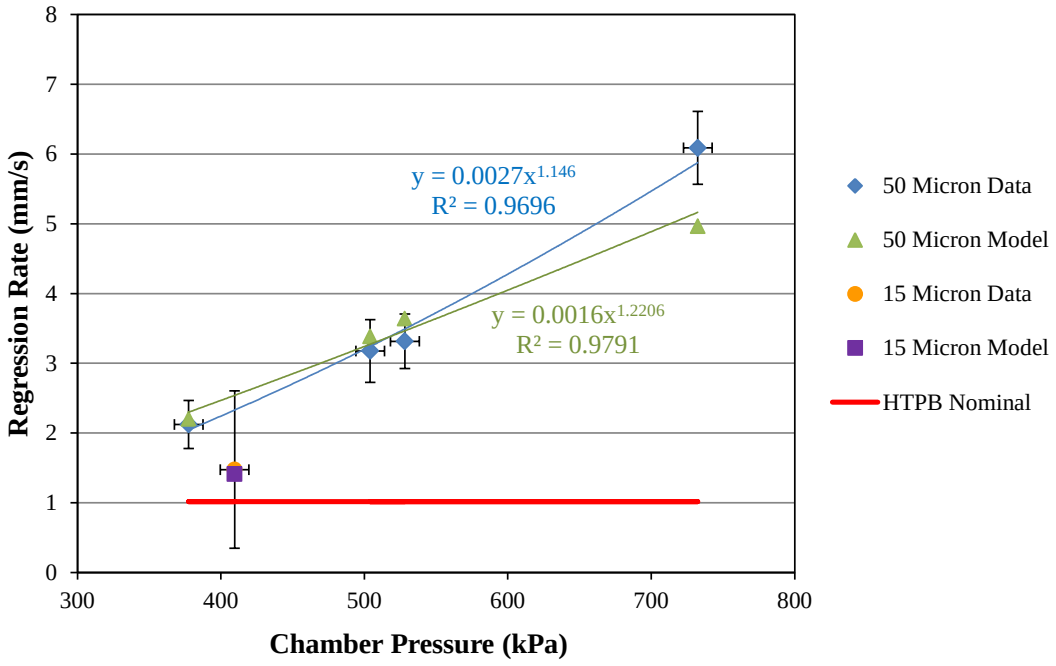

Figure 4.13. GOX 50 and 15 Micron Model Results

As with the 100 micron test articles, an oxidizer diameter value was determined for the 200, 50, and 15 micron test articles by minimizing the sum of the squares. This gave an oxidizer diameter value of 6.1 μm for the 200 micron test articles and 0 μm for the 50 and 15 micron test articles. The lower value for the 50 and 15 micron test articles as compared to the 100 micron test articles is expected as the smaller pore sizes should result in a less significant diffusion contribution. However, the lower value for the 200 micron test cases is unexpected as the larger pore size would be expected to increase the diffusion contribution. One potential cause is that the large percentage of tests of 100 micron test articles at the ~500 kPa condition biased the results of the 100 micron test articles due to their greater deviation from the simple flame model. While preliminary results from the 50 and 15 micron test articles follow the predictions of the GDF model, more tests and analysis of the 200 micron test articles would need to be

conducted to draw conclusions regarding the correlation of pore size and the GDF oxidizer particle diameter term.

4.3 N_2O Experimental Results

Data were successfully taken for seventeen hot-fire tests using N_2O. A few additional tests were conducted at high oxidizer flow rates and low chamber pressures, but the oxidizer flow rates were too high for the chamber pressure to obtain proper burning of the motor. Due to the limited supply of existing nozzle throat diameters and the uncertainty of which throat diameters would provide proper burning of the motor, variations in the chamber pressure for a given flow rate were obtained by supplying GN_2 pressurant to the combustion chamber.

Since the N2O tests were conducted to evaluate the change resulting from using a different oxidizer, the N2O tests only used 100 micron grains. A summary of the test results is shown in

Table 4.4 with fuller details on the test conditions provided in Appendix B. As with the GOX tests, the regression rate for each test was determined by measuring the length of each test article before and after each test to determine the grain regression and then dividing the regression by the burn time. Uncertainties for the experimental results were determined as described for the GOX results.

As can be seen in the table, the chamber pressures evaluated fall within the range of pressures evaluated using GOX. In addition, the regression rate for the N_2O tests was noticeably lower than that observed in the GOX tests. This result was expected due to the lesser reactivity of N_2O compared to GOX. The uncertainty of the chamber pressure is below 4% for each test, and the oxygen velocity uncertainty is around 12% for each

test. The regression rate uncertainty experienced a wide range of uncertainty across the various tests but typically fell below a value of 20%. The variation in regression rate uncertainty was typically caused by uneven cutting of the article which increased the uncertainty of the pretest article length or by uneven burning which increased the uncertainty of the posttest article length. However, the lower regression rates of the N_2O tests allowed for longer burn times which reduced the time component of the regression rate uncertainty.

Table 4.4. N_2O Experimental Results

Test Article	Chamber Pressure (kPa)	Chamber Pressure Unc. (%)	Oxidizer Velocity (m/s)	Oxidizer Velocity Unc. (%)	Regression Rate (mm/s)	Regression Rate Unc. (%)
101-1	207.3	4%	16.31	12%	0.21	83%
101-2	941.1	1%	8.69	12%	1.39	10%
101-3	806.3	1%	8.75	12%	1.11	5%
101-4	349.9	3%	13.99	12%	0.38	17%
101-5	1054.2	1%	8.54	12%	1.44	10%
101-6	456.3	2%	10.42	12%	0.54	14%
101-7	721.4	1%	9.27	12%	0.87	5%
101-8	304.8	3%	10.60	12%	0.35	5%
101-9	790.6	1%	8.22	12%	1.02	5%
101-10	540.1	2%	8.58	12%	0.67	24%
101-11	770.4	1%	7.43	12%	1.13	5%
101-12	614.3	1%	8.51	12%	0.80	14%
101-13	593.2	1%	8.92	12%	0.73	34%
101-14	672.5	1%	8.87	12%	0.91	7%
101-15	303.2	3%	9.37	12%	0.37	14%
101-16	408.0	2%	9.35	12%	0.50	9%
101-17	471.4	2%	8.86	12%	0.65	17%

To verify that the regression rate followed the same pressure trend as observed in the GOX tests, the regression rate for each of the seventeen N_2O tests was plotted against the chamber pressure. This plot is given in Figure 4.14. As can be seen in the figure, the regression rate follows the pressure trend as observed in the GOX tests. This similarity includes the near unity value of the pressure exponent indicating the presence of similar physics as in the GOX tests as well as the potential effects from variation in initial temperature and oxidizer mass flow rate.

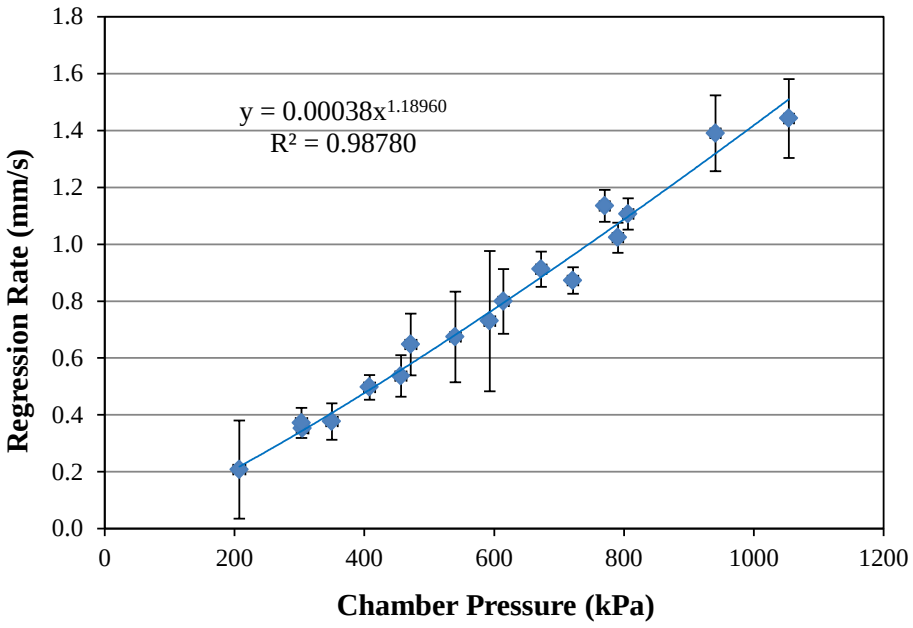

Figure 4.14. N_2O Regression Rate vs. Pressure

Additionally, to ensure that the N_2O results were indeed following a pressure dependency as opposed to an oxidizer mass flux dependency, the regression rate of the N_2O tests were also plotted against the oxidizer mass flow rate (since the test articles have an approximately constant burn area, the oxidizer mass flow rates are proportional

to the oxidizer mass flux). This plot is given in Figure 4.15. The blue data points are all the N_2O tests, the red data points are a set of tests at constant mass flow rate and varying pressure, and the green, purple, and orange data points are sets of test results at constant pressure and varying mass flow rate. As can be seen in the figure, the data points do tend to increase in regression rate with increasing mass flow rate due to using one nozzle throat diameter so that increases in oxidizer mass flow rate result in increases in chamber pressure. However, looking at the set of test conditions at the same oxidizer mass flow rate with varying chamber pressures (the red data points), it can be observed that the regression rate does increase with the chamber pressure (the higher regression rates correlate to higher chamber pressures). In addition, the three data sets with constant pressure and varying oxidizer mass flow rates (the green, purple, and orange data sets) show a slight decrease in the regression rate when increasing the oxidizer mass flow rate. These results support the conclusion that the regression rate of the N_2O test articles is dependent on the chamber pressure as opposed to the oxidizer mass flow rate. Also, the slight decrease in regression rate with increasing mass flow rate follows the trend predicted by the modified ablative model.

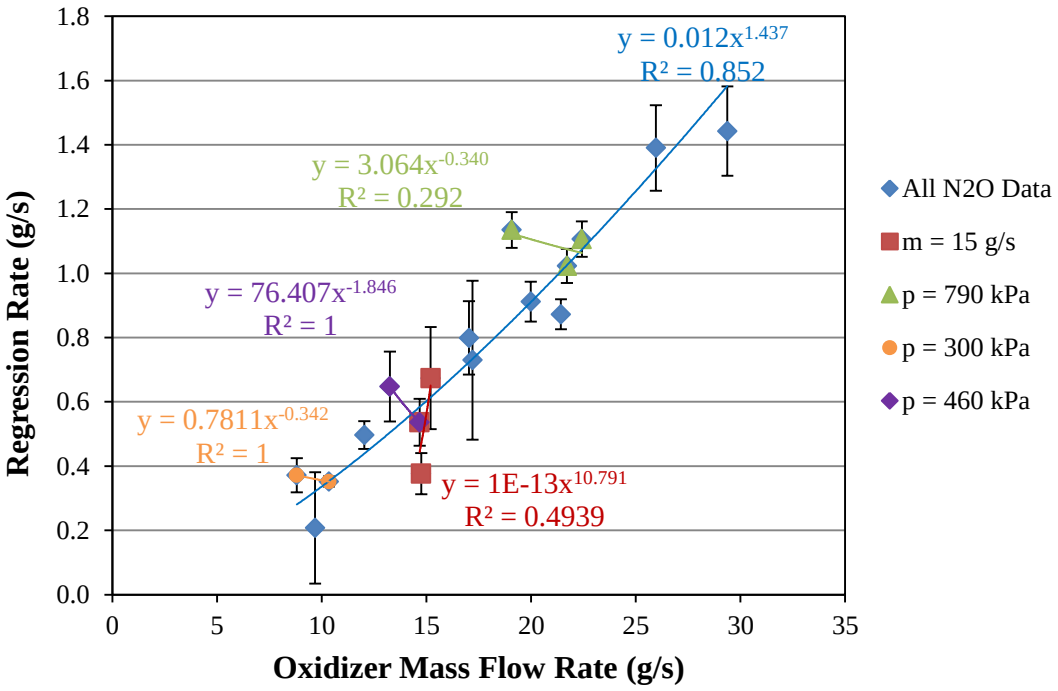

Figure 4.15. N_2O Regression Rate vs. Mass Flow Rate

4.4 N_2O Model Overview

As with the GOX data points, the flame coefficient for each N_2O test condition was determined using Eq. 2.11. The flame coefficients for the N_2O tests are shown plotted against chamber pressure in Figure 4.16. A power trendline for the flame coefficient as a function of pressure was determined from the data. As can be seen in the figure, the pressure exponent of the N_2O flame coefficient trendline is similar to that of the GOX flame coefficient trendline seen in Figure 4.6 (0.75 vs. 0.86). This similarity, along with the pressure dependency of the regression rate, indicates that the flame structure of the N_2O tests is similar to that of the GOX tests in that the flame structure behaves more like a flame seen in a solid rocket motor than one seen in a conventional

hybrid. However, the overall values of the N_2O flame coefficients are significantly lower (approximately one-fourth) than the values of the GOX flame coefficients.

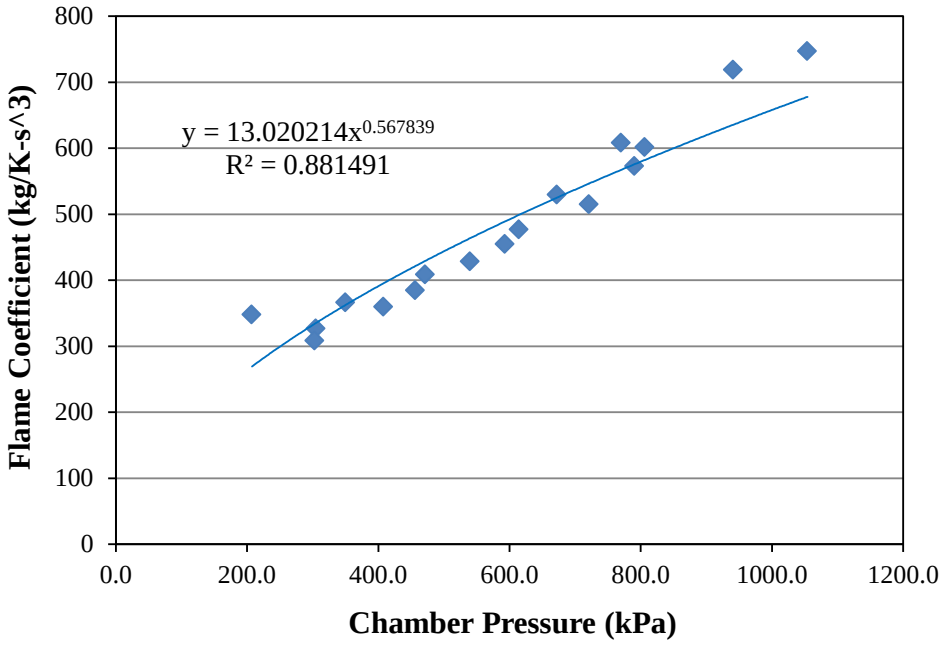

Figure 4.16. N_2O Flame Coefficient vs. Pressure

As with the GOX experiments, the contributions of the heat flux and advective terms as shown in Eq. 4.1 were calculated for the N_2O test articles. The magnitudes of both terms are plotted against chamber pressure in Figure 4.17. The blue trendline gives the pressure-based curve fit of the heat flux term for all N_2O test articles and the green trendline gives the pressure-based curve fit of the advective for all N_2O test articles. As can be seen in the trendlines, both the heat flux and advective terms show pressure dependency over the entire range of pressures tested (i.e. coefficient of determination values of 0.87 for the heat flux term and 0.80 for the advective term) suggesting that the pressure dependency in the N_2O test articles was due to the advective term as well as the

heat flux term. To further evaluate that possibility, curve fits of both terms were performed for only the test conditions with a chamber pressure above 600 kPa. The resulting trendlines are given in purple for the heat flux term and in red for the advective term. As can be seen in the figure, the curve fit of only the above 600 kPa conditions shows a strong dependence on chamber pressure for the heat flux term (i.e. coefficient of determination of 0.95) and a weak dependence on chamber pressure for the advective term (i.e. coefficient of determination of 0.37). These results for the above 600 kPa test conditions follow the conclusion drawn from the GOX results that the primary pressure dependency of the regression rate is due to the heat flux term as opposed to the advective term.

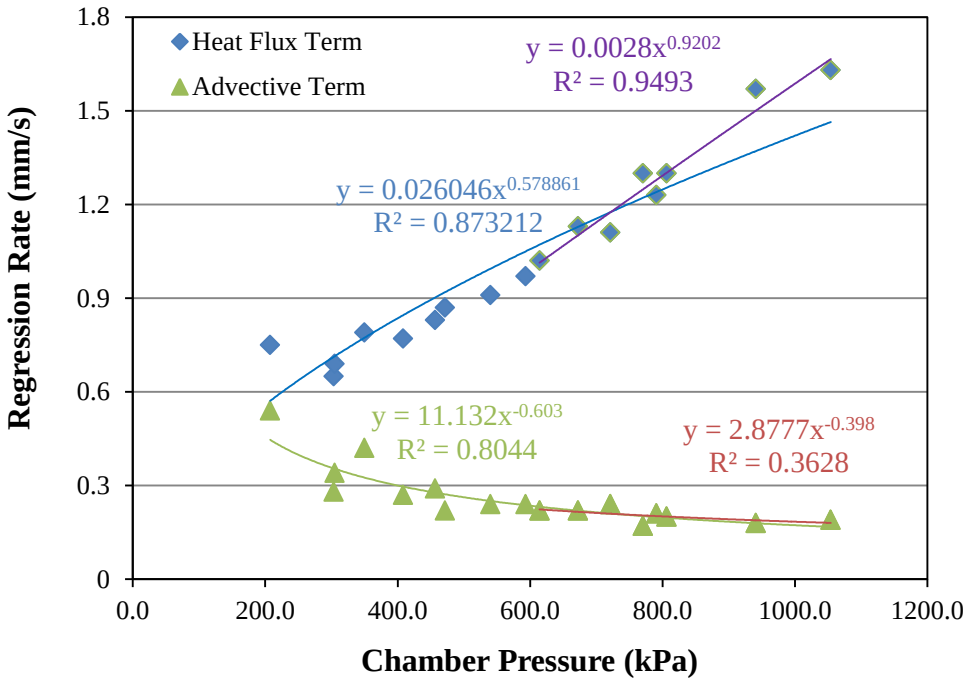

Figure 4.17. N_2O Regression Rate Contributions

In total, the results for the N_2O test articles show that the heat flux term has a strong pressure dependence for all chamber pressures tested while the pressure dependence of the advective term decreases with increasing chamber pressure. This result is reasonable as the thermal soak in an ablative model is inversely related to the regression rate (i.e. greater soak for lower regression rates). As such, for a pressure dependent regression rate, the thermal soak in the grain is also dependent on the regression rate allowing more heat transfer to the porous oxidizer flow resulting in a pressure dependency of the oxidizer enthalpy change. However, as the regression rate increases, the impact on the heat transfer starts to decrease resulting in the decreased pressure dependency of the advective term as shown in Figure 4.17.

Finally, using the assumption that the flame coefficient is equal to the thermal conductivity divided by the flame distance, it is expected that the flame height of the N_2O tests would be greater than that of the GOX tests due to the lower values of the flame coefficient calculated for the N_2O tests potentially caused by a decreased kinetic reaction rate in the N_2O tests. To evaluate that prediction of the conduction dominant assumption, images of the flame height of a GOX test and an N_2O test conducted at similar chamber pressures were compared. These images are shown in Figure 4.18. The image from the GOX test is shown on the left, and the image from the N_2O test is shown on the right. As can be seen in the figure, the flame structure from the N_2O test is noticeably larger than that from the GOX test. This predicted observation from the model fits with the difference in regression rate seen in the experimental data.

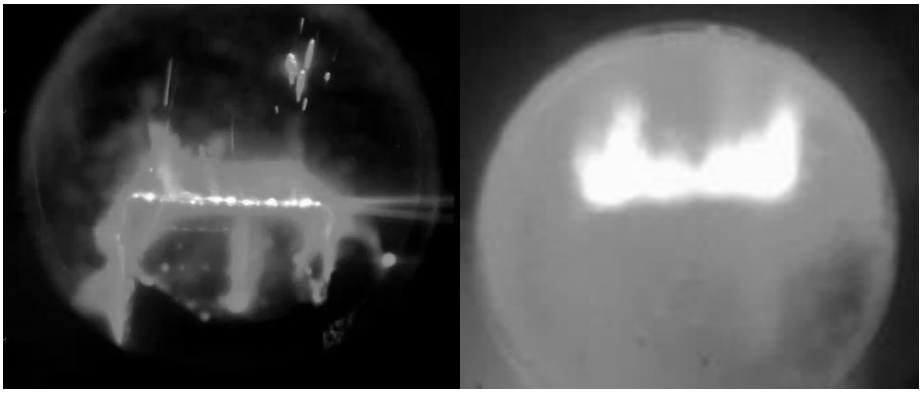

Figure 4.18. Flame Height Comparison (Left: GOX. Right: N_2O)

4.5 Test Article XCT Results

Preliminary XCT scans performed by Buckley on a test article evaluated using N_2O as the oxidizer indicated a lower solid fraction at the top surface postburn of 0.47 compared to the preburn condition of 0.53. Pictures showing a test article before and after a test are shown in Figure 4.19. The decrease in solid fraction after a test could be caused by thermal soak in the grain resulting in the fuel's slumping, by entrainment of solid particles into the oxidizer flow, or by uncertainty or error in the particular grain scanned. Some entrainment of solid particles has been observed in test videos, and visual inspection of the N_2O test articles postburn has indicated the possibility of the potential occurrence of thermal soak into the test articles. However, since the amount of XCT scan data is limited, additional scans would need to be completed to evaluate the change in solid fraction over a multitude of test articles in order to draw any conclusions on the cause of the change in the solid fraction. In addition, the effect of uneven burning that can be seen in Figure 4.19 could be better described and understood through scans of additional test articles.

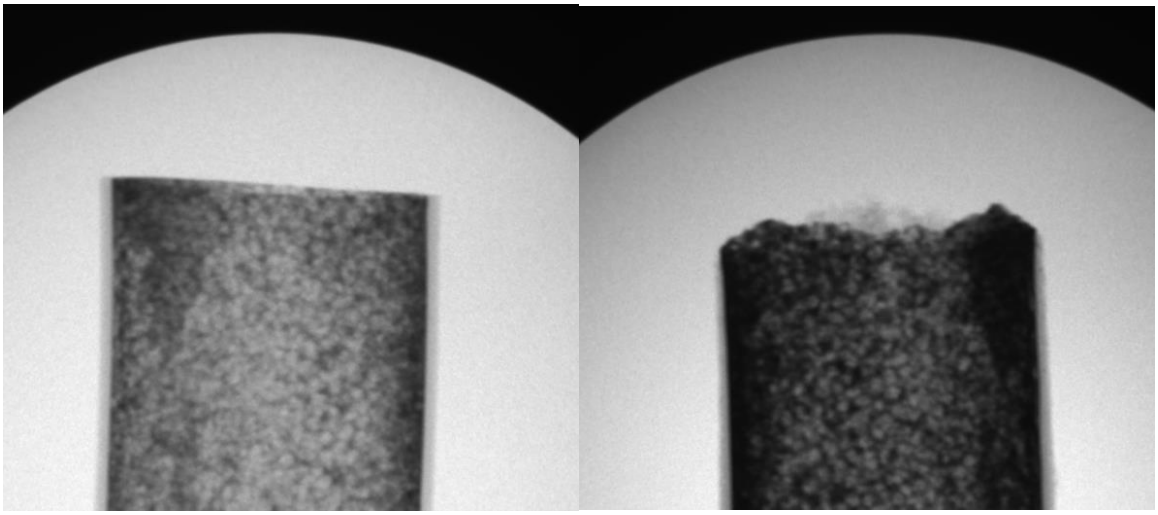

Figure 4.19. XCT Scans (Left: Prefire. Right: Postfire) [Courtesy: Buckley]

CHAPTER 5

CONCLUSIONS

Results from the experiments using GOX as the oxidizer show that the axial-injection, end-burning hybrid has the potential for significantly increasing regression rates and fuel mass fluxes as compared to conventional hybrid rocket motor configurations. Pressures tested ranged from atmospheric to 1160 kPa and oxidizer injection velocities ranged from 35 m/s to 87 m/s for the gaseous oxygen tests. Regression rates ranged from approximately 0.75 mm/s at atmospheric pressure to 8.89 mm/s at 1160 kPa The regression rate was primarily driven by the chamber pressure with a minimal impact from the oxidizer mass flow rate as demonstrated by a comparison of the effects of the heat flux and advective terms described in the modified ablative model as shown in Eq. 4.1. These results are in agreement with those of Nagata et al. who observed regression rates ranging from 1 mm/s at atmospheric to approximately 7 mm/s at 1128 kPa for his type-B tubes as opposed to those of Li et al. who did not observe any increase of regression rate in the axial-injection, end-burning configuration. Curve fits of the experimental results as a power function of the chamber pressure yielded exponents around one. For a solid rocket, this result would indicate that pressure disturbances would be amplified due to the pressure disturbance's increasing the motor's burn rate. However, since the oxidizer flow rate is independent of the chamber pressure

in an axial-injection, end-burning hybrid motor, the implications of a near-unity pressure exponent in an axial-injection, end-burning hybrid rocket motor would need to be further investigated.

Additionally, the modified ablative model along with the new application of GDF theory to model the flame in an axial-injection, end-burning hybrid was successful in fitting the GOX experimental data. This agreement between the experimental and model results indicates that a GDF-based approach has promise for modeling the flame in a porous axial-injection, end-burning hybrid. Results from the model indicate that the kinetic effects limit the combustion and thus the regression rate at lower chamber pressures while the diffusion processes become more significant as the chamber pressure increases. This effect is considered to become significant around a chamber pressure of 400 kPa for the 100 micron case as the kinetic only and the kinetic and diffusion curves start to deviate around that pressure. However, the impact of the diffusion contribution varies for each test article porosity with the 15 and 50 micron test articles' not showing an observable diffusion contribution over the range of pressures tested. Future work on the model should focus on determining the effect of pore size on the oxidizer particle diameter term in the GDF flame model. Preliminary results from this study have indicated that smaller pore sizes may result in smaller oxidizer particle diameters but a in depth study would be required to verify that trend and to determine the actual relationship.

New results on N_2O tests supported the theory that regression rate of axial-injection, end-burning hybrid rocket motors is proportional to the chamber pressure in general and not just when using GOX as the oxidizer. Pressures tested ranged from

207 kPa to 1054 kPa, and oxidizer injection velocities ranged from 7.5 m/s to 16.8 m/s for the N_2O tests. Regression rates ranged from approximately 0.21 mm/s at 207 kPa to 1.44 mm/s at 1054 kPa. While the N_2O results followed the pressure trend, the magnitude of the regression rate was significantly lower than the regression rate observed in the GOX tests. This decrease could correspond to an increase in the flame height potentially caused by a decreased kinetic reaction rate. This was qualitatively confirmed through visual observation but has not yet been quantitatively confirmed through applying the GDF model due to the need of a HDPE/N_2O global reaction. Future work in analyzing the N_2O results should focus on developing an elementary reaction model for determining the global reaction parameters.

In summary, this research evaluated the combustion and heat mechanisms controlling regression rate of axial-injection, end-burning hybrid fuel grains with laboratory-scale experiments and described them with an analytical ablative model using a new application of GDF theory. Results from the experiments, including new work using N_2O as the oxidizer, show that the axial-injection, end-burning configuration has the capability of increasing the fuel mass flux as compared to conventional designs. The results of the model demonstrated the importance of both kinetic and diffusion effects in the performance of axial-injection, end-burning hybrid rocket motors. Both the experiments and the model show that the axial-injection, end-burning hybrid configuration provides an improvement to the regression rate of conventional hybrids.

APPENDICES

APPENDIX A

TEST ARTICLE SOLID FRACTION DATA

Table A.1. HDPE Density

Grain	Mass (g)	Volume Displacement (mL)	Density (g/cm^3)
10A	5.4799	6	0.913
10B	5.4618	6	0.910
10C	5.4108	6	0.902
10D	5.2932	5.8	0.913
		Average	0.91
		Standard Deviation	0.005

Table A.2. GOX 100 Micron Solid Fraction

Grain	Mass (g)	Length (mm)	Diameter (mm)	Density (g/cm^3)
101	5.4718	38.63	19.95	0.453
102	5.2421	37.16	19.98	0.450
103	5.3820	38.32	20.02	0.446
104	5.4160	38.19	19.96	0.453
			Average	0.451
			Solid Fraction	0.50

Table A.3. GOX 50 Micron Solid Fraction

Grain	Mass (g)	Length (mm)	Diameter (mm)	Density (g/cm^3)
51	5.8398	36.79	19.66	0.523
52	5.8066	36.88	19.52	0.526
53	5.7916	36.61	19.74	0.517
54	5.7884	36.70	19.85	0.510
55	5.7604	36.83	19.38	0.530
			Average	0.521
			Solid Fraction	0.57

Table A.4. GOX 15 Micron Solid Fraction

Grain	Mass (g)	Length (mm)	Diameter (mm)	Density (g/cm^3)
15	7.5132	42.19	19.80	0.579
16	7.3454	41.39	19.66	0.585
17	7.3985	41.17	19.76	0.586
18	7.5052	42.72	19.76	0.573
			Average	0.80
			Solid Fraction	0.64

Table A.5. GOX 200 Micron Solid Fraction

Grain	Displaced Volume (mL)	Length (mm)	Diameter (mm)	Solid Fraction
201	8.2	51.26	20.59	0.481
202	8.5	52.15	20.63	0.488
203	8.5	51.26	20.63	0.496
204	8.6	51.40	20.67	0.499
			Average	0.49

Table A.6. N_2O 100 Micron Solid Fraction

Grain	Displaced Volume (mL)	Length (mm)	Diameter (mm)	Solid Fraction
101N	8	52.33	20.55	0.461
102N	8.5	54.56	20.33	0.480
103N	7.9	50.72	20.49	0.473
104N	8.5	53.58	20.52	0.480
			Average	0.47

APPENDIX B

PRESSURE TEST DATA

Table B.1. GOX Pressure Test Conditions

Test Article	Venturi Pressure (MPa)	Injector Pressure (MPa)	Venturi Temperature (K)	Injector Temperature (K)	Venturi Diameter (in.)
15-1	2.83	2.76	299.4	300.3	0.120
50-1	3.66	2.12	299.8	300.9	0.120
50-2	2.86	1.66	300.1	299.6	0.120
50-4	2.80	1.66	296.5	299.2	0.120
50-5	2.06	1.19	277.8	282.9	0.120
100-2	1.22	0.24	276.9	284.1	0.080
100-6	3.66	0.63	286.5	287.8	0.080
100-7	3.45	0.59	294.9	294.4	0.080
100-8	5.63	0.95	286.6	288.1	0.080
100-9	5.64	1.00	286.6	287.1	0.080
100-10	6.60	1.55	296.9	298.1	0.080
100-11	6.50	1.26	297.1	297.3	0.080
100-12	5.96	1.14	297.2	299.4	0.080
100-13	3.78	2.00	291.6	294.1	0.120
100-14	6.43	2.43	292.4	293.4	0.120
100-15	6.00	2.72	293.0	295.5	0.120
100-16	2.94	1.17	295.5	299.2	0.120
100-17	2.79	0.97	297.1	300.0	0.120
200-1	0.67	0.37	285.2	286.7	0.120
200-2	3.07	1.48	285.2	289.9	0.120
200-3	2.15	1.12	280.0	288.5	0.120
200-4	3.38	1.51	282.8	289.4	0.120

Table B.2. N_2O Pressure Test Conditions

Test Article	Orifice Pressure (MPa)	Injector Pressure (MPa)	Orifice Temp. (K)	Injector Temp. (K)	N_2O Orifice Dia. (in.)	GN_2 Orifice Pressure (MPa)	GN_2 Orifice Temp. (K)	GN_2 Orifice Dia. (in.)
101-1	1.05	0.25	302.5	302.3	0.063	-	-	-
101-2	2.67	0.98	302.8	301.8	0.063	-	-	-
101-3	2.30	0.84	297.1	298.6	0.063	-	-	-
101-4	1.55	0.40	297.1	299.3	0.063	-	-	-
101-5	2.95	1.11	297.8	296.6	0.063	-	-	-
101-6	1.54	0.49	296.9	297.2	0.063	-	-	-
101-7	2.20	0.76	295.4	294.3	0.063	-	-	-
101-8	1.06	0.32	280.2	279.8	0.063	0.52	281.4	0.063
101-9	2.13	0.83	280.1	285.2	0.063	1.16	283.3	0.063
101-10	1.53	0.56	280.3	283.4	0.063	0.88	282.6	0.063
101-11	1.90	0.80	280.7	285.9	0.063	1.15	283.2	0.063
101-12	1.73	0.65	283.6	287.4	0.063	1.10	285.1	0.063
101-13	1.74	0.63	283.8	287.1	0.063	1.10	284.7	0.063
101-14	1.99	0.70	283.6	282.1	0.063	0.67	291.9	0.063
101-15	0.92	0.32	285.6	289.1	0.063	0.90	287.6	0.063
101-16	1.24	0.43	286.5	289.1	0.063	0.81	289.5	0.063
101-17	1.36	0.49	286.7	290.6	0.063	0.84	290.7	0.063

APPENDIX C

UNCERTAINTY ANALYSIS

To determine the accuracy of the experimental results, an uncertainty analysis was conducted for the regression rate and the oxidizer velocity. Due to the simplicity of the data reduction equation, a Taylor Series Method (TSM) analysis was performed for the regression rate of each test article while a Monte Carlo Method (MCM) analysis was performed for the oxidizer velocity due to the increased complexity of the oxidizer velocity data reduction equation.

For a TSM analysis, the uncertainty for a measurement with uncorrelated errors is calculated using the equation

$$U_r = \sqrt{\sum \left(\frac{\partial r}{\partial x_i} \cdot U_i\right)^2} \tag{C.1}$$

where U_r is the uncertainty of the calculated parameter, r is the calculated parameter, x_i is the contributing parameter, and U_i is the uncertainty of the contributing parameter. Given that the regression rate was calculated by taking the difference in the pretest and posttest grain lengths and dividing by the burn time, the TSM analysis equation for the standard uncertainty of the regression rate is given as

$$u_{\dot{r}} = \sqrt{\left[\left(\frac{x_1 - x_2}{\Delta t^2}\right) u_{\Delta t}\right]^2 + \left[-\left(\frac{1}{\Delta t}\right) u_{x1}\right]^2 + \left[\left(\frac{1}{\Delta t}\right) u_{x2}\right]^2} \tag{C.2}$$

where $u_{\dot{r}}$ is the standard uncertainty of the regression rate, x_1 is the pretest length of the test article, x_2 is the posttest length of the test article, Δt is the burn time, $u_{\Delta t}$ is the standard uncertainty of the burn time, u_{x1} is the standard uncertainty of the pretest length

of the test article, and u_{x2} is the standard uncertainty of the posttest length of the test article.

The uncertainties of the pretest and posttest lengths were determined by the standard deviation of the measurements. For both measurements, the random uncertainty was significantly larger (over an order of magnitude) than the uncertainty due to resolution and enabled the resolution uncertainty to be neglected.

A standard uncertainty of 0.08 s was used for the burn time based on using a sample frequency of 200 Hz. This value was selected by assigning a standard uncertainty of fifteen frames to the start of burning and five frames to the end of burning. The higher value for the start of burning was chosen due to the start's being determined by evaluating the high speed image of the combustion to see when the flame spread across the surface of the grain. A fifteen frame standard uncertainty at 200 Hz provided a ±0.15 s expanded uncertainty for that parameter. The lower value of five frames for the standard uncertainty of the end of burning was due to using the minimum value of the time derivative of pressure to establish the end of the burn time [61]. These values were then combined using Eq. 4.1 to provide a total standard uncertainty for the burn time.

For the Monte Carlo Method (MCM), the nominal value and the standard uncertainties for each variable are determined. Next, a series of iterations are run where the random values of the standard uncertainties from specified distributions (e.g. Gaussian, square, triangular, etc.) are added to their respective variables and are then used to calculate the result. After all the iterations have been completed, the results are averaged to find the final value of the result, and the standard deviation is calculated to determine the standard uncertainty of the result. A diagram illustrating the process of a

MCM is given in Figure C.1 [62]. Since this experiment yielded one dominant standard uncertainty for each parameter, it was determined to combine the random and systematic standard uncertainties for each parameter. In addition, each uncertainty was assumed to follow a Gaussian distribution. A table of the standard uncertainties for calculating the oxidizer mass flow rate for sample 100-16 is shown in Table C.1 along with the source of the uncertainty.

Pressure measurement uncertainties were determined through in-house calibration of the uncertainty. While the temperature and venturi discharge coefficient uncertainties were specified by the manufacturer, other uncertainties were determined by the standard deviation of the measurement to ascertain the random uncertainty. For this experiment, ten thousand iterations of the MCM were conducted for each test condition. Due to the simplicity of the equations, a large number of iterations were able to be conducted without difficulty which aided in ensuring that the most accurate values for the uncertainty were determined.

Table C.1. Test Article 100-16 Standard Uncertainties

Parameter	Value	Units	Source
Grain Diameter	0.5	mm	Random
Grain Void Fraction	0.025	-	Random
Venturi Pressure	4.2	kPa	Calibration
Venturi Temperature	0.5	K	Manufacturer
Venturi Throat Diameter	0.013	mm	Assumed
Discharge Coefficient	0.01	-	Manufacturer
Chamber Pressure	8.5	kPa	Calibration

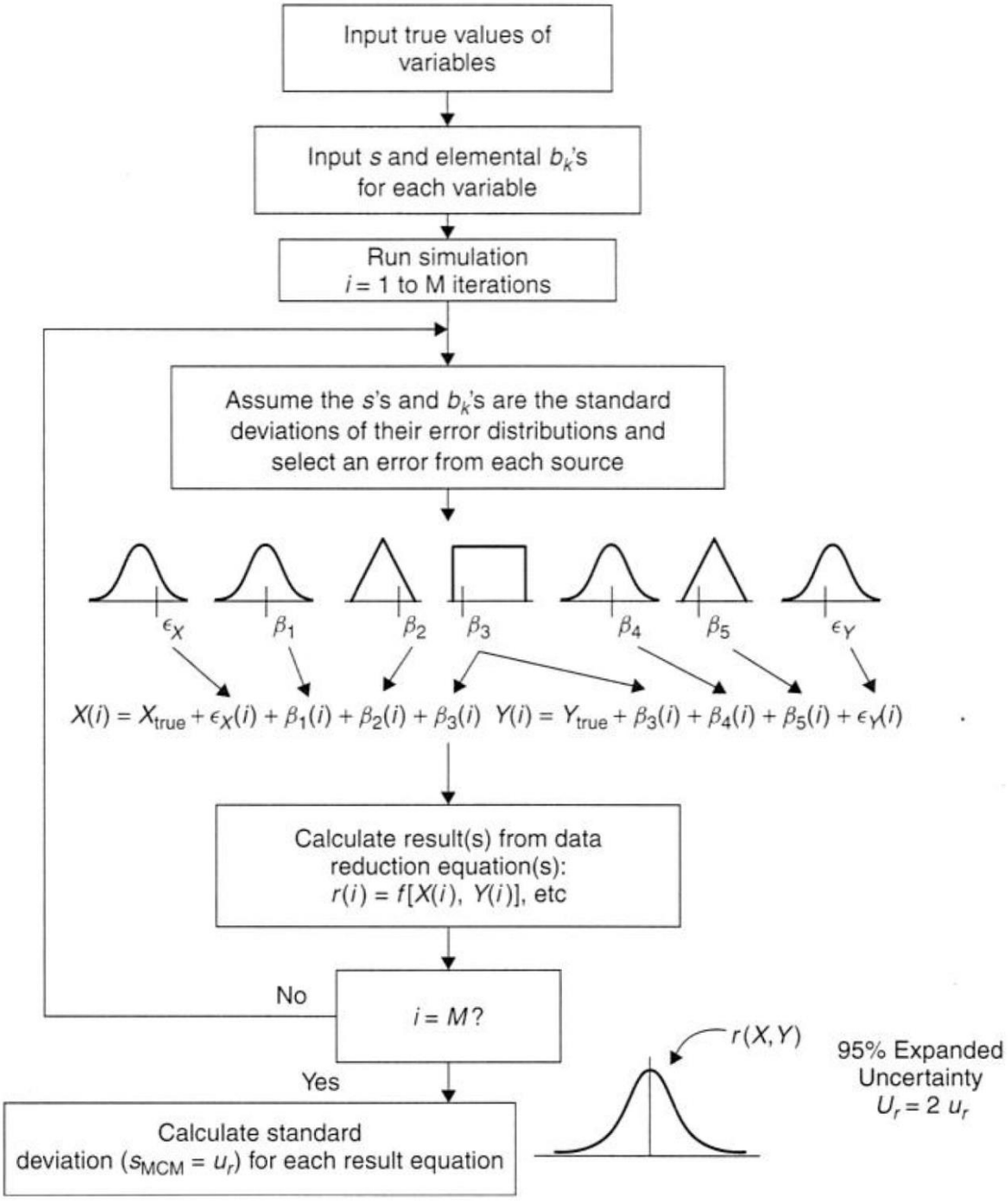

Figure C.1. Monte Carlo Method Approach [62]

APPENDIX D

PHOTOGRAPHIC DATA

Figure D.1. Article 100-10 Posttest (GOX)

Figure D.2. Article 100-11 Posttest (GOX)

Figure D.3. Article 100-12 Posttest (GOX)

Figure D.4. Article 50-1 Posttest (GOX)

Figure D.5. Article 50-2 Posttest (GOX)

Figure D.6. Article 15-1 Posttest (GOX)

Figure D.7. Article 200-2 (GOX)

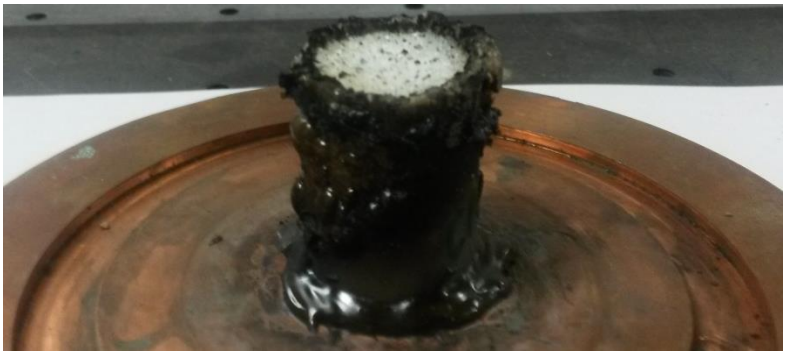

Figure D.8. Article 101-3 (N_2O)

Figure D.9. Article 101-13 (N_2O)

APPENDIX E

DERIVATION OF GDF MODEL LENGTHS

This appendix provides a derivation of the Granular Diffusion Flame model based on that performed by Condon and Osborn [67] and Summerfield et al. [52]. Key assumptions for the GDF model include:

- One dimensional,
- Gas phase flame,
- Conduction heat transfer from flame to grain,
- Fuel and oxidizer released as pockets of vapor,
- Oxidizer pocket size connected to the average particle size
- Both kinetic and diffusion effects contribute to reaction location, and
- Only gas phase mixing of fuel and oxidizer [67].

To start, an energy balance of the propellant was performed as shown in Figure E.1. As can be seen in the figure, the energy balance is an ablative model as discussed in Chapter 2. Performing the energy balance results in the equation

$$k_g \frac{(T_{fl}-T_s)}{L} = \dot{m}_t'' c_p (T_s - T_o) - \dot{m}_t'' Q_s \tag{E.1}$$

where k_g is the thermal conductivity of the gases, T_{fl} is the flame temperature, T_s is the surface temperature of the propellant, L is the reaction zone length, $\dot{m}_t''$ is the mass flux of the propellant, c_p is the specific heat of the propellant, T_o is the initial temperature of the propellant, and Q_s is the heat release of the propellant.

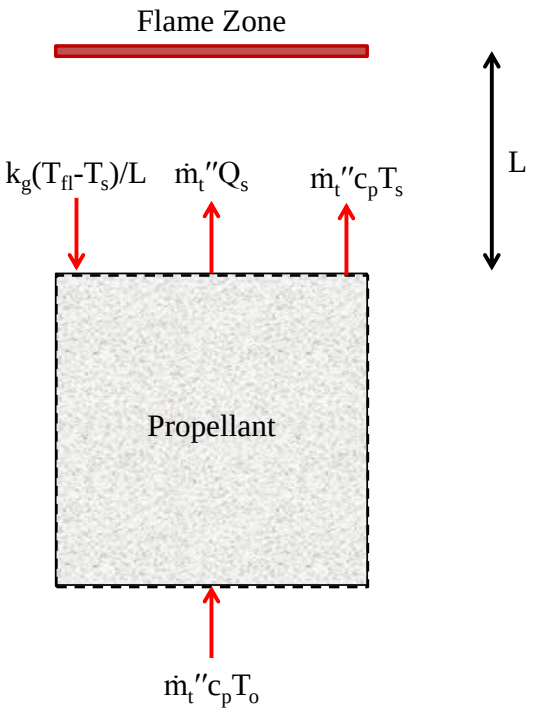

Figure E.1. GDF Energy Balance [67]

In order to solve Eq. E.1 to find the mass flux of the propellant, the reaction zone length must be determined. For the model shown in Figure E.1, the length of the reaction zone can be found using the equation:

$$L = u \cdot \tau \tag{E.2}$$

where u is the velocity of the propellant gas escaping the control volume and τ is the residence time of the gases in the reaction zone. To find the reaction zone length, both the velocity and the residence time need to be determined. The velocity of the propellant gas is equal to the mass flux divided by the density of the gas. This is given by the equation

$$u = \frac{\dot{m}_t''}{\rho_g} \tag{E.3}$$

where ρ_g is the density of the propellant gas.

As stated in the assumptions list, both kinetic and diffusion effects are considered to be significant. For the GDF model, the reaction zone length is considered to be a summation of the kinetic and diffusion contributions. To find the kinetic contribution to the reaction zone length, the residence time is determined assuming a global second order reaction of the mixed gases using an Arrhenius function. This results in the equation

$$\tau = \left[(1-\epsilon)^2 \rho_g A e^{\left(-E_a/RT_g\right)}\right]^{-1} \tag{E.4}$$

where ε is a function of the reaction products (equal to zero at the propellant surface and one at reaction completion), A is the pre-exponential factor of the Arrhenius function, E_a is the activation energy of the reaction, R is the gas constant of the propellant, and T_g is the average temperature of the hot gases. The GDF model assumes that the $(1-\varepsilon)^2$ term is approximately equal to one over the flame zone indicating that the reaction occurs near the propellant surface. Using that assumption, Eqs. E.3 and E.4 can be substituted into Eq. E. 2 to yield the equation:

$$L_k = \frac{\dot{m}_t''}{\rho_g A e^{\left(-E_a/RT_g\right)}} \tag{E.5}$$

where L_k is the kinetic reaction zone length. Next, Eq. E.5 can be solved for the mass flux, substituted into Eq. E.1 (assuming that L in Eq. E.1 only includes the kinetic contribution), and solved for the kinetic reaction zone length to yield the equation:

$$L_k = \frac{\sqrt{k_g\left(T_{fl}-T_s\right)}}{\rho_g \sqrt{c_p(T_s-T_o)-Q_s}\sqrt{A e^{\left(-E_a/RT_g\right)}}} \tag{E.6}$$

where all terms have been previously defined. Finally, Eq. E.6 can be further refined by assuming that the density of the gases follows ideal gas law. Applying that assumption results in the equation

$$L_k = \frac{\sqrt{k_g(T_{fl}-T_s)}}{\sqrt{c_p(T_s-T_o)-Q_s}} \cdot \frac{RT_g}{\sqrt{Ae^{\left(-Ea/RT_g\right)}}} \cdot \frac{1}{p_{ch}} \tag{E.7}$$

where p_{ch} is the chamber pressure. As can be seen in the equation, the kinetic reaction zone length is inversely proportional to the chamber pressure.

Next, the diffusion contribution to the reaction zone length can be found using the diffusion residence time of

$$\tau = \frac{d^2}{D_g} \tag{E.8}$$

where d is the particle diameter and D_g is the binary diffusivity of the oxidizer and fuel vapors. As stated in the assumptions, as the propellant vaporizes, it forms pockets of fuel vapor and oxidizer vapor. The particle diameter can be related to the mass in the vapor pockets using the equation

$$\mu = \rho_g d^3 \tag{E.9}$$

where μ is the vapor pocket mass. By substituting Eqs. E.3, E.8, and E.9 into Eq. E.2, the following expression for the diffusion reaction zone length is obtained

$$L_D = \frac{\dot{m}_t'' \mu^{2/3}}{\rho_g^{5/3} D_g} \tag{E.10}$$

where L_D is the diffusion reaction zone length. Solving Eq. E.10 for the mass flux, substituting into Eq. E.1 (assuming that L in Eq. 1 only includes the diffusion contribution), and solving for the diffusion reaction zone length yields the equation

$$L_D = \frac{\sqrt{k_g(T_{fl}-T_s)}}{\sqrt{c_p(T_s-T_o)-Q_s}} \cdot \frac{\mu^{1/3}}{\rho_g^{5/6} D_g^{1/2}} \tag{E.11}$$

where all terms have been previously defined. Equation E.11 can be further refined by substituting relationships for the pocket mass and binary diffusivity terms. The binary diffusivity can be found using the equation

$$D_g = k_1 \frac{T_g^{3/2}}{p_{ch}} \tag{E.12}$$

where k_1 is a binary diffusivity parameter including the contributions from the Boltzmann constant, molecular mass, and molecular diameter [47]. Next the pocket mass can be defined according the oxidizer particle diameter using the equation

$$\mu^{1/3} = k_2^{1/3} d_o \tag{E.13}$$

where k_2 is the pocket density and d_o is the oxidizer particle diameter. Substituting Eqs. E.12 and E.13 into Eq. E.14 and applying the ideal gas law for the gas density yields the equation

$$L_D = \frac{\sqrt{k_g(T_{fl}-T_s)}}{\sqrt{c_p(T_s-T_o)-Q_s}} \cdot \frac{k_2^{1/3} R^{5/6} T_g^{1/12}}{k_1^{1/2}} \cdot \frac{d_o}{p_{ch}^{1/3}} \tag{E.14}$$

where all terms have been previously defined. By summing the kinetic reaction zone length given in Eq. E.7 and the diffusion reaction zone length given in Eq. E.14, the total reaction zone length can be obtained thus giving the flame location in the model.

REFERENCES

[1] Sutton, G. P., and Biblarz, O., *Rocket Propulsion Elements*, 8th ed., John Wiley & Sons, Inc., Hoboken, New Jersey, 2010.

[2] Lestrade, J.-Y., Anthoine, J., Verbene, O., Boiron, A. J., Khimeche, G., and Figus, C., "Experimental Demonstration of the Vacuum Specific Impulse of a Hybrid Rocket Engine," *50th AIAA/ASME/SAE/ASEE Joint Propulsion Conference*, Cleveland, OH, AIAA 2014-3951, 2014.

[3] Ronningen, J. E., "Post-flight Analysis of a Hybrid Test Rocket Flight," *59th International Astronautical Congress*, Glascow, United Kingdom, September 29 – October 3 2008, IAC-08-C4.2.7.

[4] Hitt, M. A., Taylor, T., and Frederick, R. A., "Design of a 3-D Printed Unified Hybrid Motor," *50th AIAA/ASME/SAE/ASEE Joint Propulsion Conference*, Cleveland, OH, AIAA-2014-3498, 2014.

[5] Eilers, S. D., Whitmore, S. A., and Peterson, Z. W., "Regeneratively Cooled Multiple-Use Plug Hybrid for Nanosatellites," *Journal of Propulsion and Power*, Vol. 29, No. 6, November-December 2013.

[6] Whitmore, S. A., Peterson, Z. W., and Eilers, S. D., "Comparing Hydroxyl Terminated Polybutadiene and Acrylonitrile Butadiene Styrene as Hybrid Rocket Fuels," *Journal of Propulsion and Power*, Vol. 29, No. 3, May-June 2013.

[7] Hirata, Y., Aso, S., Hayashida, T., Nakawatase, R., Tani, Y., Morishita, K., and Shimada, T., "Improvement of Regression Rate and Combustion Efficiency of High Density Polyethylene Fuel and Paraffin Fuel of Hybrid Rockets with Multi-Section Swirl Injection Method," *47th AIAA/ASME/SAE/ASEE Joint Propulsion Conference*, San Diego, CA, AIAA 2011-5907, 2011.

[8] Whitmore, S. A., Walker, S. D., Merkley, D. P., and Sobbi, M., "High Regression Rate Hybrid Rocket Fuel Grains with Helical Port Structures," *50th AIAA/ASME/SAE/ASEE Joint Propulsion Conference*, Cleveland, OH, AIAA 2014-3751, 2014.

[9] Whitmore, S. A., Inkley, N. R., and Merkley, D. P., "Development of a Power Efficient, Restart-Capable Arc Ignitor for Hybrid Rockets," *50th AIAA/ASME/SAE/ASEE Joint Propulsion Conference*, Cleveland, OH, AIAA 2014-3949, 2014.

[10] Whitmore, S. A., Wilson, J. R., Ritter, M. A., and Williams, L. T., "Pyrolysis of Acrylonitrile-Butadiene-Styrene (ABS) Under High Heat Flux Conditions," *50th AIAA/ASME/SAE/ASEE Joint Propulsion Conference*, Cleveland, OH, AIAA 2014-3752, 2014.

[11] McCulley, J. M., "Design and Testing of Digitally Manufactured Paraffin Acylonitrile-Butadiene-Styrene Hybrid Rocket Motors," M.S. Thesis, Department of Mechanical and Aerospace Engineering, Utah State University, Logan, UT, 2012.

[12] Dushku, M. and Mueller, P., "Additively Manufactured Propulsion System," SSC12,III-2, 26th Annual AIAA/USU Conference on Small Satellites, Logan, UT, 2012.

[13] AIAA Hybrid Rocket Technical Committee, "A Short Course on the Concept, Systems, Applications, and Operating Principles of Hybrid Rockets," presented at the 31st Joint Propulsion Conference and Exhibit, San Diego, CA, July 1995.

[14] Carmicino, C. and Sorge, An. R., "Role of Injection in Hybrid Rockets Regression Rate Behavior," *Journal of Propulsion and Power*, Vol. 21, No. 4, July-August 2005.

[15] Marxman, G. A. and Gilbert, M., "Turbulent Boundary Layer Combustion in the Hybrid Rocket," *Ninth International Symposium on Combustion*, Academic Press, New York 1963, pp. 371-383.

[16] Chiaverini, M., "Review of Solid-Fuel Regression," *Fundamentals of Hybrid Rocket Combustion and Propulsion*, edited by Chiaverini, M. and Kuo, K., Vol. 218, Progress in Astronautics and Aeronautics, AIAA, Reston, VA, 2007, pp. 37-125.

[17] Marxman, G. A., Woolridge, C.E., and Muzzy, R. J., "Fundamentals of Hybrid Bounary Layer Combustion," *Heterogeneous Combustion*, edited by H. G. Wolfhard, I. Glassman, and L. Green, Jr., Vol. 15, AIAA Progress in Astronautics and Aeronautics, Academic Press, New York, 1964, pp. 485-521.

[18] Altman, D. and Humble, R., "Hybrid Rocket Propulsion Systems," *Space Propulsion Analysis and Design*, edited by Humble, R. W., Henry, G. N., and Larson, W. J., The McGraw-Hill Companies, Inc., Primis Custom Publishing, New York, 1995, p. 379.

[19] Marxman, G. A., "Combustion in the Turbulent Boundary Layer on a Vaporizing Surface," *Tenth Symposium (International) on Combustion*, Combustion Inst., Pittsburgh, PA, 1965, pp. 1337-1349.

[20] Marxman, G. A., "Boundary-Layer Combustion in Propulsion," *Eleventh Symposium (International) on Combustion*, Combustion Inst., Pittsburgh, PA, 1966, pp. 269-289.

[21] Muzzy, R. J., "Applied Hybrid Combustion Theory," AIAA Paper 72-1143, 1972.

[22] Wongyai, P. and Greatrix, D. R., "Regression Rate Estimation for Swirling-Flow Hybrid Rocket Engines," *50th AIAA/ASME/SAE/ASEE Joint Propulsion Conference*, Cleveland, OH, AIAA 2014-3750, 2014.

[23] Knuth, W. H., Chiaverini, M. J., Sauer, J. A., and Gramer, D. J., "Solid-Fuel Regression Rate Behavior of Vortex Hybrid Rocket Engines," *Journal of Propulsion and Power*, Vol. 18, No. 3, May-June 2002.

[24] Ohe, K., Mizuchi, M., Aso, S., Tani, Y., Ohyama, S., Araki, K., Tada, H., and Shimada, T., "Study on Hybrid Rocket with Multi-Section Swirl Injection Method toward Flight Experiments of Subscale Space Plane," *50th AIAA/ASME/SAE/ASEE Joint Propulsion Conference*, Cleveland, OH, AIAA 2014-3954, 2014.

[25] Tada, H., Aso, S., Tani, Y., Ohyama, S., Araki, K., Ohe, K., Mizuchi, M., and Shimada, T., "Visualization of Flames in Combustion chamber of Hybrid Rocket Engine with Multi-Section Swirl Injection Method," *50th AIAA/ASME/SAE/ASEE Joint Propulsion Conference*, Cleveland, OH, AIAA 2014-3850, 2014.

[26] Whitmore, S. A., Walker, S. D., and Merkley, D. P., "Engineering Model for Hybrid Rocket Regression Rate Amplification by Helical Ports," *51st AIAA/ASME/SAE/ASEE Joint Propulsion Conference*, Orlando, FL, AIAA 2015-3745, 2015.

[27] McKnight, B. R., Armold, D., Boyer, J. E., Kuo, K. K., DeSain, J. D., Fuller, J. K., Brady, B. B., and Curtiss, T. J., "Testing of Hybrid Rocket Fuel Grains at Elevated Temperatures with Swirl Patterns Fabricated Using Rapid Prototyping Technology," *50th AIAA/ASME/SAE/ASEE Joint Propulsion Conference*, Cleveland, OH, AIAA 2014-3754, 2014.

[28] Karabeyoglu, A., Zilliac, G., Cantwell, B., DeZilwa, S., and Castellucci, P., "Scale-Up Tests of High Regression Rate Paraffin-Based Hybrid Rocket Fuels," *Journal of Propulsion and Power*, Vol. 20, No. 6, November-December 2004.

[29] Cantwell, B., Karabeyoglu, A., and Altman, D., "Recent Advances in Hybrid Propulsion," *International Journal of Energetic Materials and Chemical Propulsion*, Vol. 9, No. 4, 2010.

[30] Jens, E. T., Mechentel, F., S, Cantwell, B. J., Hubbard, G. S., and Chandler, A. A., "Combustion Visualization of Paraffin-Based Hybrid Rocket Fuel at Elevated Pressures," *50th AIAA/ASME/SAE/ASEE Joint Propulsion Conference*, Cleveland, OH, AIAA 2014-3848, 2014.

[31] Jens, E. T., Narsai, P. B., Cantwell, B. J., and Hubbard, G. S., "Schlieren Imaging of the Combustion of Classical and High Regression Rate Hybrid Rocket Fuels," *50th AIAA/ASME/SAE/ASEE Joint Propulsion Conference*, Cleveland, OH, AIAA 2014-3849, 2014.

[32] Shark, S. C., Pourpoint, T. L., Son, S. F., and Heister, S. D., "Performance of Dicyclopentadiene/H_2O_2-Based Hybrid Rocket Motors with Metal Hydride Additives," *Journal of Propulsion and Power*, Vol. 29, No. 5, September-October 2013.

[33] Frederick, R. A., Whitehead, J., J., Knox, L. R., and Moser, M. D., "Regression Rates Study of Mixed Hybrid Propellants," *Journal of Propulsion and Power*, Vol. 23, No. 1, January-February 2007.

[34] Thomas, J. C., Peterson, E. L., DeSain, J. D., Ridlehuber, M. N., and Brady, B. B., "Hybrid Rocket Burning Rate Enhancement by Nano-Scale Additives in HTPB Fuel Grains," *50th AIAA/ASME/SAE/ASEE Joint Propulsion Conference*, Cleveland, OH, AIAA 2014-3955, 2014.

[35] Frederick, R. A. and Whitehead, J. J., "Predicting Hybrid Propellant Regression Rate Using Response Surfaces," *Journal of Propulsion and Power*, Vol. 25, No. 3, May-June 2009.

[36] Whitehead, J. J., "Mixed Oxidizer Hybrid Propulsion System Optimization under Uncertainty using Applied Response Surface Methodology and Monte Carlo Simulation," Ph.D. Dissertation, Department of Mechanical and Aerospace Engineering, University of Alabama in Huntsville, Huntsville, AL, 2008.

[37] Lorente, A. P., Yu, N., Zeng, P., and Zhao, B., "Development and Three-dimensional Numerical Simulation of a Double-tube Hybrid Rocket Motor ," *50th AIAA/ASME/SAE/ASEE Joint Propulsion Conference*, Cleveland, OH, AIAA 2014-3546, 2014.

[38] Lorente, A. P., Yu, N., and Zhao, B., "Testing and Evaluation of a Double-Tube Hybrid Rocket Motor," *51st AIAA/ASME/SAE/ASEE Joint Propulsion Conference*, Orlando, FL, AIAA 2015-4035, 2015.

[39] Nagata, H., Okada, K., San'da, T., Kato, T., Akiba, R., Satori, S., and Kudo, I., "Combustion Characteristics of Fibrous Fuels for Dry Towel Hybrid Motor," *JSTS*, Vol. 13, No. 1, pp. 11-16, 1997.

[40] Nagata, H., Aikawa, N., Akiba, R., Kudo, I., Ito, K., and Tanatsugu, N., "Combustion Characteristics of Propellants for Dry Towel Hybrid Rocket Motor," 48th International Astronautical Congress, Paper IAF-97-S.2.08, 6-10 Oct. 1997.

[41] Nagata, H., Teraki, H., Saito, Y., Kanai, R., Yasukochi, H., Wakita, M., and Totani, T., "Verification Firings of End-burning Type Hybrid Rockets," *51st AIAA/ASME/SAE/ASEE Joint Propulsion Conference*, Orlando, FL, AIAA-2015-4199, 2015.

[42] Li, X., Tian, H., Yu, N., and Cai, G., "Experimental Investigation of Combustion in Axial-Injection End Burning Hybrid Rocket Motor," *Journal of Propulsion and Power*, Vol. 31, No. 3, May-June 2015.

[43] McAlevy, III, R. F. and Lee, S. Y., "A Porous Plug Burner Technique for the Study of Composite Solid Propellant Deflagration on a Fundamental Level and its Application to Hybrid Rocket Propulsion," *Heterogeneous Combustion Conference*, Palm Beach, FL, Preprint No. 63-496, 1963.

[44] McAlevy, III, R. F., Lee, S. Y., and Wilson, Jr., R. P., "The Combustion of Porous Aluminum Plugs with Oxygen Throughput," Stevens Institute of Technology, Department of Mechanical Engineering, Technical Report ME-RT 67007, Hoboken, NJ, July 1967.

[45] Mills, A. F., *Heat Transfer*, 1st ed., Irwin, Homewood, IL, 1992.

[46] Stoliarov, S. I. and Walters, R. N., "Determination of the Heats of Gasification of Polymers using Differential Scanning Calorimetry," *Polymer Degradation and Stability*, Vol. 93, No. 2, pp. 422-427, February 2008.

[47] Turns, S. R., *An Introduction to Combustion: Concepts and Applications*, 3rd ed., McGraw-Hill, New York, 2012.

[48] Ferguson, C. R. and Keck, J. C., "Stand-Off Distances on a Flat Flame Burner," *Combustion and Flame*, Vol. 34, pp. 85-98, 1979.

[49] Wang, W. and Rogg, B., "Premixed Ethylene/Air and Ethane/Air Flames: Reduced Mechanisms Based on Inner Iteration," *Reduced Kinetic Mechanisms for Applications in Combustion Systems*, edited by Peters, N. and Rogg, B., m15, Lecture Notes in Physics, Springer-Verlag, Berlin, Germany, 1993, pp. 76-101.

[50] Law, C. K., "A Compilation of Experimental Data on Laminar Burning Velocities," *Reduced Kinetic Mechanisms for Applications in Combustion Systems*, edited by Peters, N. and Rogg, B., m15, Lecture Notes in Physics, Springer-Verlag, Berlin, Germany, 1993, pp. 15-26.

[51] Beckstead, M. W., Derr, R. L., and Price, C. F., "A Model of Composite Solid-Propellant Combustion Based on Multiple Flames," *AIAA Journal*, Vol. 8, No. 12, December 1970.

[52] Summerfield, M., Sutherland, G. S., Webb, M. J., Taback, H. J., and Hall, K. P., "Burning Mechanism of Ammonium Perchlorate Propellants," *Solid Propellant Rocket Research*, ARS Progress in Aeronautics and Astronautics Vol. 1, Academic Press, 1960, pp. 141-182.

[53] Blair, D. W., Bastress, E. K., Hermance, C. E., Hall, K. P., and Summerfield, M., "Some Research Problems in the Steady-State Burning of Composite Solid Propellants," *Solid Propellant Rocket Research*, ARS Progress in Aeronautics and Astronautics Vol. 1, Academic Press, 1960, pp. 183-206.

[54] Cor, J. J., "A Continuous Oxidizer Regression Model for the Combustion of Composite Solid Propellants," M.S. Thesis, Mechanical Engineering Department, University of Illinois at Urbana-Champaign, Urbana, IL, 1987.

[55] Mulkey, H. W., "Development of a Liquid Oxygen Facility for Rocket Engine Injector Performance Testing," M.S.E. Thesis, Department of Mechanical and Aerospace Engineering, University of Alabama in Huntsville, Huntsville, AL, 2010.

[56] Buckley, J. R., Denny, M. D., and Nelson, G. J., "Computed Tomography Characterization of a Porous Hybrid Motor Grain," *51st AIAA/ASME/SAE/ASEE Joint Propulsion Conference*, Orlando, FL, AIAA-2015-4119, 2015.

[57] "Type T Reference Tables N.I.S.T. Monograph 175 Revised to ITS-90," OMEGA Engineering, Inc., [http://www.omega.com/temperature/Z/pdf/z207.pdf Accessed 2/17/2016]

[58] "Type K Reference Tables N.I.S.T. Monograph 175 Revised to ITS-90," OMEGA Engineering, Inc., [http://www.omega.com/temperature/Z/pdf/z204-206.pdf Accessed 2/17/2016]

[59] Ikard, R. L., "Experimental Injector Element Stability Characterization and Combustion Imaging," M.S.E. Thesis, Mechanical and Aerospace Engineering Department, University of Alabama in Huntsville, Huntsville, AL, 2010.

[60] Frederick, Jr., R. A., Williams, B. M., Bain, J. C., and Nichols, J. A., "Predicting X-Ray Images for Burning Solid-Propellant Rocket Motors," *29th Aerospace Sciences Meeting*, Reno, NV, AIAA 91-0305, 1991.

[61] Mascaro, M. D., "Regression Rate Determination of a Gas Generator Hybrid Rocket Motor with GOX," M.S.E. Thesis, Mechanical and Aerospace Engineering Department, University of Alabama in Huntsville, Huntsville, AL, 2015.

[62] Coleman, H. W., and Steele, W. G., *Experimentation, Validation, and Unceratinty Analysis for Engineers*, 3rd ed., John Wiley & Sons, Inc., Hoboken, New Jersey, 2009, Chap. 3-4.

[63] "Thermophysical Properties of Fluid Systems," NIST, [http://webbook.nist.gov/chemistry/fluid/ Accessed 4/13/2015].

[64] ProPep 3, Propellant Performance Evaluation Program 3, Software Package, Ver. 1.0.1, NASSA, Las Vegas, NV, 2013.

[65] Cequel Toolbox, Chemical Equilibrium in Excel, Software Package, Ver. 1.77, Software and Engineering Associates Inc. and SpreadsheetWorld, Inc., Carson City, NV, 2004.

[66] Gaseq, Chemical Equilibria in Perfect Gases, Software Package, Ver. 0.79, Chris Morley, http://www.gaseq.co.uk/, 2005.

[67] Condon, J. A. and Osborn, J. R., "The Effect of Oxidizer Particle Size Distribution on the Steady and Nonsteady Combustion of Composite Propellants," Purdue University, School of Mechanical Engineering, Final Report AFRPL-TR-78-17, West Lafayette, IN, August 1978.